A HIGH-FIDELITY NON-INTRUSIVE REDUCED-ORDER MODEL FOR THE STATIC AEROELASTIC BEHAVIOR OF LIFTING SURFACES

A THESIS SUBMITTED TO
THE GRADUATE SCHOOL OF NATURAL AND APPLIED SCIENCES
OF
MIDDLE EAST TECHNICAL UNIVERSITY

BY

ZARİF ÖZGE ÖZKAYA

IN PARTIAL FULFILLMENT OF THE REQUIREMENTS
FOR
THE DEGREE OF DOCTOR OF PHILOSOPHY
IN
AEROSPACE ENGINEERING

JUNE 2025

Approval of the thesis:

A HIGH-FIDELITY NON-INTRUSIVE REDUCED-ORDER MODEL FOR THE STATIC AEROELASTIC BEHAVIOR OF LIFTING SURFACES

submitted by **ZARİF ÖZGE ÖZKAYA** in partial fulfillment of the requirements for the degree of **Doctor of Philosophy** i**n Aerospace Engineering, Middle East Technical University** by,

Prof. Dr. Naci Emre Altun
Dean, **Graduate School of Natural and Applied Sciences** _____

Prof. Dr. Serkan Özgen
Head of the Department, **Aerospace Engineering** _____

Prof. Dr. Altan Kayran
Supervisor, **Aerospace Engineering, METU** _____

Examining Committee Members:

Prof. Dr. İsmail Hakkı Tuncer
Aerospace Engineering, METU _____

Prof. Dr. Altan Kayran
Aerospace Engineering, METU _____

Assoc. Prof. Dr. Melin Şahin
Aerospace Engineering, METU _____

Assoc. Prof. Dr. Mustafa Kaya
Aerospace Engineering, AYBÜ _____

Assoc. Prof. Dr. Touraj Farsadi
Aerospace Engineering, ATU _____

Date: 16.06.2025

I hereby declare that all information in this document has been obtained and presented in accordance with academic rules and ethical conduct. I also declare that, as required by these rules and conduct, I have fully cited and referenced all material and results that are not original to this work.

Name Last name: Zarif Özge Özkaya

Signature :

ABSTRACT

A HIGH-FIDELITY NON-INTRUSIVE REDUCED-ORDER MODEL FOR THE STATIC AEROELASTIC BEHAVIOR OF LIFTING SURFACES

Özkaya, Zarif Özge
Doctor of Philosophy, Aerospace Engineering
Supervisor: Prof. Dr. Altan Kayran

June 2025, 160 pages

This study proposes an efficient, low-cost reduced-order method for analyzing the static aeroelastic behavior of a three-dimensional sweptback wing, focusing on the impact of wing elasticity on model efficiency. The primary method used is Proper Orthogonal Decomposition (POD) coupled with Radial Basis Function (RBF) interpolation. The results reveal that reduced-order modeling (ROM) is more effective for the aeroelastic wing, particularly when the pressure coefficient (Cp) is the output. This improvement is attributed to the bending-torsion coupling in the aeroelastic wing, which reduces the effective angle of attack and delays flow separation. For flexible wings, the study further shows that rigid node assumption is insufficient for accurately capturing Cp distributions; hence, separate ROMs must be generated for the deformed positions of the nodes. These node-specific ROMs also enable accurate predictions of the wing deflection. Additionally, the RBF method is applied to generate surrogate models by direct interpolation of the data ensemble. The accuracy, computational cost, and practicality of the POD-RBF coupled ROM and the RBF surrogate model are compared. The study also explores

the use of Artificial Neural Networks (ANN) to predict Cp values, both in combination with POD to develop a reduced-order model and independently as a surrogate model. The findings show that the POD-ANN based ROM outperforms the ANN surrogate model in terms of predictive accuracy and computational efficiency. In conclusion, the methods proposed in this study provide a highly efficient and accurate alternative to high-fidelity analyses, offering substantial computational savings and making them valuable for future aeroelastic modeling.

Keywords: Reduced Order Modelling, Static Aeroelasticity, Proper Orthogonal Decomposition, Radial Basis Functions, Artificial Neural Networks.

ÖZ

KANAT YÜZEYLERİNİN STATİK AEROELASTİK DAVRANIŞI İÇİN YÜKSEK DOĞRULUKLU İNDİRGENMİŞ MODEL

Özkaya, Zarif Özge
Doktora, Havacılık ve Uzay Mühendisliği
Tez Yöneticisi: Prof. Dr. Altan Kayran

Haziran 2025, 160 sayfa

Bu çalışma, üç boyutlu geriye eğik bir kanadın statik aeroelastik davranışını analiz etmek için verimli, düşük maliyetli indirgenmiş bir model önermektedir. Bu çalışma, kanat elastikiyetinin model verimliliği üzerindeki etkisini vurgulamaktadır. Kullanılan ana yöntem, Uyumlu Ortogonal Ayrışım (UOA) ile Radyal Tabanlı Fonksiyonlar (RBF) interpolasyonunun birleşimi ile oluşturulmuş indirgenmiş modeldir. Sonuçlar, basınç katsayısı (Cp) çıktı olarak alındığında, indirgenmiş modellemenin aeroelastik kanat için daha etkili olduğunu göstermektedir. Bu iyileşme, aeroelastik kanattaki eğilme-bükülme birleşiminin bir sonucu olarak, etkili hücum açısını düşürmesi ve akış ayrılmasını geciktirmesiyle açıklanmıştır. Esnek kanatlar için yapılan analizler, rijit düğüm noktalarının Cp dağılımlarını doğru bir şekilde göstermek için yeterli olmadığını göstermektedir; bu nedenle, düğüm noktalarının deforme olmuş konumları için ayrı modeller oluşturulmalıdır. Oluşturulan bu modeller, kanat sapmasını da doğru bir şekilde tahmin etmeyi mümkün kılar. Bu çalışmada ayrıca, RBF yöntemi, veri setinin doğrudan interpolasyonu ile ikame modelleri oluşturmak için uygulanmıştır. UOA-RBF

indirgenmiş modeli ile RBF ikame modelinin doğruluğu, hesaplama maliyeti ve pratikliği karşılaştırılmıştır. Bu çalışmada ek olarak, Cp değerlerini tahmin etmek için Yapay Sinir Ağları (YSA) kullanımı incelenmiştir; hem UOA ile indirgenmiş bir model geliştirme hem de bağımsız bir ikame model olarak uygulanmıştır. Sonuçlar, UOA-YSA tabanlı indirgenmil modelin, YSA tabanlı ikame modeline göre tahmin doğruluğu ve hesaplama verimliliği açısından daha iyi performans gösterdiğini ortaya koymuştur. Sonuç olarak, bu çalışmada önerilen yöntemler, yüksek doğruluk ve verimlilik sağlayarak yüksek-fidelite analizlerine kıyasla önemli hesaplama tasarrufları sunmakta ve gelecekteki aeroelastik modelleme çalışmaları için değerli bir alternatif oluşturmaktadır.

Anahtar Kelimeler: İndirgenmiş Model, Statik Aeroelastisite, Uyumlu Ortogonal Ayrışım, Radyal Tabanlı Fonksiyonlar, Yapay Sinir Ağları.

To My Family

ACKNOWLEDGMENTS

I would like to express my deepest gratitude to my supervisor Prof. Dr. Altan Kayran for his invaluable guidance, advice, criticism and encouragement throughout this study. His insightful feedback, suggestions and expert knowledge has been priceless.

I also extend my thanks to the members of my thesis committee for their thoughtful suggestions and constructive criticism.

I am deeply grateful to my parents for their support and belief in me. Their constant encouragement kept me going through the most challenging times of my academic journey.

Finally, a special thanks to my life partner, Murat Yılmaz, for his unwavering support and patience, which have been a constant source of strength throughout this study.

TABLE OF CONTENTS

ABSTRACT v

ÖZ vii

ACKNOWLEDGMENTS x

LIST OF TABLES xiv

LIST OF FIGURES xv

1 INTRODUCTION 1

1.1 Overview 1

1.2 Motivation and Objectives 10

1.3 Limitations 12

1.4 Content of the Study 13

2 HIGH-FIDELITY FULL ORDER MODEL 15

2.1 AGARD 445.6 Wing 17

2.2 Elongated AGARD 445.6 Wing 23

3 REDUCED ORDER MODELING WITH PROPER ORTHOGONAL DECOMPOSITION 27

3.1 Proper Orthogonal Decomposition (POD) Method 27

3.2 Reconstruction of the Results Based on the POD Method 30

3.2.1 Three-Dimensional Rigid Wing Configuration 32

3.2.2 Three-Dimensional Aeroelastic Wing Configuration 37

3.2.3 Dataset Involving Higher Mach Numbers 47

4 REDUCED ORDER MODELING WITH POD-RBF METHOD AND SURROGATE MODELING WITH RADIAL BASIS FUNCTIONS 57

4.1 Radial Basis Function (RBF) Method 57
4.2 Reduced Order Modeling with the POD coupled with the RBF 58
4.2.1 Prediction of the Results for the Three-dimensional Rigid Wing Configuration 59
4.2.2 Prediction of the Results for the Three-dimensional Aeroelastic Wing Configuration 62
4.2.3 Prediction of the Results for a Dataset Involving Higher Mach Numbers 68
4.3 Surrogate Modeling with RBF 74
4.3.1 Sampling with Latin Hypercube Sampling Method 78
5 REDUCED ORDER MODELING WITH POD-ANN METHOD AND SURROGATE MODELING WITH ARTIFICIAL NEURAL NETWORKS 83
5.1 Artificial Neural Network (ANN) Method 83
5.2 Reduced Order Modeling with POD coupled with ANN 89
5.2.1 Prediction of the Results for Three-dimensional Rigid Wing Configuration 90
5.2.2 Prediction of the Results for Three-dimensional Aeroelastic Wing Configuration 93
5.2.3 Prediction of the Results for a Dataset Involving Higher Mach Numbers 96
5.3 Surrogate Modeling with ANN 108
6 CONCLUSIONS AND FUTURE WORKS 117
6.1 Conclusions 117
6.2 Future Works 121
REFERENCES 123

APPENDICES 131

A. Mesh Sensitivity for Structural Analysis 131

B. NRMSE Distribution for Different Mode Numbers 133

C. Mesh Refinement Study for Higher Mach Conditions 136

D. Flow Conditions where Shock Formation is Observed 139

E. Accumulated Energy and NRMSE Distribution of the Reconstructed Cp for Each Data Pair with Different Data Sizes 141

F. NRMSE Distribution of the Surrogate Model using Cubic Spline Interpolation Method 143

G. Prediction Performance of the RBF and Linear Interpolation Methods for the Reduced Parameter Sizes Obtained from LHS 144

H. NRMSE Distribution of ANN Models with Different Number of Layers and Neurons 146

I. ANN Configurations with Different Number of Layers and Neurons..... 149

J. Prediction Performance of POD based ROMs and Bilinear Interpolation for Different Data Sizes 154

K. Prediction of the Results for Data Points Outside the Snapshot Matrix of 63 Parameter Pairs 155

CURRICULUM VITAE 159

LIST OF TABLES

TABLES

Table 2.1 Comparison of the results of different mesh sizes 23
Table 2.2 Comparison of the modal frequencies 24
Table 3.1. Computational time of SVD and MOS methods* 32
Table 3.2. Comparison of the maximum displacements of the aeroelastic wing at M=0.85 & AOA=5º 42
Table 3.3. Comparison of the POD mode numbers for different cases 51
Table 4.1. Maximum deflection and von Mises stress results for the POD-RBF ROM and RBF based surrogate models (M=0.83 and AOA=4.75°) 77
Table 4.2. Comparison of the computational time for the Cp distribution for the rigid and the aeroelastic wing (M=0.83 and AOA=4.75°)* 77
Table 5.1. Training Algorithms [59] 86
Table 5.2. Comparison of the errors for both wing configurations using POD-ANN ROM method 96
Table 5.3. Comparison of the CPU time of training and epoch number for different methods* 112
Table 5.4. Comparison of the CPU time of prediction for different methods (rigid wing for M=0.83 & AOA=4.75º)* 112
Table 5.5. Comparison of the CPU time of prediction for different methods (rigid wing for M=0.83 & AOA=4.75º)* 114

LIST OF FIGURES

FIGURES

Figure 2.1. One-way solution process (a) for rigid wing and two-way solution process (b) for elastic wing 15
Figure 2.2. Example input and output for Linear Shape Function mapping..... 16
Figure 2.3. Example input and output for conservative Intersect-Scatter-Gather mapping..... 17
Figure 2.4. AGARD 445.6 wing panel dimensions 18
Figure 2.5. Comparison of natural frequencies and mode shapes with literature [55] 18
Figure 2.6. Structural mesh configuration of the AGARD 445.6 wing 19
Figure 2.7. CFD mesh configuration of the fluid domain (a) and detailed view of the CFD mesh configuration of the wing profile (b) 19
Figure 2.8. Root section of the wing mesh (a) and the detailed view of the boundary layer (b) 20
Figure 2.9. Comparison of Cp distribution with literature at 0.67 and 0.34 span locations [56] 20
Figure 2.10. Comparison of aeroelastic Cp distribution with literature at 0.67 and 0.34 span locations [56] 21
Figure 2.11. Comparison of Cp distribution of rigid and elastic wings at 0.67 and 0.34 span locations [56] 21
Figure 2.12. Deflection of the leading and trailing edges [56] 22
Figure 2.13. Comparison of Cp distribution for different mesh sizes at 0.67 and 0.34 span locations [56] 23
Figure 2.14. Dimensions of the baseline AGARD 445.6 wing (a) and the AGARD 445.6 wing with elongated span (b) 24
Figure 2.15. Structural mesh configuration of the elongated AGARD 445.6 wing 24
Figure 2.16. CFD mesh configuration of the fluid domain (a) and detailed view of the CFD mesh configuration of the wing profile (b) 25

Figure 3.1. Lattice of snapshots 30
Figure 3.2. Spanwise (a) and chordwise (b) sections taken from the wing 31
Figure 3.3. Spanwise (a) and chordwise nodes (b) 31
Figure 3.4. Fraction of energy and accumulated energy (% energy) for the Cp of the rigid wing 33
Figure 3.5. NRMSE and R^2 errors for 1 mode and 8 modes for the rigid wing 33
Figure 3.6. Cp distribution on the top (a) and bottom (b) wing surfaces for the high-fidelity analysis and reconstructed Cp for 1 mode and 8 modes (M=0.85 and AOA=5º) 34
Figure 3.7. Variation of Cp along the chordwise (a) and spanwise (b) wing sections for the high-fidelity analysis result and the reconstructed Cp for 1 mode and 8 modes (M=0.85 and AOA=5º) 35
Figure 3.8. Variation of Cp along the chordwise ((a) & (c)) and spanwise ((b) & (d)) wing sections for the high-fidelity analysis result and the reconstructed Cp for the least accurate flow conditions 36
Figure 3.9. Fraction of energy and accumulated energy (% energy) for the Cp of the aeroelastic wing 37
Figure 3.10. Fraction of energy for the x, y, z position of the nodes 38
Figure 3.11. NRMSE and R^2 errors for 1 mode and 5 modes for the aeroelastic wing 38
Figure 3.12. Cp distribution on the top (a) and bottom (b) wing surface for the high-fidelity analysis and reconstructed Cp for 1 mode and 5 modes (M=0.85 and AOA=5º) 39
Figure 3.13. Cp distribution on the top (a) and bottom (b) wing surface for the high-fidelity analysis and reconstructed Cp for 1 mode and 5 modes (M=0.55 and AOA=1º) 39
Figure 3.14. Variation of Cp along the chordwise ((a) & (c)) and spanwise ((b) & (d)) wing sections for the high-fidelity analysis result and the reconstructed Cp for 1 mode and 5 modes 40

Figure 3.15. Isometric view (a) and side view (b) of the reconstructed displacement of the aeroelastic wing using POD based ROM (M=0.85 and AOA=5º) 41
Figure 3.16. Cp vs normalized chord (x_n) of the rigid and the aeroelastic wing (M=0.85 for AOA = 1º, 3º, 5º) 43
Figure 3.17. Span locations where sectional Cp distributions are compared 44
Figure 3.18. Streamlines around the rigid (a) and the aeroelastic wing (b) at different span locations (M=0.85 and AOA=5º) 44
Figure 3.19. Twist of the aeroelastic wing at different sections (a) and decrease in the effective AOA at these sections (b) 45
Figure 3.20. Fraction of energy for the von-Mises stress in the aeroelastic wing . 46
Figure 3.21. NRMSE and R^2 error for the von-Mises stress on the aeroelastic wing 46
Figure 3.22. von-Mises stress distribution on the top (a) and bottom (b) wing surfaces obtained by the high-fidelity aeroelastic analysis and the reconstructed result with 1 mode (M=0.55 & AOA=1º) 47
Figure 3.23. Extended dataset with 81 data points 48
Figure 3.24. The Cp distribution on the wing; as well as the Mach variation at 0.8 m (a) and 0.5 m (b) span locations, chordwise Cp distributions at 0.8 m (c) and 0.5 m (d) span locations on the rigid wing for M=0.95 and AOA=5° flow condition..... 49
Figure 3.25. The Cp distribution on the wing, as well as the variation of M at the 0.5 span location (a) and the chordwise Cp distribution at the 0.5 span location of the aeroelastic wing (b) 50
Figure 3.26. Accumulated energy for the Cp of the rigid wing (a) and the aeroelastic wing (b) 50
Figure 3.27 NRMSE and R^2 errors for the reconstructed Cp results using 14 modes for the rigid wing 51
Figure 3.28 Chordwise (at 0.8 m of the span) (a) and spanwise (b) Cp distributions of the rigid wing for the 71st, 1st and 81st flow conditions reconstructed with 14 modes 52

Figure 3.29 NRMSE and R^2 errors for reconstructed Cp results using 8 modes for the aeroelastic wing 52
Figure 3.30 Spanwise (a) and chordwise (at 0.8 (b) and at 0.5 (c)) Cp distributions for the 81st and spanwise (d) and chordwise (at 0.8 (e) and at 0.5 (f)) Cp distributions for the 71st flow condition for the aeroelastic wing 53
Figure 3.31 Chordwise Cp distributions at 0.8 m span of the aeroelastic wing with the reconstructed nodes using 1 mode (a) and the rigid nodes (b) (M=0.95 and AOA=5°) 54
Figure 3.32 Isometric view (a) and side view (b) of the reconstructed displacement of the aeroelastic wing using POD based ROM (M=0.95 and AOA=5°) 54
Figure 4.1. Samples from the LHS 59
Figure 4.2. NRMSE of the Cp results for the rigid wing 60
Figure 4.3 Cp distribution on the top (a) and the bottom (b) surfaces of the rigid wing obtained by high-fidelity CFD analysis and the predicted Cp via POD-RBF interpolation (M=0.83 and AOA=4.75°) 61
Figure 4.4 Variation of the Cp for different chordwise sections of the rigid wing obtained by high-fidelity CFD analysis and the predicted Cp via the POD-RBF interpolation (M=0.83 and AOA=4.75°) 61
Figure 4.5 Variation of the Cp at the spanwise section of the rigid wing obtained by high-fidelity CFD analysis and the predicted Cp via the POD-RBF interpolation (M=0.83 and AOA=4.75°) 62
Figure 4.6. NRMSE of the Cp results for aeroelastic and rigid wings 63
Figure 4.7. Cp distribution on the top (a) and the bottom (b) surfaces of the wing obtained by high-fidelity static aeroelastic analysis and the predicted Cp via the POD-RBF interpolation (M=0.83 and AOA=4.75°) 64
Figure 4.8. Chordwise (at the 0.95 m span location) Cp variation of high-fidelity static aeroelastic analysis and the predicted Cp of the POD-RBF interpolation (M=0.83 and AOA=4.75°) 65
Figure 4.9. Spanwise Cp variation of high-fidelity static aeroelastic analysis and the predicted Cp of the POD-RBF interpolation (M=0.83 and AOA=4.75°) 66

Figure 4.10. von Mises Stress distribution on the top (a) and bottom (b) wing surfaces (M=0.83 and AOA=4.75°) 67
Figure 4.11 Intermediate points to be predicted (a) and the new prediction points (b) 68
Figure 4.12 NRMSE of the Cp results for the rigid wing using 63-sample and 81-sample cases 68
Figure 4.13 Chordwise (at 0.65 m span) (a) and spanwise (b) Cp distributions of the rigid wing predicted using POD-RBF with 81 data samples (M=0.93 and AOA=4.8°) 69
Figure 4.14 Cp distribution on the upper surface of the rigid wing for the 14th flow condition (M=0.93 and AOA=4.8°) 69
Figure 4.15 NRMSE of the Cp results for the rigid and aeroelastic wings obtained using POD-RBF approach 70
Figure 4.16 Chordwise (at 0.8m (a) and 0.35m (b) span) and spanwise (c) Cp distributions of the aeroelastic wing for the 14th prediction point 70
Figure 4.17 Cp distribution on the upper surface of the aeroelastic wing for the 14th flow condition (M=0.93 and AOA=4.8°) 71
Figure 4.18. Updated dataset with 90 data points 72
Figure 4.19. NRMSE of the Cp results for the rigid and aeroelastic wings obtained using POD-RBF 72
Figure 4.20. Chordwise (at 0.8m (a) and 0.5m (b) span) and spanwise (c) Cp distributions of the rigid wing for the 15th prediction point 73
Figure 4.21. Cp distribution on the upper surface of the rigid wing for the 15th flow condition (M=0.944 and AOA=4.74°) 73
Figure 4.22. Chordwise (at 0.8m (a) and 0.5m (b) span) and spanwise (c) Cp distributions of the aeroelastic wing for the 15th prediction point 74
Figure 4.23. Cp distribution on the upper surface of the aeroelastic wing for the 15th flow condition (M=0.944 and AOA=4.74°) 74
Figure 4.24. NRMSE of the Cp results for rigid and the aeroelastic wings via the coupled POD-RBF ROM and the RBF-based surrogate model predictions 75

Figure 4.25. Variation of Cp along the chordwise ((a) and (c)) and spanwise ((b) and (d)) wing sections predicted via the RBF-based surrogate model 76
Figure 4.26. Parameter pairs used for the snapshot matrix and prediction 79
Figure 4.27. Randomly selected parameters pairs of M=0.8050 and AOA=4.2668° and M=0.6371 and AOA= 2.7588° from 30 LHS parameters and 15 LHS parameters case, respectively 79
Figure 4.28. Chordwise ((a) and (c)) and spanwise ((b) and (d)) Cp distributions for aeroelastic wings at two different flow conditions 80
Figure 4.29. NRMSE for the Cp results using the RBF method with different number of input pairs 80
Figure 4.30. Variation of the Cp along the chordwise (a) and spanwise (b) wing sections obtained by the high-fidelity analysis and the predicted Cp via the RBF model with 30 LHS parameters (M=0.83 & AOA=4.75º) 81
Figure 5.1. Schematic diagram of the artificial neural network 84
Figure 5.2. Tan-Sigmoid and Linear Transfer Functions 85
Figure 5.3. NRMSE for the Cp results of the rigid wing using the POD-ANN model with different neuron numbers 90
Figure 5.4. Output vs. target plots of basis coefficients for the ANN with 15 neurons 91
Figure 5.5. MSE vs epoch number for the ANN with 15 neurons 92
Figure 5.6. Cp distribution on the top (a) and bottom (b) surfaces of the rigid wing obtained by the high-fidelity analysis and predicted results via the POD-ANN reduced order model (M=0.83 and AOA=4.75º) 93
Figure 5.7. NRMSE for the Cp results of the aeroelastic wing using the POD-ANN model with different neuron numbers 94
Figure 5.8. Output vs. target plots of basis coefficients for the ANN with 15 neurons for the aeroelastic wing 94
Figure 5.9. MSE vs epoch number for the ANN with 15 neurons for the aeroelastic wing 95

Figure 5.10. Cp distribution on the top (a) and bottom (b) surfaces of the aeroelastic wing obtained by the high-fidelity analysis and predicted results via the POD-ANN reduced order model (M=0.83 and AOA=4.75º) 95
Figure 5.11 NRMSE of the Cp results obtained by using POD-RBF and POD-ANN (1 layer-35 neurons for rigid and 1 layer-9 neurons for aeroelastic wing) approaches (81 dataset) 96
Figure 5.12 NRMSE distribution for Cp predictions of the rigid wing using POD-ANN method with different ANN configurations (a) and output vs target plot for ANN with 1 layer and 35 neurons (b) 97
Figure 5.13 Difference in results for the aeroelastic wing at the 14th prediction point 98
Figure 5.14 NRMSE distribution for aeroelastic Cp prediction using POD-ANN method with different ANN configurations (a) and output vs target plot for ANN with 1 layer and 9 neurons (b) 98
Figure 5.15 NRMSE of the Cp results for the rigid and aeroelastic wings obtained by using different datasets with POD-ANN method 99
Figure 5.16 Chordwise (at 0.8m (a) and 0.5m (b) span) and spanwise (c) Cp distributions of the rigid wing obtained from POD-ANN for 15th prediction point 99
Figure 5.17 Cp distribution on the upper surface of the rigid wing for the 15th flow condition (M=0.944 and AOA=4.74°) 100
Figure 5.18 NRMSE of the Cp results for the rigid and aeroelastic wings obtained from different approaches using 90 data samples 100
Figure 5.19. Spanwise ((a) & (c)) Cp distribution and NRMSE distribution ((b) & (d)) of the rigid wing obtained from POD-ANN and POD-RBF for the 13th point 101
Figure 5.20. Spanwise ((a) & (c)) Cp distribution and NRMSE distribution ((b) & (d)) of the aeroelastic wing obtained from POD-ANN and POD-RBF for the 13th point 101
Figure 5.21. Predicted displacement using both approaches for the 13th prediction point (M=0.87 and AOA=3.6°) 102

Figure 5.22. Chordwise at 0.5 m span ((a) & (d)) and spanwise Cp distributions ((b) & (e)) along with the NRMSE distribution on the upper surface of the aeroelastic wing ((c) & (f)) obtained from POD-ANN and POD-RBF predictions at 15th point 103
Figure 5.23. Cp vs normalized chord (x_n) of the rigid wing and the aeroelastic wing (AOA = 5º for M = 0.85, 0.9, 0.93 and 0.95) 104
Figure 5.24. Extended dataset with 126 samples 105
Figure 5.25 NRMSE of the Cp results for the rigid wing obtained from both approaches using 126-sample dataset 106
Figure 5.26 Spanwise Cp distributions for the 14th and 15th prediction point obtained using POD-ANN and POD-RBF approaches (126-sample dataset) 107
Figure 5.27. NRMSE distribution for Cp prediction of the rigid wing using POD-ANN and POD-RBF methods for different number of datasets 107
Figure 5.28. NRMSE for the Cp results using the ANN based surrogate model with different neuron numbers for the rigid wing 109
Figure 5.29. Output vs. target plots of Cp results for the ANN with 80 neurons for the rigid wing 110
Figure 5.30. NRMSE for the Cp results using the ANN based surrogate model with different neuron numbers for the aeroelastic wing 110
Figure 5.31. Output vs. target plots of Cp results for the ANN with 70 neurons for the aeroelastic wing 111
Figure 5.32. MSE vs epoch number for the ANN with 80 neurons for rigid wing (a) and 70 neurons for aeroelastic wing (b) 111
Figure 5.33. Comparison of NRMSE for the Cp results using 2 different methods for the rigid and aeroelastic wings 113
Figure 5.34. Comparison of NRMSE for the Cp results using POD based ROMs (63-sample dataset) 114

CHAPTER 1

INTRODUCTION

1.1 Overview

Recent advancements in material technology and innovative production methods coupled with the efforts in the field of structural optimization have considerably contributed to the widespread adoption of lightweight structures within the aviation industry. Furthermore, the growing demand for highly efficient designs characterized by reduced induced drag and sustained, endurant flight performance has called for an increase in aspect ratio. As a direct consequence of this weight reduction alongside the elevated aspect ratio, the static aeroelastic behavior of aerospace structures emerges as an important phenomenon that needs a comprehensive investigation and consideration during the design process since it greatly affects the flight performance. Understanding these interactions is essential for optimizing performance and ensuring the structural integrity of the aerospace structures. However, high fidelity numerical simulations of such aeroelastic problems are computationally intensive studies that require significant computational resource and time. The data acquired from such complex studies need effective post processing strategies to gain insight of the physics of the problem and assessment of the models with different variables. Therefore, there is an increasing interest in exploiting reduced order models (ROMs) as well as surrogate models among the scientific community which reflects the behavior of a complex system with a reasonable accuracy while alleviating the computational burden.

There are many approaches for the requirement of order reduction; however, Proper Orthogonal Decomposition (POD) stands out as the most widely utilized method of which efficiency is proven by many studies in various scientific fields like aerodynamics, structural mechanics, aeroelasticity etc. for years. In this method, the

dominant features of the solutions of similar problems are extracted and the reduced model is constructed by exploiting these dominant features. The POD method produces an optimal linear set of basis vectors that describe the ensemble of data in an optimum way [1]. Then the reduced order system is represented by linear superposition of the basis vectors and corresponding basis coefficients allowing for a more efficient analysis without significant loss of fidelity. To determine the basis coefficients, several methods are available which make the ROM modeling as intrusive or nonintrusive. As one way, the governing equations of the high-fidelity system can be projected onto the reduced space spanned by basis vectors. The Galerkin method is used frequently as a projection technique in both aerodynamic and aeroelastic studies [2-6]. Since the original equations of the system is modified in this method, such methods are called as intrusive. Preserving the underlying physics and need of access to the governing equations are the main points of these methods. On the other hand, basis coefficients can also be obtained by projecting the available solutions on the basis vectors. Exploiting these basis coefficients at hand, others can be obtained with different methods that make the prediction of solutions possible with different parameters of interest. Since such methods do not depend on governing equations, they are called as nonintrusive methods.

The efficiency of intrusive or nonintrusive ROMs in terms of accuracy and computational cost is problem dependent and investigated by several authors. A comparative study between POD interpolation and POD projection methods is conducted by Wang et al. [7] for heat transfer problems. It is demonstrated that for the four-variable problem, POD with linear interpolation gives higher accuracy than projection; however, for the problem with six variables the opposite is the case. Zimmermann and Görtz proposed an intrusive POD based ROM approach for solving steady aerodynamic flows [8]. Authors state that even if the intrusive POD method is more computationally costly, it gives more accurate extrapolation results compared with the POD based interpolation approaches using Kriging and thin-plate spline methods. Similarly, in the study of Sinha et al. [9], a comparison between the intrusive POD approach and the nonintrusive POD coupled with thin-plate spline

radial basis functions shows that the accuracy of the POD based interpolation methods is inadequate, especially in extrapolative cases. They employ intrusive POD based ROM approach for the prediction of aerodynamic coefficients of subsonic missile by adopting Mach number, angle of attack and roll angle as parameters. Hesthaven and Ubbiali [10] employed neural networks (NN) to approximate the basis coefficients and constructed nonintrusive POD-NN ROM for steady state partial differential equations with physical and geometric parameters. Authors show that same predictive accuracy is obtained compared with the POD-Galerkin method with a lower computational cost. Similarly in the study of San et al. [11], artificial neural network (ANN) is used in conjunction with the POD for the transient fluid model at various Reynolds numbers and it is demonstrated that the POD-ANN approach is superior to the intrusive POD-Galerkin projection approach for the case investigated. Several studies aim to leverage both approximations to enhance the efficiency of their solutions. For example, in the study of Ding et al. [12], POD based ROM is presented for the prediction of fluid flow and heat transfer problems. For steady problems, the basis coefficients are obtained using the cubic spline interpolation (CSI) method, with the Reynolds number as the variable. For transient problems, Galerkin projection is employed, taking time as the variable. The use of the POD based algorithm is seen to predict the fluid and temperature fields accurately alongside the drastic time reduction. In addition, Cao et al. [13] presented an efficient multistep ROM method for steady airfoil flows especially when there are shock waves. Authors combined both approaches by using a non-intrusive POD-Radial Basis Function (RBF) ROM to provide a good initial guess and reduce the computational cost while employing the intrusive ROM to enhance accuracy.

In the literature, although there are cases where intrusive methods are reported to give more accurate results; it is known that many industrial applications rely on commercial solvers such that interference of the source code may not be possible or can be a highly complex task. Nevertheless, in industrial applications due to the endeavors of design optimization, uncertainty quantification etc., ROMs and surrogate models can be especially useful. Therefore, the demand for simple, low

cost yet accurate models can be provided by nonintrusive ROMs. Since there is no need to access the governing equations of the problem at hand, nonintrusive ROMs enable great flexibility for practical applications in industrial as well as scientific fields.

For the construction of POD based nonintrusive ROMs, several interpolation methods can be adopted for the calculation of basis coefficients such as spline interpolations, RBF methods, Kriging interpolations etc. The interpolated coefficients are subsequently exploited for the prediction of the data at the relevant parameters including flow variables (angle of attack, Mach number etc.), geometric variables (span, thickness etc.), structural variables (stiffness, density etc.) or flight conditions (altitude, load factor etc.). For the unsteady analyses, time and frequency can also be a varying parameter. In some cases, different kinds of variables, such as flow and structural variables, are investigated simultaneously. Among the early studies, Bui-Thanh et al. [14] coupled POD with CSI to develop a ROM that captures variations in angle of attack and Mach number, investigating the steady transonic flow past over an airfoil. Similarly, in the study of Tang and Shyy [15], POD method is exploited for low order modeling of the steady state, super and hypersonic aerothermodynamics of the selected space-vehicle configuration at varying angle of attack and Mach numbers**.** The basis coefficients are obtained by the response surface method combined with NN. In the study of Taeibi-Rahni et al. [16], POD is coupled with the CSI method and applied for an airfoil at the steady viscous and inviscous flows at different flow regimes**.** The parameters are selected as angle of attack or Mach numbers. Samewisely, Malouin et al. [17] exploited CSI for the coefficients in two-dimensional parameter space of angle of attack and Mach number. Mifsud et al. [18] created a POD based ROM for the parametric studies of weapon aerodynamics**.** Authors employed both flow conditions (Mach number or angle of attack) and geometry (base radius or nose deflection) as parameters in their study. For the construction of the response surface for basis coefficients, different techniques such as linear regression-based method, linear spline, cubic spline and RBF methods are studied. It is stated that RBFs turn out to be more accurate in

predictions. POD based ROM with polynomial response surface and moving least squares methods is also used for a coupled fluid-structure system in the study of Coelho et al. [19]. Multidisciplinary optimization analysis is carried out by considering geometric design variables such as camber and chord. Similarly, in the study of Xiao et al. [20] POD based ROM with RBF interpolation is used for fluid-structure interaction problems utilizing both one-way and two-way solutions by taking snapshots in time. Li et al. [21] proposed a nonintrusive POD-CSI method for the parameterized electromagnetic scattering problems. A two-step POD method is employed to extract time and parameter independent basis functions and the CSI approach is invoked to approximate the time and parameter modes of the coefficients. Fossati and W. G. Habashi [22] applied Bayesian Kriging interpolation, stating that it is more effective for approximating multi-dimensional highly nonlinear problems than the ordinary Kriging method. The proposed POD based ROM is constructed for icing analysis of an airfoil with five parameters, and three-dimensional problem with three parameters. A ROM with the combination of POD and Kriging by taking profile geometry parameters of physical domain as a variable is constructed by Yasong and Junqiang [23]. The method predicts the subsonic stationary flow fields precisely. POD with Kriging method is also investigated in terms of its efficiency for uncertainty quantification analyses [24,25]. Walton et al. [26] presented a ROM by combining POD with the RBF method. The proposed method is applied to unsteady, compressible, inviscid flow over an oscillating three-dimensional wing. The solutions obtained at different frequencies are used as snapshots. Authors demonstrated that POD interpolation techniques are also applicable for unsteady problems. Wang et al. [27] verified the effectiveness of POD based interpolation in terms of computational cost for heat and flow problems and stated that cubic B-spline interpolation is more accurate than linear interpolation. In addition, POD based ROM method is offered by applying polynomial chaos expansion to basis coefficients for uncertainty quantification analyses [28]. Hua and Sorheim [29] created a POD based ROM for parameterized unsteady flow problems. POD coefficients are approximated using the RBF method at every time step for the

parameters of interest. Then, dynamic mode decomposition technique is used to decompose the coefficients into dynamic modes to predict the coefficients for the unsteady system. Xiao et al. [30] employed POD-RBF method for Navier-Stokes equations. The model is verified by two cases of a lock exchange problem and flow past a cylinder problem, taking time as a parameter.

It is evident from the literature that RBF is a widely preferred choice as an interpolation method across a variety of applications. The RBF method stands out due to its flexibility, convenience, and accuracy when applied to scattered multi-dimensional datasets [31]. As it is mentioned in the previous paragraph, effective solutions are achieved through the application of the RBF when it is employed in conjunction with the POD method, enhancing both computational efficiency and accuracy in modeling complex systems. It should also be noted that by applying on a data set directly, the RBF method can effectively serve as a surrogate model across various engineering fields such as aerodynamics and structural analysis as demonstrated in a number of studies in literature [32-37]. Numerous applications of the RBF method demonstrated its capability to yield remarkably efficient results characterized by high accuracy and low computational expense. On the other hand, it is also worth mentioning that in recent years, ANN has been gaining prominence as a powerful method to construct surrogate models as it is demonstrated in various studies [38-40] or reduced order models when combined with POD. ANNs possess a remarkable capability to approximate any function, even in cases involving complicated nonlinear input-output relationships. Providing a substantial amount of data for the underlying relationship, ANNs can establish a nonlinear mapping between a defined set of inputs and their corresponding targets. This process of adjustment is facilitated through a series of linear combinations of parameters and transfer functions that effectively capture the complex behavior of the system, which may not be expressed explicitly in a functional form. As a result, ANN-based surrogate models have become the focus of extensive investigation by many researchers aiming to enhance the performance and applicability of the ANN based models across various engineering problems. In the study of Hesthaven and Ubbiali

[10], NN is used to construct a POD-NN ROM for steady state partial differential equations considering physical and geometric parameters. Then, this study is extended to time-dependent nonlinear problems [41]. Similarly, Sun et al. [42] presented POD based ROM adopting ANN to interpolate the POD coefficients for prediction of transonic flow field with varying geometric parameters. Yu and Hesthaven [44], proposed a POD and ANN method for flow reconstruction and the method achieved reasonable predictions for several two- and three-dimensional cases investigated. A non-intrusive ROM based on POD and ANN is also studied by the Şugar-Gabor [43] for several test cases and it is stated that the ROM shows great potential for the accurate and low-cost modeling of complex parametric unsteady problems. San et al. [11] performed a POD-ANN ROM method on the prediction of a nonlinear wave-propagation problem and showed that the model yields stable and accurate results within inside and outside of the database range. In the work of Renganathan et al. [45] POD is coupled with deep neural network and applied to the inviscid transonic flow past airfoil under varying flow and geometric parameters. Their approach performs on par with the nonintrusive projection-based POD-ROM method in terms of predictive accuracy. Overall, these studies highlight the potential of integrating ANN with POD methods, demonstrating the ongoing evolution of ANN-related research in addressing complex engineering problems.

Among the various applications of the POD based approaches, one significant area of interest is the investigation of static aeroelastic behavior of aerospace structures. In literature, studies exist that examine the static aeroelastic behavior of aircraft structures utilizing ROMs. The ROM techniques can be applied to either the fluid part or the structural part as well as to both parts in order to decrease the size of the model transferred between each discipline. The reduced-order model is expected to accurately approximate results across varying input variables while decreasing computational time significantly. For example, Lindhorst et al. [46] replaced the CFD solver in the aeroelastic coupling scheme with a ROM performing static as well as transient analyses of an airfoil. For the time independent problems, ROM consists of POD with radial basis function artificial neural network (RBF-ANN) method. The

same study is also conducted for wing analysis [47]. In the study of Ripepi et al. [48], ROM is used to predict static aeroelastic loads, to exploit in multidisciplinary optimization analyses. POD and Isomap methods are used for ROM in both intrusive and nonintrusive frameworks. It is seen that intrusive approach helps to reduce errors. Similarly, ROM based on Volterra series method is used for aerodynamic part for static aeroelastic analysis [49**].** On the other hand, in the study of Changchuan et al. [50] structural side of the aeroelastic analysis of a wing is represented by a ROM. A ROM is obtained by regression analysis from load cases and corresponding deformations, then it is coupled with vortex lattice aerodynamics method to obtain the static aeroelastic behavior of the wing. In the study of Berthelin et al. [51] surrogate models are constructed for the aerodynamic and the structural disciplines separately using POD with Gaussian process interpolation.

This study presents a nonintrusive POD based ROM for the static aeroelastic behavior of a 3D wing under varying flow conditions, defined by angle of attack and Mach number. The POD based reduced order modeling is performed for both rigid and flexible wings (referred to as rigid and aeroelastic wings in this study) to compare the effectiveness of the application of the POD based ROM for both configurations. Such a study requires CFD-based aerodynamic analysis in conjunction with static aeroelastic analysis of the 3D wing. Nonintrusive POD-based ROMs are constructed by exploiting high-fidelity CFD simulations of the Navier–Stokes equations for the rigid wing, as well as two-way fluid-structure interaction analyses for the aeroelastic wing. The latter involves coupling high-fidelity CFD for the aerodynamic domain with three-dimensional finite element analysis for the structural domain. Both aerodynamic and structural disciplines are included together under the nonintrusive POD based ROM framework to reconstruct the resultant aerodynamic and structural metrics of the wing. For the evaluation of the prediction capability of the method, pressure coefficient (Cp) distributions are predicted for different angle of attack and Mach conditions for both rigid and aeroelastic wings. Contrary to the rigid wing, the effect of changes in the positions of the nodes of the aeroelastic wing due to the deflection of the wing is also investigated. In this respect,

for the prediction of the Cp distribution by the POD based ROM, converged nodal positions of the wing surface obtained by high-fidelity static aeroelastic analysis are also taken into account while constructing the ROM. For the evaluation of deformed nodal positions, an additional POD-based ROM is generated. Using this ROM, predictions of the Cp distribution and wing deflection are performed for the aeroelastic wing with deformed nodal positions. It is observed that, particularly for highly flexible wings, generating a separate ROM for the deformed nodal positions is essential to accurately capture variations in the Cp distribution along the wing. This separate ROM also facilitates the calculation of wing deformation as a by-product. In addition, von-Mises stress distribution in the aeroelastic wing is obtained by constructing a ROM utilizing the high-fidelity solutions of static aeroelastic analysis.

Moreover, in the present study, at first RBF is adopted as an interpolation method coupled with POD for the CFD analysis of the rigid wing and static aeroelastic analysis of the aeroelastic wing. In addition, the RBF method is also exploited for the prediction of the results with direct interpolation of the data ensemble in a comparative manner. A few studies that compare POD based interpolation and direct interpolation of data ensemble exist in literature. Walton et al. [26] studied unsteady solutions of parameterized fluid flow problems using combined POD and RBF methods and concluded that POD based interpolation method is advantageous over the direct interpolation in terms of computational time. In the study of Zimmerman and Görtz [8], POD-ROM approach is used for predicting steady, turbulent aerodynamic flows. Similarly, this study asserts that even if both entry-by-entry interpolation of the snapshot vectors and interpolation of the basis coefficients give the same results, interpolation of basis coefficient is much more efficient computationally. In the current study, the prediction capability of both methods is evaluated in view of the static aeroelastic analysis of the 3D wing. It is seen that both methods give very similar results with great accuracy. In addition, there is a significant decrease in computational time compared to high-fidelity analyses as expected; however, contrary to other studies, computational time is similar for both

methods. We note that even if the entries to be interpolated are far more than POD coefficients for direct interpolation with the RBF, it is more practical to be applied since computational process is much simpler.

Similarly, as a second case ANN is coupled with POD to construct a reduced order model for the rigid and aeroelastic wings. The ANN method is also investigated as an independent surrogate model to compare with the proposed coupled POD-ANN approach. The models constructed are utilized for the prediction of pressure coefficient (Cp) distributions for different angle of attack and Mach conditions that do not exist in the training data set. Based on the comparison of Cp distribution results obtained with different surrogate and reduced order models, it is shown that the coupled ANN and POD approach is computationally more efficient and has slightly better prediction capability.

One of the main purposes of the present study is to make an efficiency comparison of the surrogate/reduced order model applications for rigid and aeroelastic wings utilizing the results of Cp distributions obtained from the CFD and static aeroelastic analysis of the wing, respectively. It is shown that because of the bending-torsion coupling characteristic of sweptback wings, flow separation is postponed at higher angle of attack flow conditions and this results in an enhancement of the prediction capabilities of the models developed for the aeroelastic wing compared to the rigid wing. By examining the characteristics of sweptback wings, the study highlights the critical importance of incorporating elastic effects in ROM approaches, ultimately leading to more accurate and reliable assessments of aerodynamic performance in varying flight conditions.

1.2 Motivation and Objectives

The study's motivation is driven by the need to enhance computational efficiency without compromising the accuracy and reliability of aerodynamic approximations. Traditional high-fidelity CFD solutions offer highly accurate results for real-world

aerodynamic and aeroelastic problems but come at a significant computational cost. Therefore, the data acquired from such complex studies need effective post-processing strategies to efficiently store and reconstruct the data when required, while also assessing the models under different variables. The current study aims to address this challenge by introducing and evaluating a set of reduced-order modeling techniques that not only reduce the data storage size but also enable to predict aerodynamic and structural responses across varying flow parameters for both rigid and aeroelastic wing configurations.

The proposed reduced order model approaches can be used to build a high-fidelity aerodynamic solver for wind turbine blades for very fast and more accurate calculation of the forces acting on the blades in wind turbine system simulations, for instance. Such a solver can be coupled with the wind turbine controller software and more reliable turbine power calculation can be performed owing to the high-fidelity aerodynamic solver developed based on the proposed reduced order model construction approach. Since the reduced order model is constructed utilizing the high fidelity CFD solutions taking into account the aeroelastic effects, the high fidelity, fast aerodynamic solver developed can substitute the low fidelity blade element theory which is commonly used in wind turbine simulations. Multi-body wind turbine simulation tools require a fast aerodynamics solver, hence with the proposed reduced order model both fast and high-fidelity aerodynamic analysis can be performed in wind turbine system simulations.

Another potential application of these approaches lies in the real-time control and adjustment of aerostructures. In missile systems, the flight is managed through control actuation systems, which manipulate control surfaces, such as wings or fins. By applying the ROM developed for the missile wing, the aerodynamic forces acting on these control surfaces can be accurately predicted. These forces directly influence the power consumption of the control actuation system, making them critical for optimizing the missile's battery usage during flight. Integrating real-time data from the ROM into the missile's autopilot system enables dynamic adjustments to the

control actuation system, allowing for effective power management by reducing unnecessary power consumption during various flight phases.

Similarly, by exploiting the ROM-based approaches explained in this thesis, the aerodynamic forces acting on the missile, particularly on its wings, can be efficiently computed (here it should be noted that the ROMs are more suitable than surrogate models for this purpose, as explained in the following chapters, due to the potential limitations in onboard memory of the missile guidance systems). These ROM predicted aerodynamic forces enable real-time estimation of fuel consumption throughout the flight. This predictive capability allows the missile's autopilot system to continuously adjust its trajectory and control inputs to optimize fuel usage, ensuring that the missile follows the most efficient path to its target.

The results of this work are expected to contribute to the broader field of computational fluid-structure interactions by providing insights into the comparative advantages and limitations of various surrogate modeling approaches. Ultimately, the findings of this study may pave the way for more practical, cost-effective solutions in aerodynamic and structural design optimization for both rigid and aeroelastic wings.

1.3 Limitations

This study presents the use of POD, RBF and ANN methods that provide accurate approximations across a range of flow parameters. While the developed models demonstrate satisfactory performance under steady or mildly unsteady conditions, their applicability may be constrained in highly unsteady flow regimes. In such cases, the adoption of more sophisticated modeling approaches may be necessary, and these complex flow scenarios should be addressed separately to ensure modeling reliability and predictive accuracy. The focus of this study is primarily on cases with moderate nonlinearity in the approximation of aerodynamic and structural behaviors. While this simplifies the modeling process, it does not fully capture important non-

linear effects like highly complex flow phenomena, which could affect the accuracy of the predictions for more advanced or real-world applications.

In addition, while the methods presented in this study offer substantial reductions in computational cost, the process of constructing a high-fidelity dataset, as well as developing and optimizing the reduced-order and surrogate models, can be resource-intensive, particularly when dealing with large datasets or more complex geometries. The performance of these models may also degrade if applied to complex aerodynamic configurations that differ significantly from the wing model discussed in this study.

Furthermore, the input parameters are limited to the Mach number and angle of attack, while the output parameters are confined to pressure coefficients, node positions, and stress results in this study. Although these variables provide a foundational understanding of aerodynamic and structural behavior, their restricted scope limits the overall level of detail and range of analysis. To achieve a more comprehensive and insightful evaluation, the range of parameters should be extended. This could include varying additional aerodynamic conditions, structural properties, material characteristics or operational conditions as needed, thereby enabling a more robust understanding of the system's performance under diverse scenarios.

Finally, although a benchmark wing configuration is employed to demonstrate the proposed methods, validation against experimental data is limited. The results obtained from the reduced-order models may differ when applied to real-world experimental setups, where factors like manufacturing tolerances, environmental conditions, and measurement uncertainties come into play.

1.4 Content of the Study

In the current study, the proposed methods are applied to both rigid and aeroelastic 3D wing configurations aiming to reconstruct and predict their aerodynamic and

structural metrics across varying flow parameters. The performance of the methods is demonstrated on the benchmark AGARD 445 wing with an elongated span. The rest of the study is organized as follows: Chapter 2 introduces the test wing and describes the methodologies employed for high-fidelity CFD and static aeroelastic analyses. Chapter 3 presents the POD method and details the construction of the reduced-order model for both rigid and aeroelastic wing configurations. The performance of the ROM is evaluated in terms of its ability to reconstruct the existing data. In Chapter 4, RBF is leveraged to predict the results of intermediate variables that are not readily available. To achieve this, the RBF is coupled with POD to construct a robust reduced order model. As a follow-up, a surrogate model is developed by directly applying RBF to a snapshot matrix. Both approaches are compared in terms of accuracy, computational cost and practicality. Chapter 5 introduces an ANN method to create a reduced-order model in conjunction with POD and also serving as a surrogate model. A comparative analysis of the ROM and surrogate model results against high-fidelity CFD results is conducted, providing insights into the accuracy and reliability of the proposed approaches. In all chapters the dataset is extended to include higher Mach numbers in order to increase the nonlinearity of the system. Under these conditions, the performances of the POD based ROM approaches are compared to evaluate their effectiveness in capturing the resulting more complex flow dynamics.

CHAPTER 2

HIGH-FIDELITY FULL ORDER MODEL

In this study, a 3D sweptback wing is investigated for both rigid and aeroelastic configurations. CFD analysis is conducted for the rigid wing using the commercial solver Ansys Fluent Release 21.2 [52]. For the aeroelastic case, Ansys Fluent is coupled with Ansys Mechanical Release 21.2 [53] via the system coupling tool to perform two-way static aeroelastic analysis as it is demonstrated in Figure 2.1.

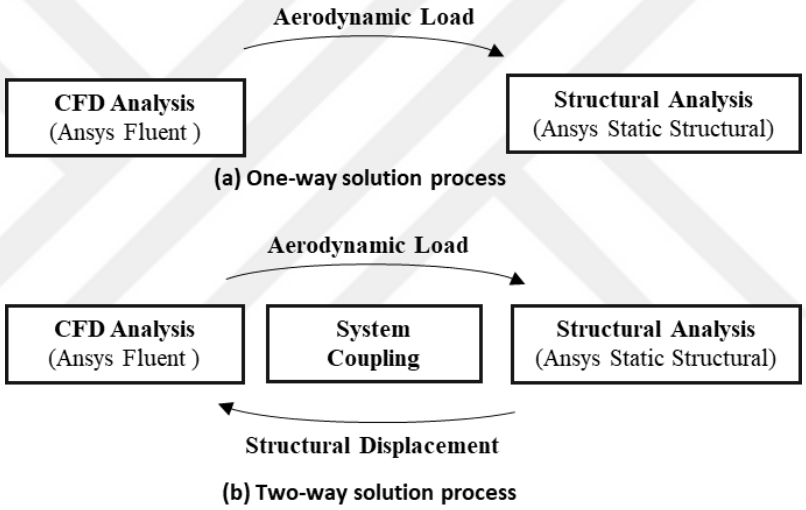

Figure 2.1. One-way solution process (a) for rigid wing and two-way solution process (b) for elastic wing

Static aeroelastic analysis is an iterative solution process during which aerodynamic loads are interpolated between nonconformal meshes on either side of the fluid-solid interface. In Ansys System Coupling module, data transfers are achieved via mapping, where the data of the target mesh are obtained by exploiting the data for the source mesh. There are two types of mapping employed in system coupling that are profile-preserving mapping and conservative mapping [54]. The goal of profile-preserving mapping is to minimize the difference between the profiles, or the distribution of data, across corresponding locations on the source and target meshes.

It is used for transferring non-conservative quantities from interface source to target regions. In the current case, profile preserving method is used for the transfer of displacement information enabling a precise representation of structural deformations. On the other hand, the goal of conservative mapping is to minimize the difference between the sum of the data at corresponding mesh locations on both the source and target domains. This mapping technique is used to transfer conservative quantities such as the aerodynamic force in the current case, from interface source to target regions.

In the current case of two-way analysis of 3D wing, surface-to-surface mapping is implemented using a projection association algorithm. After "System Coupling" has associated source and target locations, it generates data on the mapped target locations. Linear Shape Function method is used as a data-generation algorithm for profile-preserving surface-to-surface mapping. In this method, quantities located on source mesh nodes are mapped to target mesh nodes, as shown in the Figure 2.2

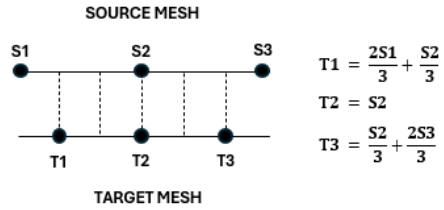

Figure 2.2. Example input and output for Linear Shape Function mapping

The linear relationship between the results of the target nodes and the source nodes is illustrated in Figure 2.2. On the other hand, Intersect-Scatter-Gather method is used for conservative surface-to-surface mapping. In this method, data located on the source mesh elements are mapped to target mesh elements, as shown in Figure 2.3.

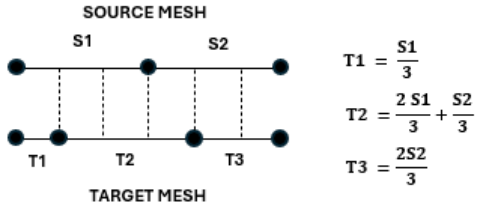

Figure 2.3. Example input and output for conservative Intersect-Scatter-Gather mapping

As illustrated in Figure 2.3, in this case the size of each intersected region relative to the size of the corresponding source element is used. The result of the target element is directly proportional to the size of the source element.

Two-way analysis iteration starts with the CFD analysis of the rigid wing model. Due to elastic nature of the wing, it deforms under the aerodynamic load; this deformation is obtained after importing the loads to the structural part and performing structural analysis. Following this, the mesh for next aerodynamic calculation is regenerated based on the deformed wing configuration. This process of structural analysis is repeated until both the aerodynamic load and the structural deformation converge within a specified tolerance, or until the maximum number of iterations is reached. In this study, a dynamic mesh is defined at the fluid-solid interface with diffusion-smoothing method which allows the interior nodes to move in accordance with the deforming boundary while maintaining the same number of nodes and their connectivity throughout the analysis.

The solutions obtained from the CFD analysis of the rigid wing and static aeroelastic analysis of the elastic wing are regarded as the high-fidelity results since they reflect the real-life phenomena with a significant degree of accuracy.

2.1 AGARD 445.6 Wing

The wing model utilized in this study is AGARD 445.6 Wing, a well-known test case for aeroelastic problems, employed in wind tunnel experiments to investigate its flutter characteristics in the Langley Transonic Dynamics Tunnel [55]. The AGARD

445.6 features a low-aspect-ratio sweptback wing with a NACA 65A004 airfoil. The panel dimensions of the wing are given in Figure 2.4.

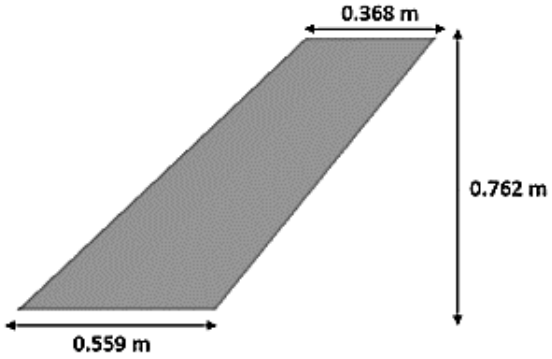

Figure 2.4. AGARD 445.6 wing panel dimensions

The wing used in the experimental study was constructed from laminated mahogany which is an orthotropic material. The stiffness of this model is reduced by drilling holes through the wing to obtain flutter at the desired Mach number. The associated material properties can be found in reference [57]. The equivalent analysis model is validated by comparing the natural frequencies and mode shapes with the actual results given in reference [55] (Figure 2.5).

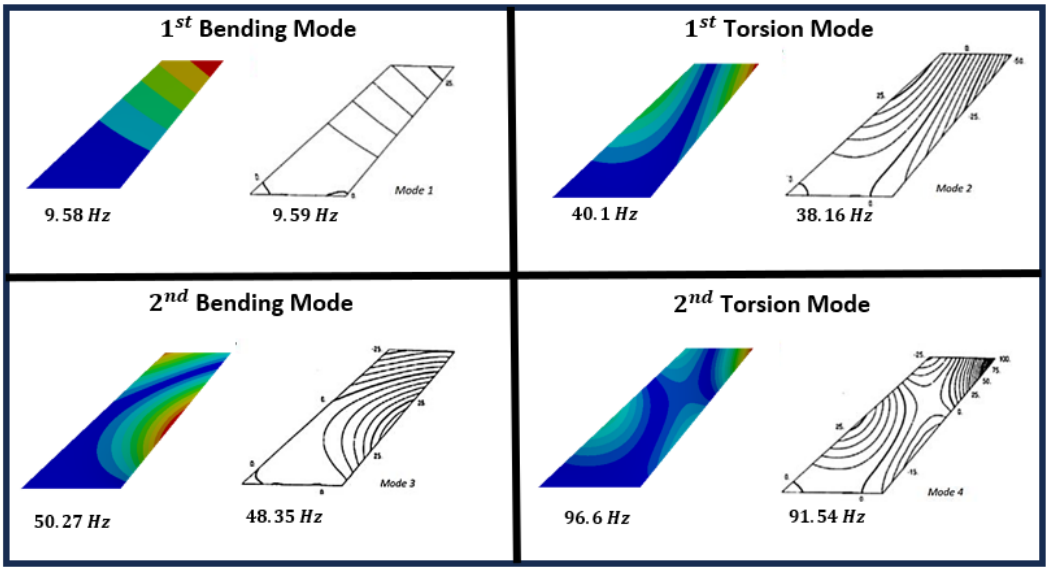

Figure 2.5. Comparison of natural frequencies and mode shapes with literature [55]

Modal analysis is conducted using Ansys Mechanical [53] tool and AGARD wing is modeled using tetrahedral elements with 152653 nodes and 92627 elements. The structural mesh configuration is given in Figure 2.6.

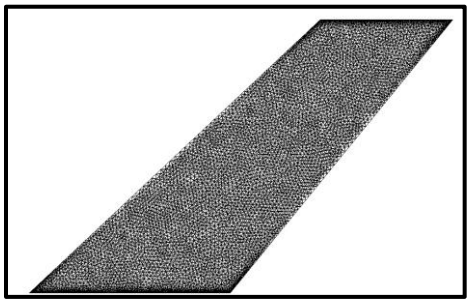

Figure 2.6. Structural mesh configuration of the AGARD 445.6 wing

The fluid domain is made from a half cylindrical prism cut by the symmetry plane and the wing is placed inside the half cylindrical prism (Figure 2.7). The CFD mesh domain consists of 4 node linear tetrahedral elements mainly and 6 node linear wedge and 5 node linear pyramid elements. There are 2310150 elements with 570659 nodes in total.

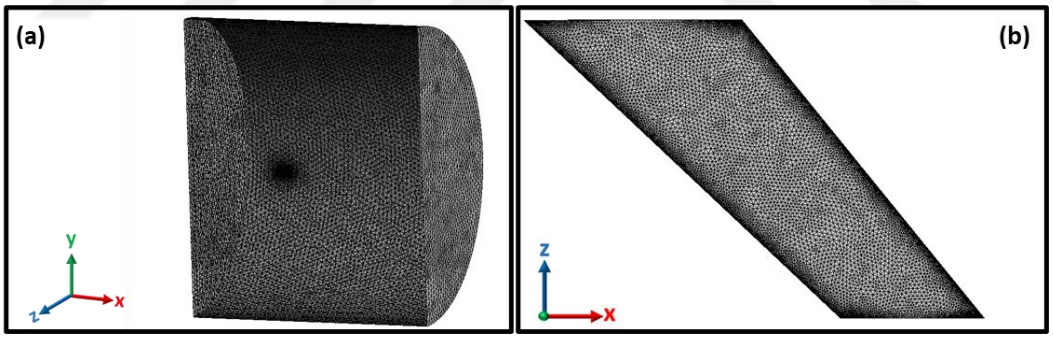

Figure 2.7. CFD mesh configuration of the fluid domain (a) and detailed view of the CFD mesh configuration of the wing profile (b)

CFD analysis is conducted using Ansys Fluent [52] tool. Far-field boundary condition is defined on the surfaces of the prism except the surface where root of the wing is located. This surface has a symmetric boundary condition. For the wing surface, no slip wall condition is defined. Finer mesh is applied on the edges of the wing to obtain an accurate airflow on the wing and also to avoid convergence issues.

In addition, the mesh at the zone, near the wall of the wing, is refined to keep y^+ below 1 at the boundary layer (Figure 2.8).

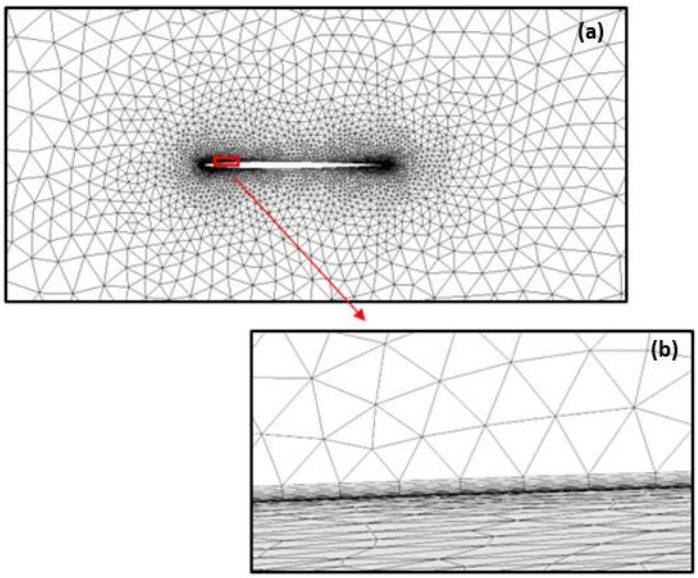

Figure 2.8. Root section of the wing mesh (a) and the detailed view of the boundary layer (b)

For the flow conditions, compressible and viscous flow with the SST k-w turbulence model assumption is used. To validate the CFD model developed for the current study, the Cp distribution results are compared with the findings of Cai et al. [56] at the same flow conditions of 0.85 Mach and 5° AOA. The comparative results are given at 67% and 34% span from the root in Figure 2.9.

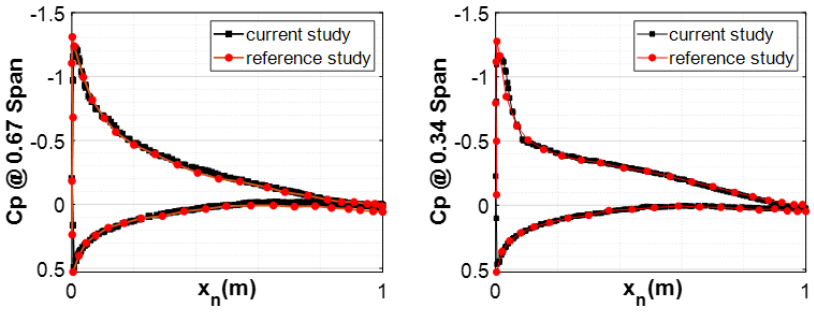

Figure 2.9. Comparison of Cp distribution with literature at 0.67 and 0.34 span locations [56]

It can be seen that the results of both analyses are well-matched with each other. Additionally, the static aeroelastic results are evaluated and compared to further

verify the accuracy of the model. The Cp distribution outcomes derived from the two-way analysis are shown in Figure 2.5.

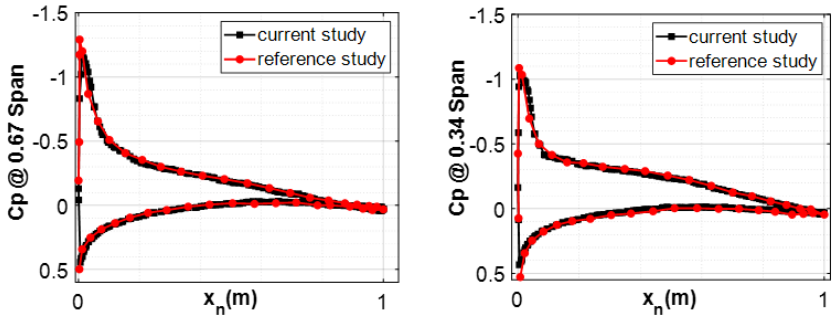

Figure 2.10. Comparison of aeroelastic Cp distribution with literature at 0.67 and 0.34 span locations [56]

Similarly, the Cp distribution results of two-way analysis show a good agreement with the literature. In this case, as the aeroelastic wing undergoes a bending deformation, effective AOA decreases due to the bending-torsion coupling that occurs in the sweptback geometry. Consequently, this result in an overall decrease in Cp at the airfoil sections. The decrease of aeroelastic Cp distribution can be seen more clearly at Figure 2.11.

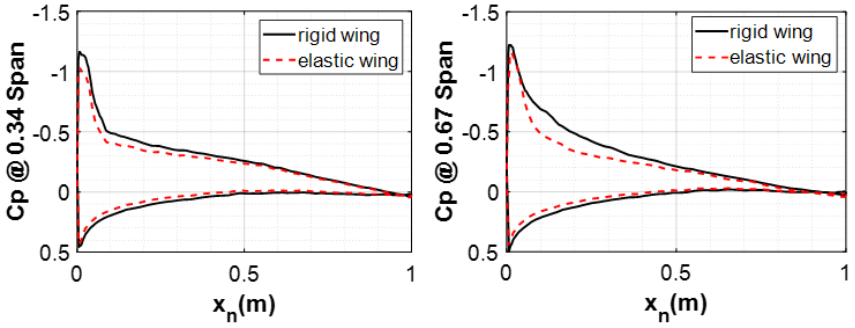

Figure 2.11. Comparison of Cp distribution of rigid and elastic wings at 0.67 and 0.34 span locations [56]

Figure 2.11 shows that since the deflection is higher as getting close to the wing tip the difference of Cp distribution is more remarkable at 0.67 span location.

Furthermore, the vertical deflection of the leading and trailing edges resulting from the two-way analysis along the span are shown and compared with the literature as given in Figure 2.12.

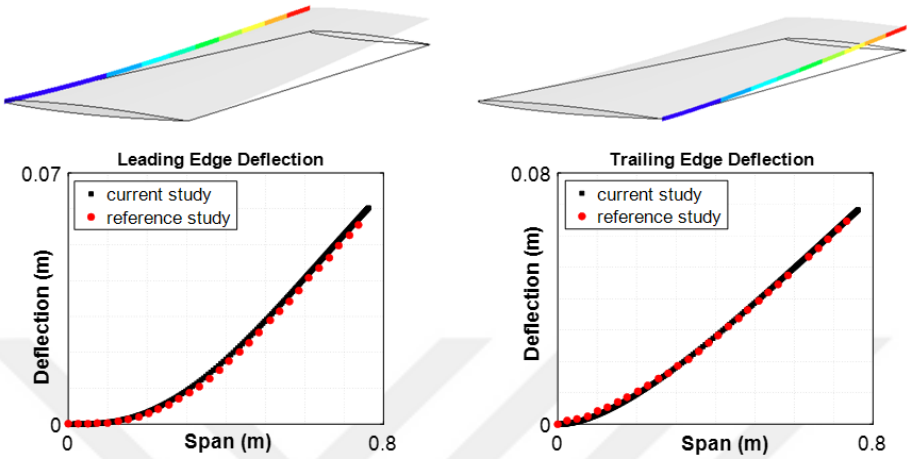

Figure 2.12. Deflection of the leading and trailing edges [56]

The deflections of the wing edges are also well-matched with the study of Cai et al [56]. Moreover, the maximum wing deflection and lift coefficient obtained from different mesh sizes are compared to ensure the accuracy and reliability of the computational results. The purpose is to identify the optimal mesh configuration that balances computational efficiency with the fidelity of the aerodynamic and structural predictions. By assessing the convergence of the lift coefficient and the maximum wing deflection, the sensitivity study confirmed that the current mesh (fine mesh) is sufficiently refined to capture the flow phenomena accurately. The comparative results are given in Table 2.1.

Table 2.1 Comparison of the results of different mesh sizes

	Element Number	Node Number	C_L	Maximum Wing Deflection (m)
Coarser mesh	1144191	264904	0.2675	0.0691
Fine Mesh	2310158	570659	0.2670	0.0683
Finer Mesh	2921285	726109	0.2668	0.0683

In addition, the Cp distribution results from static aeroelastic analyses with different mesh sizes are given in Figure 2.13.

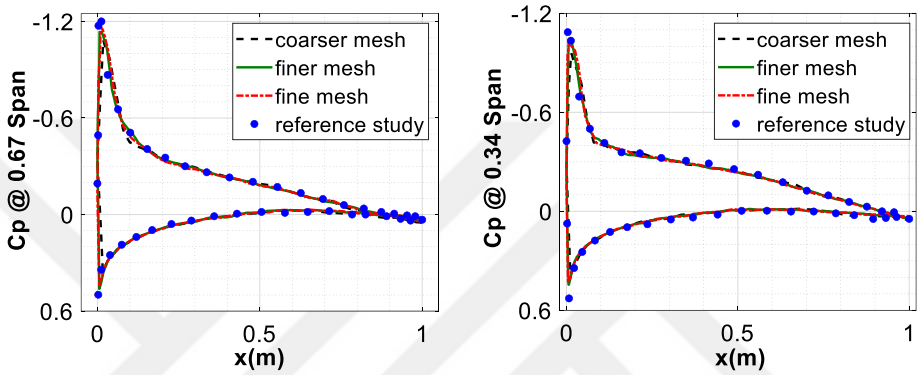

Figure 2.13. Comparison of Cp distribution for different mesh sizes at 0.67 and 0.34 span locations [56]

The comparative study presented in Table 2.1 and Figure 2.13 indicates that the fine mesh configuration is able to predict the results obtained by Cai et al. [40] accurately. Notably, it yields almost the same results to those acquired by the finer mesh. However, the Cp distribution results reveal that the fine mesh shows better agreement with the reference study compared to the coarser mesh. Consequently, the fine mesh case is chosen for further use and it is adapted for the elongated AGARD 445.6 wing by preserving the element sizes. The details of the elongated AGARD 445.6 wing are provided in the following section.

2.2 Elongated AGARD 445.6 Wing

In the current study, span of the AGARD 445.6 wing is increased about 30% which leads to a further decrease in the stiffness of the wing, making the static aeroelastic

effects more remarkable. AGARD 445.6 wing with elongated span dimensions is given in Figure 2.14 with the original AGARD 445.6 wing.

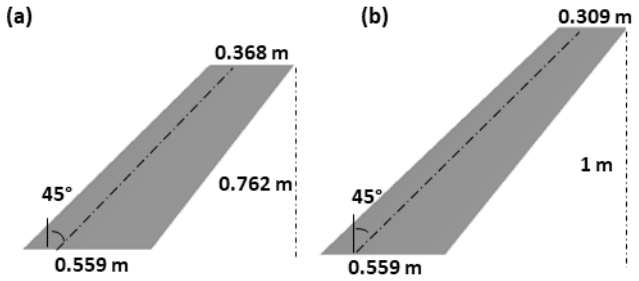

Figure 2.14. Dimensions of the baseline AGARD 445.6 wing (a) and the AGARD 445.6 wing with elongated span (b)

The elongated wing profile results in reduced structural stiffness and increased mass, leading to a decrease in the natural frequencies. The comparison of the natural frequencies between the AGARD 445.6 wing and the elongated AGARD 445.6 wing is shown in Table 2.2.

Table 2.2 Comparison of the modal frequencies

	1st Bending Mode (Hz)	1st Torsion Mode (Hz)	2nd Bending Mode (Hz)	2nd Torsion Mode (Hz)
AGARD 445.6 [55]	9.599	39.165	48.348	91.545
AGARD 445.6 with 1m Span	5.894	25.607	36.753	62.420

The structural mesh of the solid, elongated wing is given in Figure 2.15, that consists of 101288 tetrahedral elements with 171702 nodes. The mesh sensitivity analysis of different mesh sizes is given in Appendix A.

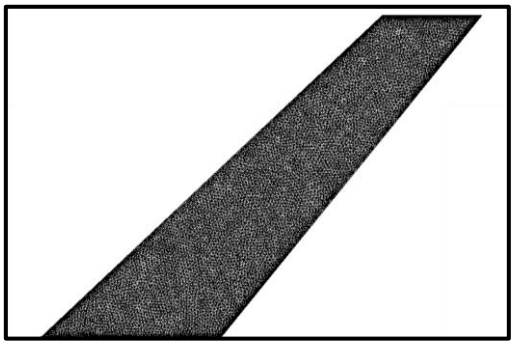

Figure 2.15. Structural mesh configuration of the elongated AGARD 445.6 wing

Since the results of modal, CFD and static aeroelastic analyses of AGARD 445.6 wing are validated with the literature, the same procedure is followed for the elongated AGARD wing. Consequently, the same mesh configuration is employed for the elongated wing which is presented in Figure 2.16.

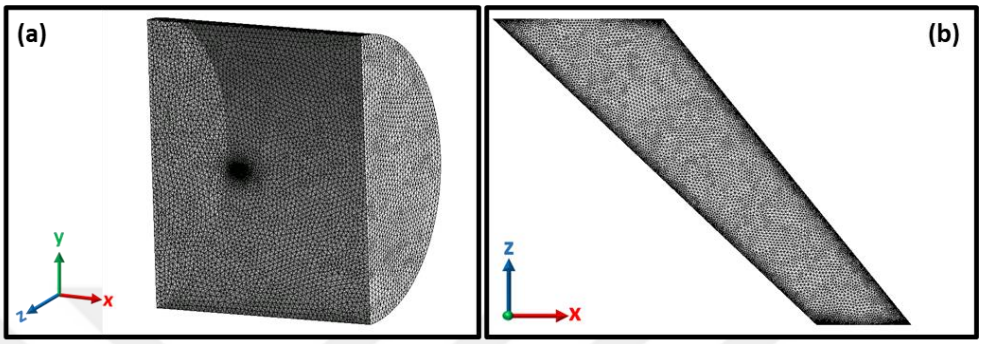

Figure 2.16. CFD mesh configuration of the fluid domain (a) and detailed view of the CFD mesh configuration of the wing profile (b)

For the elongated wing in fluid domain, there are 20366 nodes on the surface of the wing in total, each of which is used to obtain the data to create a snapshot matrix. It should be noted that constructing a snapshot matrix involves repeated high-fidelity analyses which requires a great computational cost. However, this expense can be regarded as an investment in future efficiency. The upfront costs associated with numerous high-fidelity analyses ultimately enhance the overall efficiency of future modeling endeavors by significantly decreasing computational time and enabling great accuracy.

CHAPTER 3

REDUCED ORDER MODELING WITH PROPER ORTHOGONAL DECOMPOSITION

3.1 Proper Orthogonal Decomposition (POD) Method

POD is an effective statistical tool that is able to extract dominant features from a large data set. The data set can be obtained from either the results of experiments or simulations for one or more variables of interest. Exploiting the data set, a snapshot matrix of $\mathbf{Z} \in \mathbb{R}^{nxm}$ is created for the 'm' number of results of a system for a changing parameter and the 'n' number of nodes or points where the data are taken.

$$[\mathbf{Z}]_{nxm} = \begin{bmatrix} z_1^1 & \cdots & z_1^m \\ \vdots & \ddots & \vdots \\ z_n^1 & \cdots & z_n^m \end{bmatrix} \tag{1}$$

It is common to subtract from each row of $\mathbf{Z}$ the mean value of that row, to create a modified snapshot matrix. Defining $\widetilde{\mathbf{z}_k} = \frac{1}{m}\sum_{i=1}^{m} \mathbf{z}_i$ as the mean of the k^{th} row, the mean vector $\tilde{\mathbf{z}}$ is formed. Then the modified snapshot matrix is conducted as:

$$\{\bar{\mathbf{z}}\}_i = \{\mathbf{z}\}_i - \tilde{\mathbf{z}}, \qquad i = 1,2,\dots,m \tag{2}$$

where m is the total number of snapshots.

The aim of the POD method is to first extract the optimal orthogonal basis vectors or the POD modes from the sampled parameter space, the snapshot matrix. From these basis vectors, the first $m_s < m$ modes that contain sufficient information provided by the snapshots are chosen. Singular value decomposition (SVD) or method of snapshots (MOS) techniques can be used for this purpose.

Singular Value Decomposition

SVD technique can be used directly to obtain POD modes. SVD applied on the modified snapshot matrix is written in the form of,

$$\bar{\mathbf{Z}}_{\mathrm{nxm}} = \mathbf{U}_{\mathrm{nxm}}\, \mathbf{\Sigma}_{\mathbf{m}\mathrm{xn}}\, \mathbf{V}^{\mathrm{T}}{}_{\mathrm{nxm}} \tag{3}$$

where, columns of **U** are the eigenvectors of $[\bar{\mathbf{Z}}][\bar{\mathbf{Z}}]^{\mathrm{T}}$ and are known as the left-singular values of $\bar{\mathbf{Z}}$, columns of **V** are the eigenvectors of $[\bar{\mathbf{Z}}]^{\mathrm{T}}[\bar{\mathbf{Z}}]$ and are known as the right-singular values of $\bar{\mathbf{Z}}$ and diagonals of **Σ** are the square of the eigenvalues of $[\bar{\mathbf{Z}}]^{\mathrm{T}}[\bar{\mathbf{Z}}]$ also known as the singular values of $\bar{\mathbf{Z}}$. The diagonal elements are ordered in a decreasing way, and they allow to compute the fraction of the total energy associated with each mode,

$$\%\mathrm{E} = \frac{\sum_{\mathrm{i}=1}^{\mathrm{m_s}} \lambda_{\mathrm{i}}}{\sum_{\mathrm{i}=1}^{\mathrm{m}} \lambda_{\mathrm{i}}} \tag{4}$$

Eigenvalues quantify the significance of the basis vectors in expressing the information contained in the data, with the first POD basis vector being the most relevant and the last POD basis vector the least. The columns of **U** represent the orthogonal POD modes and the number of modes can be significantly reduced by taking into account the amount of energy captured.

Method of Snapshots

When the snapshot matrix has a few snapshots but excessive number of nodes (n>>m), the method of snapshots is an effective alternative that can be applied. In this method, eigenvectors and eigenvalues of the covariance modified matrix ($\mathbf{Z}^{\mathrm{T}}\mathbf{Z}$) is found. The covariance matrix has a size of mxm that is much less than the original snapshot matrix, therefore easier to handle.

In this method, POD basis vectors are calculated as,

$$\mathbf{U}_{\mathrm{j}} = \frac{1}{\mathrm{s_j}} \sum_{\mathrm{l}=1}^{\mathrm{m}} (\mathbf{V}_{\mathrm{j}})_{\mathrm{l}} \mathbf{z}_{\mathrm{l}} \qquad \mathrm{j} = 1, 2, \ldots, \mathrm{m} \tag{5}$$

where, s and **V** stand for the square root of eigenvalues and eigenvectors, respectively and m is the number of snapshots. Similar to the SVD method, the eigenvalues of the covariance matrix quantify the importance of the basis vectors and enable to determine the number of dominant modes, m_s. The percentage of energy captured by the modes is calculated as,

$$\%E = \frac{\sum_{i=1}^{m_s} s_i}{\sum_{i=1}^{m} s_i} \tag{6}$$

After obtaining the modes exploiting either the SVD or the method of snapshots, the solution at a particular parameter that already exists in the initial sample data is reconstructed as,

$$\mathbf{z}_j^{rc} = \tilde{\mathbf{z}} + \sum_{i=1}^{m_s<m} a_{ji}\mathbf{U}_i \qquad j = 1, 2, \ldots, m \tag{7}$$

where z^{rc} denotes the reconstructed result. Equation (7) gives the solution as the linear combination of a set of orthonormal basis vectors and the corresponding coefficients a_{ji} which are also referred as basis/scalar/projection/POD coefficients. The POD coefficients are obtained by projecting the solutions onto the POD modes as,

$$a_{ji} = \mathbf{z}_j^T\mathbf{U}_i \qquad j = 1, 2, \ldots, m;\ i = 1, 2, \ldots, m_s \tag{8}$$

Equation (7) is used to obtain the result of the system at a desired parameter for which a snapshot has already been calculated; however, it can also be used to predict the solutions at intermediate parameters in the sampling space by creating a surrogate model having parameters as input and the POD coefficients as output.

3.2 Reconstruction of the Results Based on the POD Method

In the current study, two critical flow parameters that are angle of attack (AOA), and Mach number (M) are taken as variables. The analyses are conducted within the subsonic regime, specifically spanning Mach numbers from 0.55 to 0.85, with uniform increments of 0.05. At the same time, the AOA varies between 1º and 5º, with increments of 0.5º. This systematic approach results in a dataset comprising a total of 63 distinct snapshots. The parameter pairs, which are also referred to as input data are summarized in Figure 3.1.

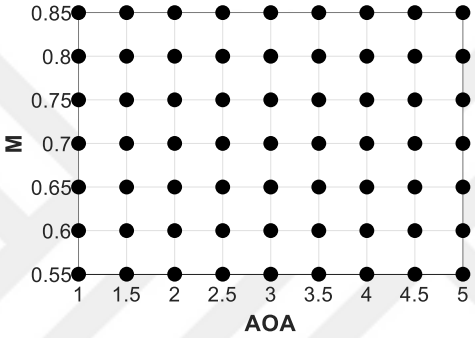

Figure 3.1. Lattice of snapshots

Based on the high-fidelity analysis results obtained for the input data, POD is initially performed on the rigid wing configuration. Then, the aeroelastic wing model is investigated, employing the results of the two-way coupled approach that integrates CFD and static structural analysis. Cp distribution is aimed as the aerodynamic output for both rigid and aeroelastic wings. Moreover, for the aeroelastic wing, displacement and von Mises stress distributions are also taken as the structural outputs providing crucial insights into the structural performance.

Cp distribution is displayed on the 3D wing configuration, however to distinguish the differences in Cp distribution obtained by high fidelity analyses and reduced order model predictions, variation of the Cp along the 2D sections of the wing are also exploited. For the spanwise section of the wing, a cut is made through the aerodynamic center, while the chordwise section is taken along the chord line located 0.8 m from the wing root. The resulting 2D sections are illustrated in Figure 3.2.

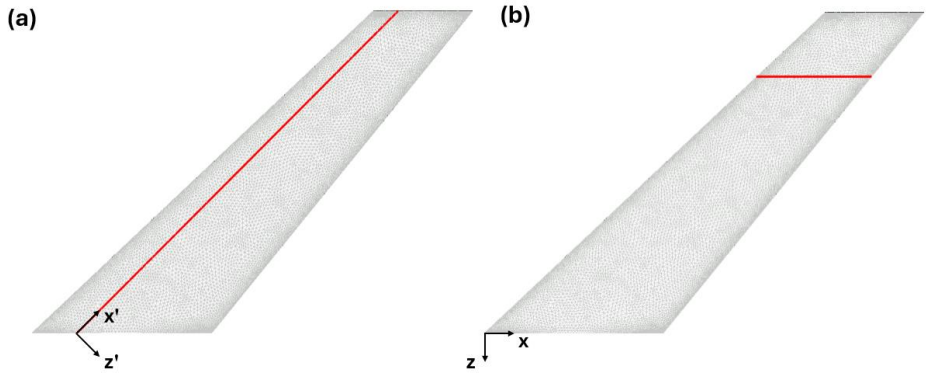

Figure 3.2. Spanwise (a) and chordwise (b) sections taken from the wing

The node positions used for result comparisons across different cases are taken from the spanwise and chordwise sections depicted in Figure 3.2. Figure 3.3 shows the nodes located within intervals of 0.0015 m from the spanwise section and 0.004 m from the chordwise section.

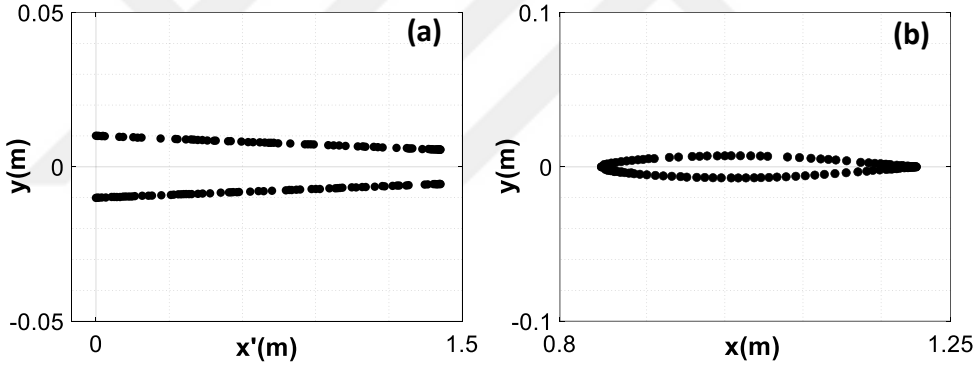

Figure 3.3. Spanwise (a) and chordwise nodes (b)

For comparing the results of the reduced-order model and full-order solutions, the normalized root mean square error (NRMSE) and R^2 error metrics are employed, defined as follows:

$$\mathrm{RMSE} = \sqrt{\frac{\sum_{i=1}^{N}(z_{a,i} - z_{p,i})^2}{N}} \qquad \mathrm{NRMSE} = \frac{\mathrm{RMSE}}{(z_{a,i})_{max} - (z_{a,i})_{min}} \tag{9}$$

$$R^2 = 1 - \frac{\sum_{i=1}^{N}(z_{a,i} - z_{p,i})^2}{\sum_{i=1}^{N}(z_{a,i} - \bar{z_a})^2} \tag{10}$$

where $z_{a,i}$, $z_{p,i}$ and $\overline{z_a}$ denote the actual, predicted and average values of the output variables (such as Cp, wing displacement and von-Mises stress), respectively; i represents the node index and N is the total number of nodes.

3.2.1 Three-Dimensional Rigid Wing Configuration

A reduced order model is initially constructed for the rigid wing configuration using POD. By applying the SVD and MOS techniques, the energy of the system captured by each mode along with their corresponding basis functions are obtained. While both methods yield identical results, it is noteworthy that the MOS technique is significantly faster than SVD, as given in Table 3.1.

Table 3.1. Computational time of SVD and MOS methods*

Singular Value Decomposition (SVD)	Method of Snapshots (MOS)
23.5 s	**0.09 s**

* On an AMD Ryzen 7-5800X 8-Core Processor & 3.80 GHz computer

It should be highlighted that the number of nodes on the surface of the 3D wing greatly exceeds the number of variables. As a result, MOS technique proves to be significantly more efficient in terms of computational speed. Consequently, the current study employs MOS technique. For the rigid wing, fraction of energy captured with the number of modes is shown in Figure 3.4. It is seen that 1st mode captures approximately 57.48%, 2nd mode 12.15% and 3rd mode 9.63% of the energy. In order to reach at least 90% of the energy, 8 modes are required to be included. The accumulated energy for Cp distribution with respect to mode number is shown also in Figure 3.4.

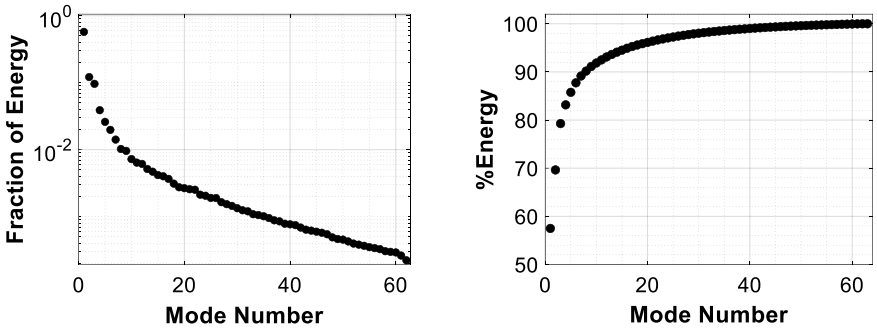

Figure 3.4. Fraction of energy and accumulated energy (% energy) for the Cp of the rigid wing

By exploiting these modes, pressure coefficient results for each angle of attack and Mach number pair in the snapshot domain given in Figure 3.1 are reconstructed and NRMSE and R^2 error values are presented for each reconstructed result using 1 and 8 modes in Figure 3.5. The results of the other modes less than 8, are given in Appendix B.

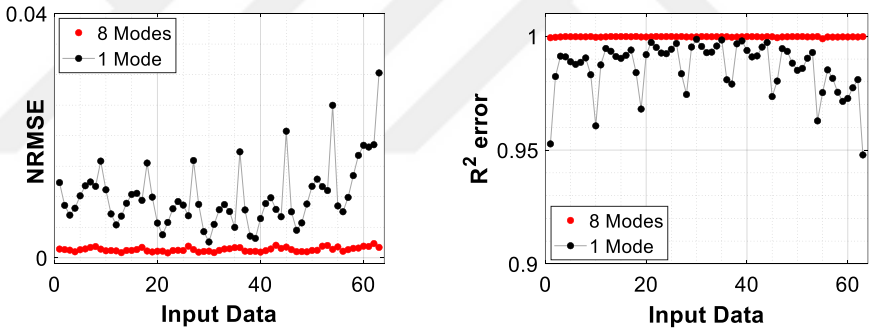

Figure 3.5. NRMSE and R^2 errors for 1 mode and 8 modes for the rigid wing

Graphs given in Figure 3.5 represents NRMSE and R^2 error values respectively for the Cp distribution across each AOA and M pair within the snapshot domain. As the accuracy of the results increases, R^2 values approach 1; while the NRMSE values approach 0. Therefore, Figure 3.5 indicates that, for the case with 8 modes capturing 90% of the energy, the reconstructed results for the snapshot matrix exhibit high accuracy. Conversely, the results obtained using only 1 mode are less accurate, as expected, given that they capture only 57.48% of the energy. Specifically, for the 1 mode case, the least accurate result corresponds to the final input variable pair of M=0.85 and AOA=5°, as indicated by both NRMSE and R^2 error metrics, which

gives the values of 0.948 and 0.030, respectively. To clearly compare the effect of mode numbers on the results under this flow condition, the pressure coefficient distributions on the top and bottom surfaces of the wing, obtained from high-fidelity CFD analysis and reconstructed using 1 mode and 8 modes, are presented on the 3D wing in Figure 3.6.

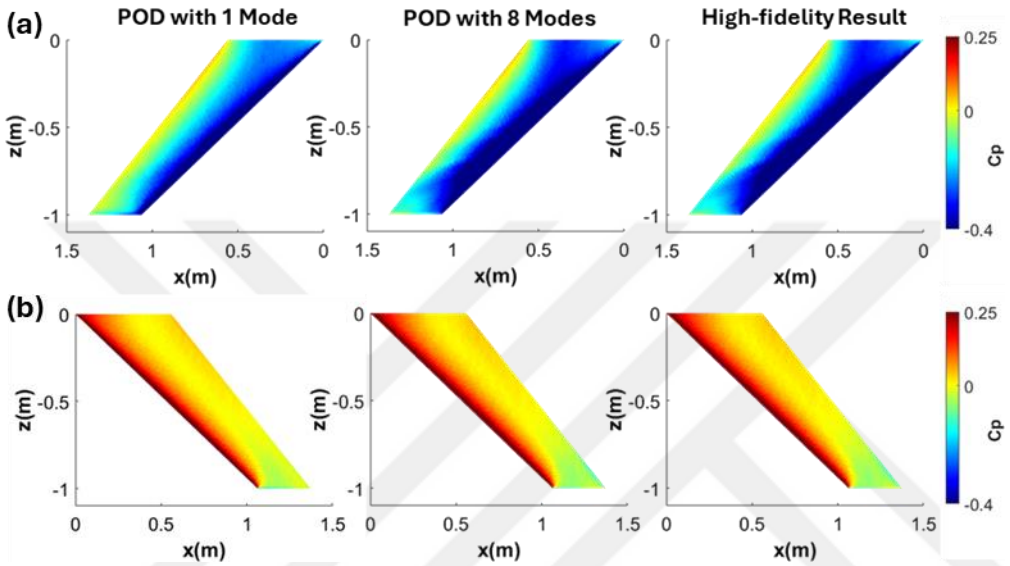

Figure 3.6. Cp distribution on the top (a) and bottom (b) wing surfaces for the high-fidelity analysis and reconstructed Cp for 1 mode and 8 modes (M=0.85 and AOA=5º)

For this flow condition, the pressure coefficient distribution reconstructed using a single mode exhibits remarkable discrepancies, particularly on the top surface, when compared to the actual results. In contrast, the distribution reconstructed with 8 modes reveals no notable differences from the high-fidelity data. To enable a more detailed comparison, the pressure coefficient distributions at the spanwise and chordwise sections, as indicated in Figure 3.3, are presented in Figure 3.7. This approach clearly highlights variations between the high-fidelity results and those reconstructed using different numbers of modes.

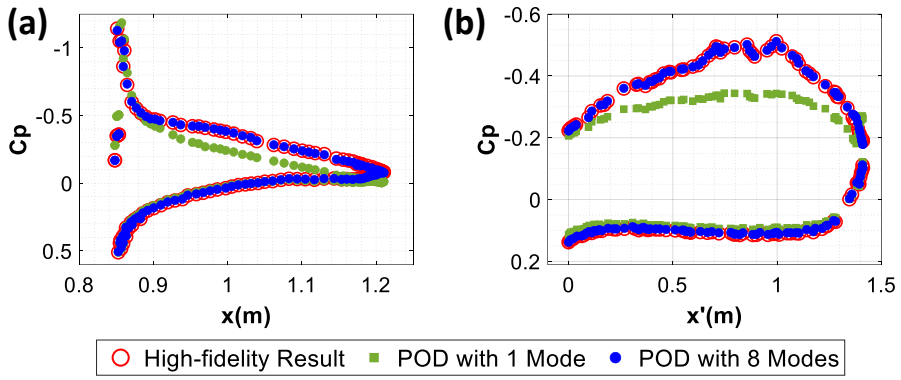

Figure 3.7. Variation of Cp along the chordwise (a) and spanwise (b) wing sections for the high-fidelity analysis result and the reconstructed Cp for 1 mode and 8 modes (M=0.85 and AOA=5°)

Figure 3.7 shows that when only a single mode is used for the reconstruction, a significant mismatch exists between the pressure coefficients particularly on the top surface of the wing in the spanwise and chordwise sections analyzed. Conversely, reconstruction using 8 modes achieves an almost perfect match. However, it should also be noted that in the 8 modes case, according to the R^2 error metric, the least accurate flow case is the 55^{th} instance, corresponds to a Mach number of 0.85 and AOA of 1°. For this flow condition R^2 is 0.9989. In addition, based on the NRMSE metric, the least accurate flow case is 62^{nd} which has a Mach number of 0.85 and AOA of 4.5° resulting in a NRMSE of 0.0023. To further investigate these discrepancies relative to the high-fidelity results, the pressure coefficient distributions along the 2D wing sections for the respective cases are analyzed and presented in Figure 3.8.

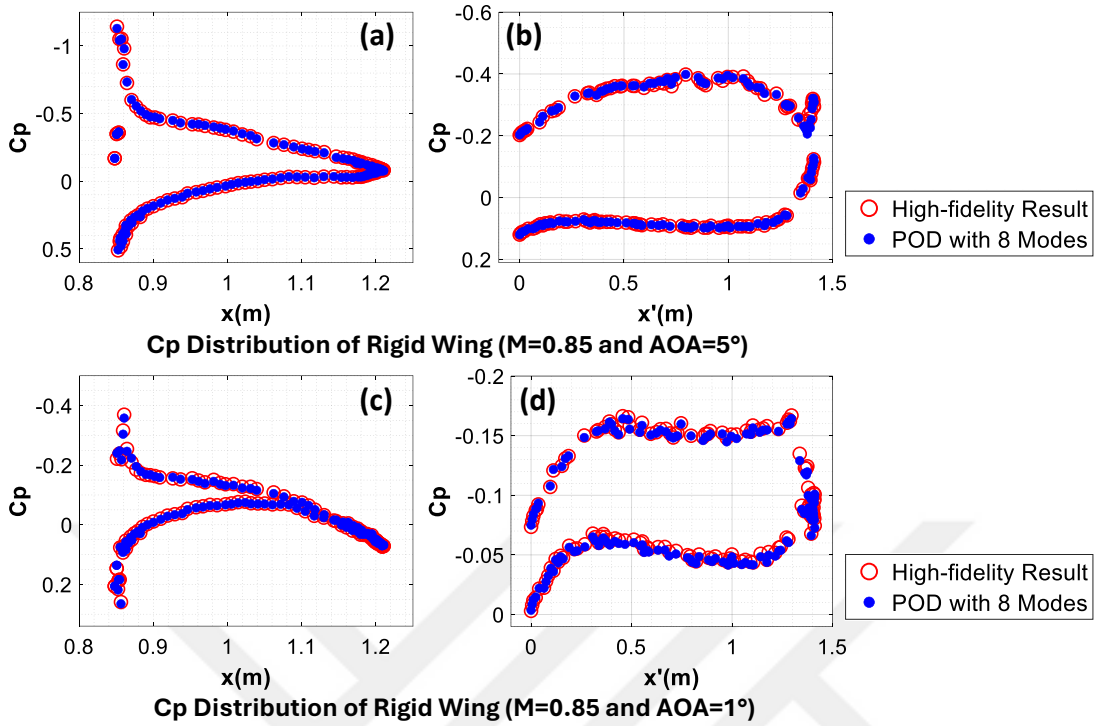

Figure 3.8. Variation of Cp along the chordwise ((a) & (c)) and spanwise ((b) & (d)) wing sections for the high-fidelity analysis result and the reconstructed Cp for the least accurate flow conditions

The least accurate flow conditions indicated by both error metrics reveal only a minor difference between the high-fidelity results and those reconstructed using 8 POD modes. This difference is considered acceptable given the significant reduction in the number of modes. While increasing the number of modes would undoubtedly enhance the precision of the results, it should be acknowledged the inherent trade-off between model order reduction and accuracy. The analysis reveals that capturing 90% of the system's energy is sufficient to achieve highly accurate outcomes. Moreover, it is essential to note that, despite the slight deviations observed when compared to the high-fidelity results, the distributions depicted in Figure 3.8 represent the least accurate cases across the flow domain; that means for other cases, the accuracy of the 8-mode results is higher. Thus, for the purposes of predictions and analyses utilizing the reduced-order model, this study employs 8 modes for the rigid wing configuration, achieving an effective balance between computational efficiency and accuracy.

3.2.2 Three-Dimensional Aeroelastic Wing Configuration

As a next reconstruction case, the aeroelastic wing is investigated. Contrary to rigid wing, the aeroelastic wing undergoes deformation in response to aerodynamic loads. A two-way FSI analysis is performed through an iterative process until the deformed equilibrium configuration is reached. From the Cp results at the end of the two-way FSI process, a snapshot matrix is constructed for the aeroelastic wing. It should be noted that, for the aeroelastic wing, the angle of attack specified in the snapshot matrix corresponds to the rigid angle of attack, rather than the effective angle of attack resulting from the equilibrium deformation of the aeroelastic structure. Employing the MOS technique, it is seen that 1st mode captures approximately 71.38%, 2nd mode 10.35% and 3rd mode 4.6% of the energy; in this case, 5 modes are required to capture 90% of the energy (Figure 3.9).

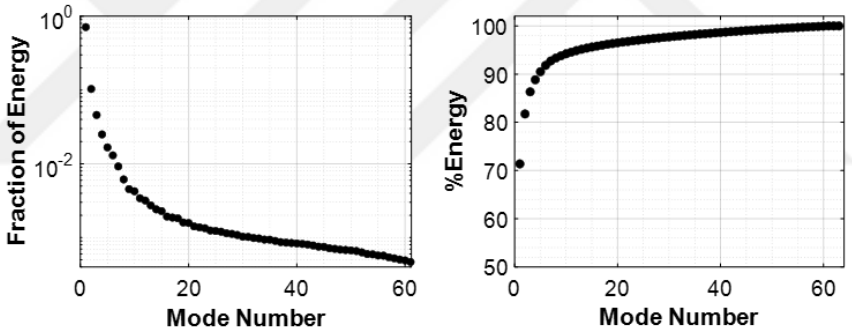

Figure 3.9. Fraction of energy and accumulated energy (% energy) for the Cp of the aeroelastic wing

In the case of aeroelastic wing, the node positions shift due to the wing's deflection, unlike the rigid wing where node positions remain constant. As a result, each analysis case necessitates its own distinct node positions. To accurately represent the Cp distributions, separate snapshot matrices are constructed for the x, y, z coordinates of the nodes. The MOS technique is also applied to these snapshot matrices. Figure 3.10 gives the fraction of energy for the x, y and z positions of the nodes (the logarithmic plots are also provided in Appendix B). From Figure 3.10, it is seen that 1st mode captures 97.1% of energy for the x position, 99.5% of energy for the y position and 97.4% of energy for the z position of the nodes. Hence, it is concluded

that using only a single mode is sufficient for the reconstruction of the nodal positions, indicating a significant reduction of order.

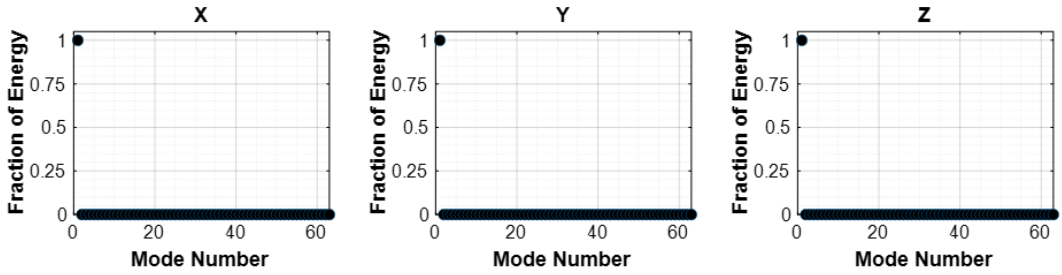

Figure 3.10. Fraction of energy for the x, y, z position of the nodes

Figure 3.11 presents the NRMSE and R^2 error values for the reconstructed Cp distributions compared to the actual results, corresponding to each Mach number and AOA pair within the snapshot matrix. The results of the other modes are given in Appendix B.

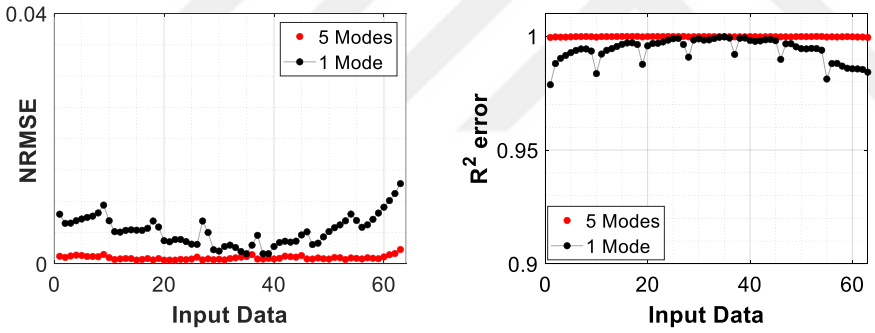

Figure 3.11. NRMSE and R^2 errors for 1 mode and 5 modes for the aeroelastic wing

Here it should be highlighted that for the aeroelastic wing case, there is an overall decrease in the error values compared to rigid wing. Similar to the rigid wing analysis, when only 1 mode is employed, the highest error belongs to the last variable pair of M=0.85 and AOA=5º according to the NRMSE with a value of 0.013. However, according to the R^2 metric, the first variable pair exhibits the highest error; specifically for the last variable pair R^2 =0.9842, while for the first pair (M=0.55 and AOA=1º) R^2 =0.9787. Thus, for this case, the reconstructed Cp distributions using 1 mode and 5 modes are displayed on the 3D wing for both first and last flow

conditions, alongside the Cp distribution obtained from the high fidelity static aeroelastic analysis in Figure 3.12 and Figure 3.13.

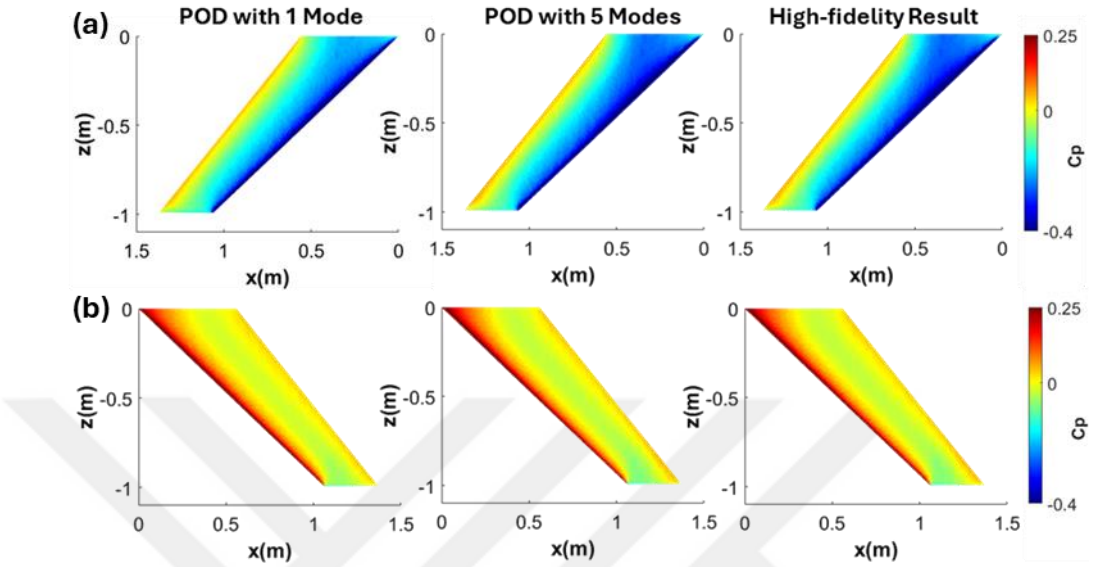

Figure 3.12. Cp distribution on the top (a) and bottom (b) wing surface for the high-fidelity analysis and reconstructed Cp for 1 mode and 5 modes (M=0.85 and AOA=5º)

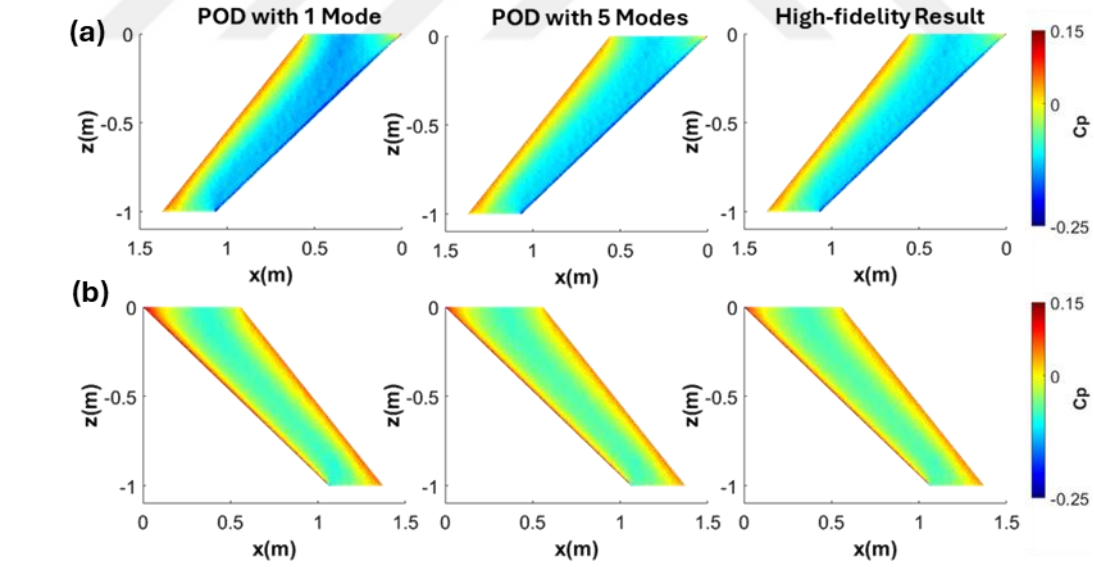

Figure 3.13. Cp distribution on the top (a) and bottom (b) wing surface for the high-fidelity analysis and reconstructed Cp for 1 mode and 5 modes (M=0.55 and AOA=1º)

As in the rigid wing case, reconstructed pressure coefficient distribution obtained by a single mode is similar as the actual pressure coefficient distribution, albeit with

some noticeable differences. When utilizing 5 modes, the reconstructed pressure coefficient distributions on both the upper and lower wing surfaces exhibit no noticeable differences from the actual pressure distributions. The variations of the pressure coefficient along the spanwise and chordwise sections shown in Figure 3.2 are presented in Figure 3.14.

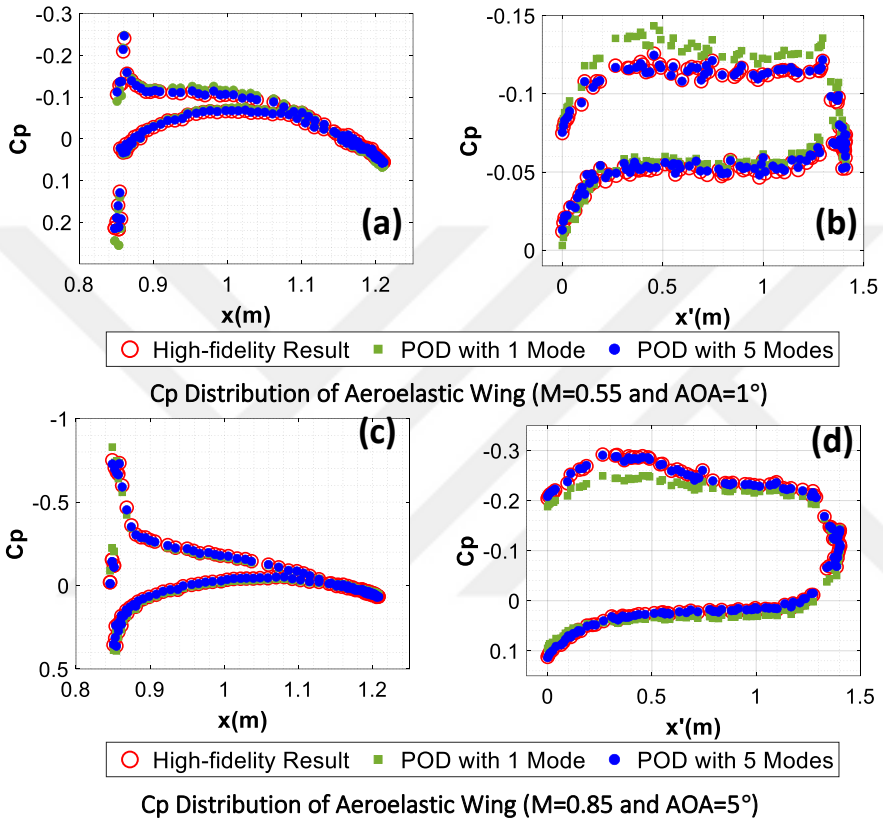

Figure 3.14. Variation of Cp along the chordwise ((a) & (c)) and spanwise ((b) & (d)) wing sections for the high-fidelity analysis result and the reconstructed Cp for 1 mode and 5 modes

It is evident from the figures that when only 1 mode is considered for reconstruction, a noticeable mismatch arises between the pressure coefficients in the spanwise and chordwise sections analyzed. This discrepancy is expected since capturing only 71% of the energy with a single mode inherently limits accuracy. On the other hand, the figures reveal that spanwise and chordwise Cp variations obtained with 5 modes closely align with the high-fidelity static aeroelastic analysis results. Furthermore, the R^2 metrics for 5 mode case reveal that the least accurate flow conditions

correspond to the first and the last parameter pair having the R^2 values of 0.9995. In terms of the NRMSE metric, the last flow condition is identified as the least accurate flow condition with a NRMSE of 0.0023. The results in Figure 3.12-Figure 3.14 also reflect the least accurate reconstructed flow conditions constructed with 5 modes. Therefore, it is safe to conclude that for the aeroelastic wing, employing 5 modes that capture 90% of the energy is sufficient to achieve accurate reconstruction results.

For the aeroelastic wing, deflection of the wing is obtained from the position of the nodes. Figure 3.15 shows the reconstructed displacement results using POD based ROM at M=0.85 and 5º AOA for the aeroelastic wing. Rigid wing is also included in this figure for a comparison purpose.

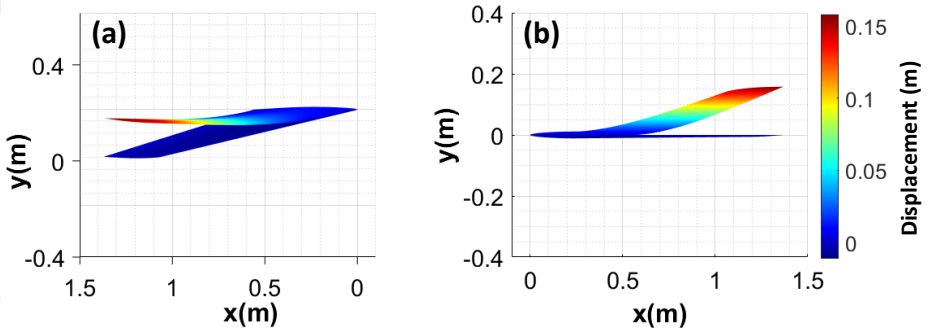

Figure 3.15. Isometric view (a) and side view (b) of the reconstructed displacement of the aeroelastic wing using POD based ROM (M=0.85 and AOA=5º)

The displacement of the wing can be inferred from the positions of the nodes. As shown in Figure 3.10, a single mode is sufficient to capture 99% of the energy associated with the node positions. Table 3.2 gives the maximum displacement derived from the reduced order solution utilizing 1 mode alongside those obtained from the high-fidelity static aeroelastic analysis. As expected, the maximum displacement calculated using a single mode closely matches with the high-fidelity result, demonstrating a high level of accuracy in the reduced-order model's solution.

Table 3.2. Comparison of the maximum displacements of the aeroelastic wing at M=0.85 & AOA=5º

High-fidelity static aeroelastic analysis result (m)	ROM displacement (m)
0.1580	**0.1584**

A comparison of the Cp data ensembles for the rigid and aeroelastic wings reveals that for the rigid wing 1 mode captures 57% of the energy, whereas for the aeroelastic wing 1 mode captures 71%. Moreover, to reach 90% of the energy, 8 modes are required for the rigid wing, whereas 5 modes are sufficient for the aeroelastic wing. This reduced requirement for the aeroelastic wing can be attributed to the more regular and consistent pattern in the Cp distribution. On the other hand, the rigid wing exhibits a disruption in this pattern as the AOA increases, necessitating additional modes to adequately capture the complexities of its aerodynamic behavior. The disruption of the Cp variation is shown in Figure 3.16 which compares the chordwise Cp distributions for the rigid and aeroelastic wings for M=0.85 across three different AOAs (1º, 3º, 5º). This figure highlights the differences in the aerodynamic behavior between the two configurations, demonstrating how the Cp distribution for the rigid wing becomes irregular with an increasing AOA, in contrast to the more stable distribution observed for the aeroelastic wing.

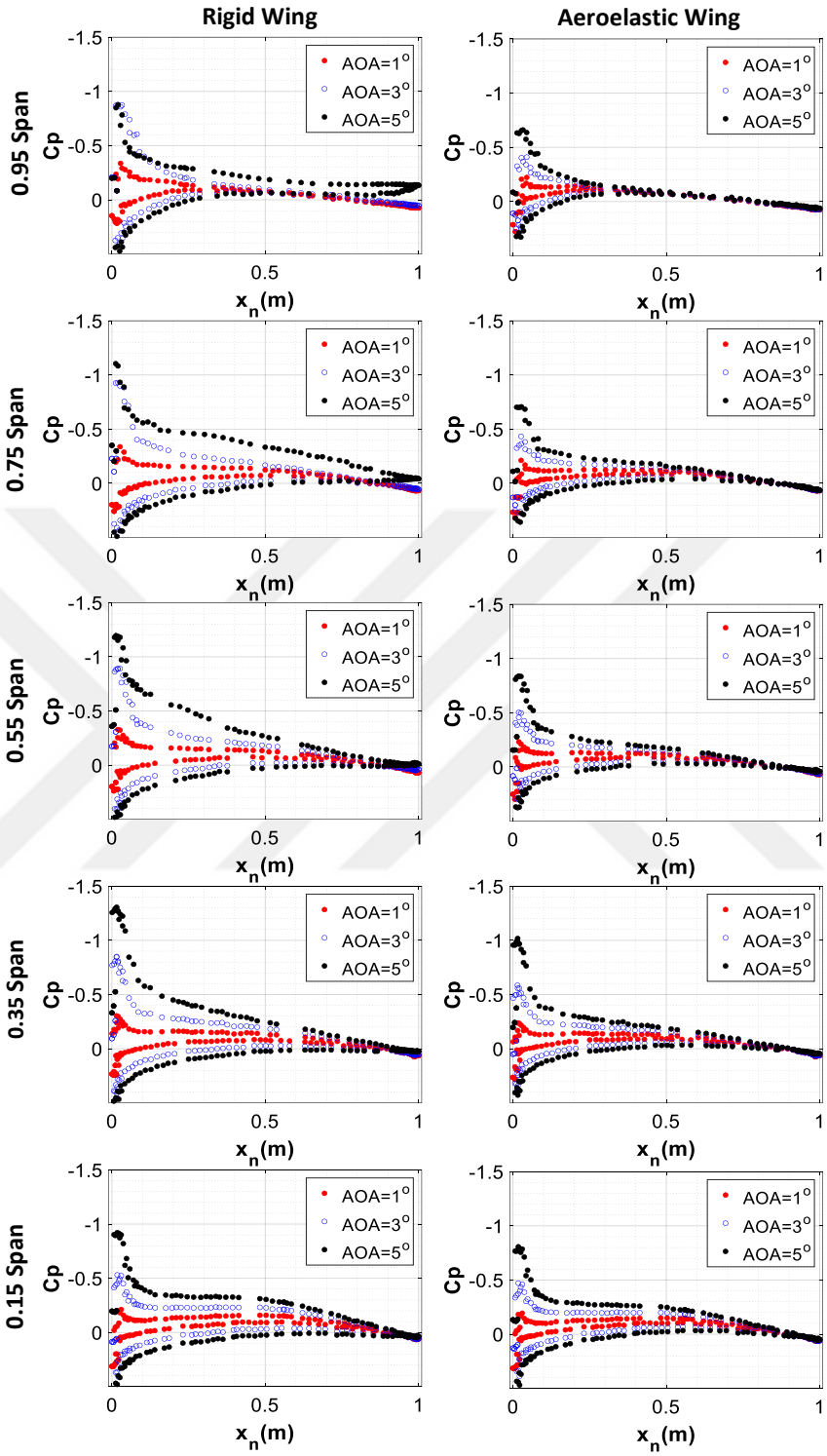

Figure 3.16. Cp vs normalized chord (x_n) of the rigid and the aeroelastic wing (M=0.85 for AOA = 1º, 3º, 5º)

The span locations are displayed in Figure 3.17. The nodes which are used for the comparison of the results for different cases are taken from sectional regions within a 0.004 m interval from the given chordwise section.

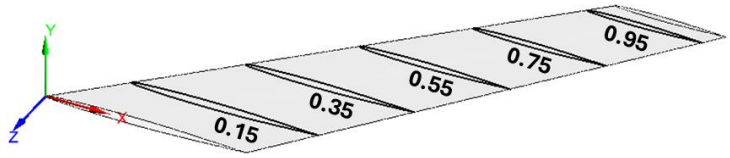

Figure 3.17. Span locations where sectional Cp distributions are compared

Figure 3.16 shows that for the rigid wing, at a higher AOA such as 5°, the Cp distribution ceases to follow a pattern like the aeroelastic wing. Figure 3.18 displays the streamlines around the rigid and aeroelastic wings for the 5° AOA case, evaluated at five different chordwise sections of the wing given in Figure 3.17.

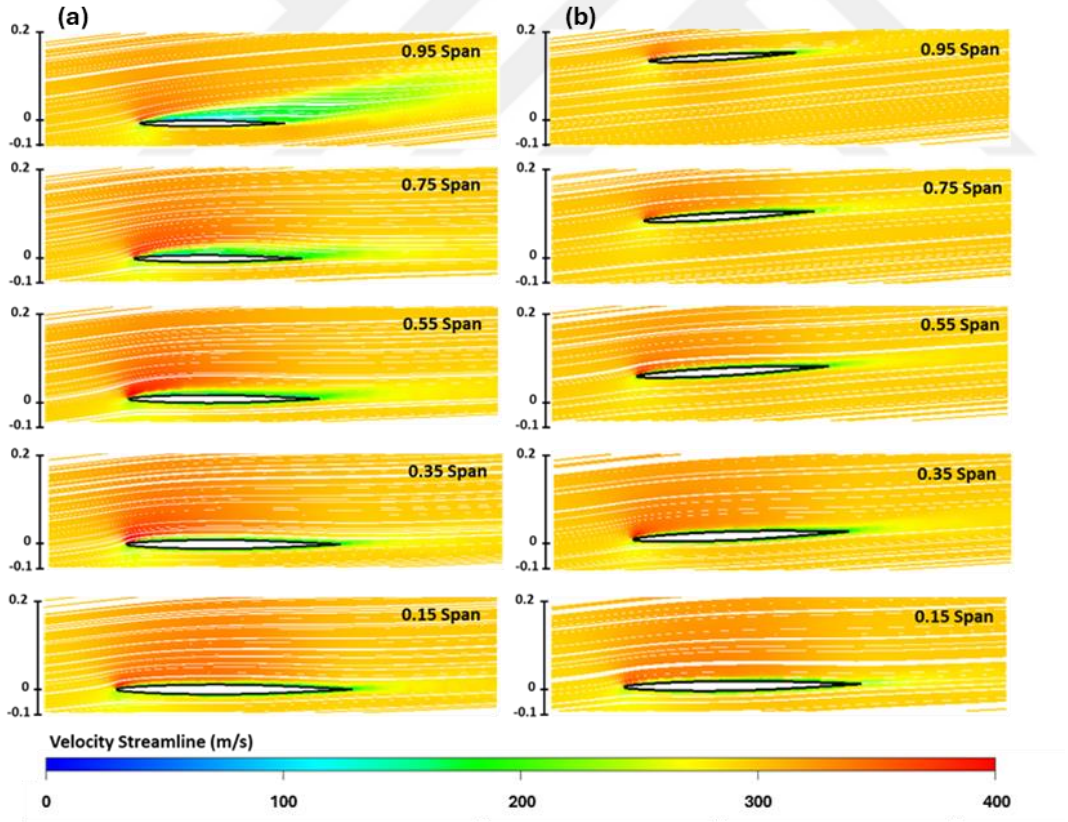

Figure 3.18. Streamlines around the rigid (a) and the aeroelastic wing (b) at different span locations (M=0.85 and AOA=5°)

As seen in Figure 3.18, for the rigid wing, the boundary layer tends to separate from the top surface at 5º AOA indicating flow separation while the flow remains attached to the surface of the aeroelastic sweptback wing. This separation progressively increases from wing root to the tip. It is worth noting that the wing under consideration features a relatively thin airfoil that tapers towards the tip, making it more susceptible to separation. The streamlines exhibit a pronounced upward deflection near the leading edge, indicating the onset of adverse pressure gradients. On the contrary, the streamlines for the aeroelastic sweptback wing remain relatively undisturbed, flowing smoothly along the airfoil without pronounced separation. This behavior can be attributed to the decrease in the effective AOA resulting from the inward twist of the aeroelastic sweptback wing due to bending. The decrease in the effective AOA across different sections of the aeroelastic wing (Figure 3.17) under the same flow condition (M=0.85 and AOA=5°) is shown in Figure 3.19 reinforcing the impact of structural flexibility on the aerodynamic performance and flow characteristics.

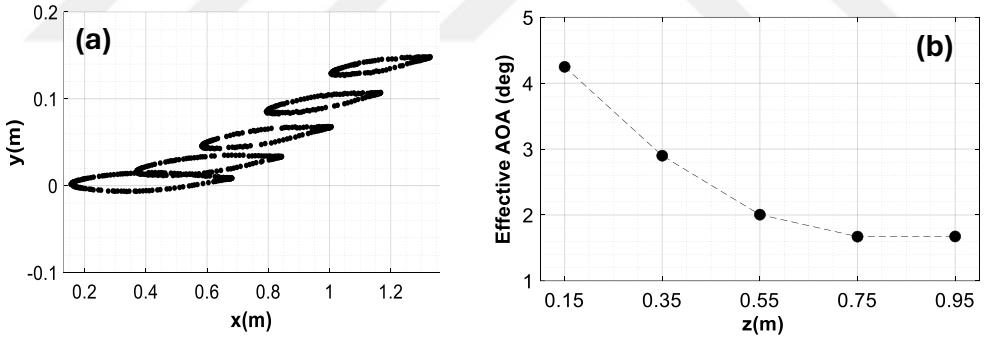

Figure 3.19. Twist of the aeroelastic wing at different sections (a) and decrease in the effective AOA at these sections (b)

As typical behavior of the wings with a sweptback geometry, when the aeroelastic wing bends, the effective AOA at a wing section decreases due to the bending-torsion coupling. The bending deformation induces twisting of the wing sections as shown in Figure 3.19.

The resulting twist leads to a reduction in the effective AOA across the wing, effectively ceasing flow separation. As illustrated in Figure 3.19, the outboard

sections of the aeroelastic sweptback wing experience a greater inward twist compared to the inboard sections. For the rigid AOA case of 5°, nearly half of the outboard wing sections exhibit an effective angle of attack of less than 2°. Due to the more consistent and regular pattern of the Cp distribution change observed in the aeroelastic sweptback wing, a reduced number of modes is sufficient to accurately capture the system's behavior. This characteristic facilitates a more efficient reduced-order modeling for the aeroelastic sweptback wing compared to the rigid wing.

For the aeroelastic wing, an additional reduced-order model is constructed to represent the von-Mises stress distribution, based on the results from 2-way static aeroelastic analysis. In this case, it is observed that 1 mode captures 96.5% of the energy (Figure 3.20).

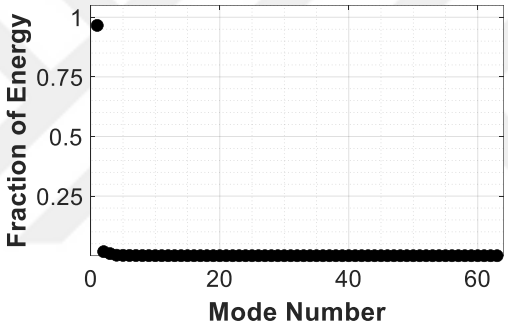

Figure 3.20. Fraction of energy for the von-Mises stress in the aeroelastic wing

Utilizing 1 mode only, NRMSE and R^2 error values obtained for each 63 variable pair are given in Figure 3.21 respectively.

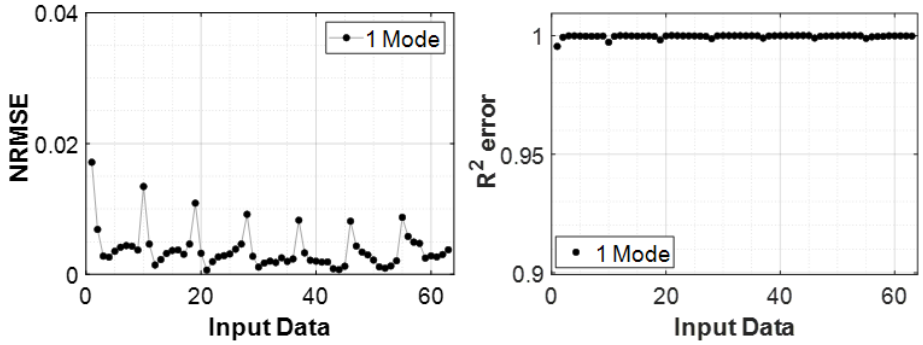

Figure 3.21. NRMSE and R^2 error for the von-Mises stress on the aeroelastic wing

Both error metrics indicate that the first variable pair yields the least accurate results with a NRMSE of 0.017 and R^2 value of 0.9954. Therefore, the von-Mises stress result of this case is investigated in detail. Figure 3.22 presents the von-Mises distribution on the surface of the wing for the first flow condition of M=0.55 and AOA=1º.

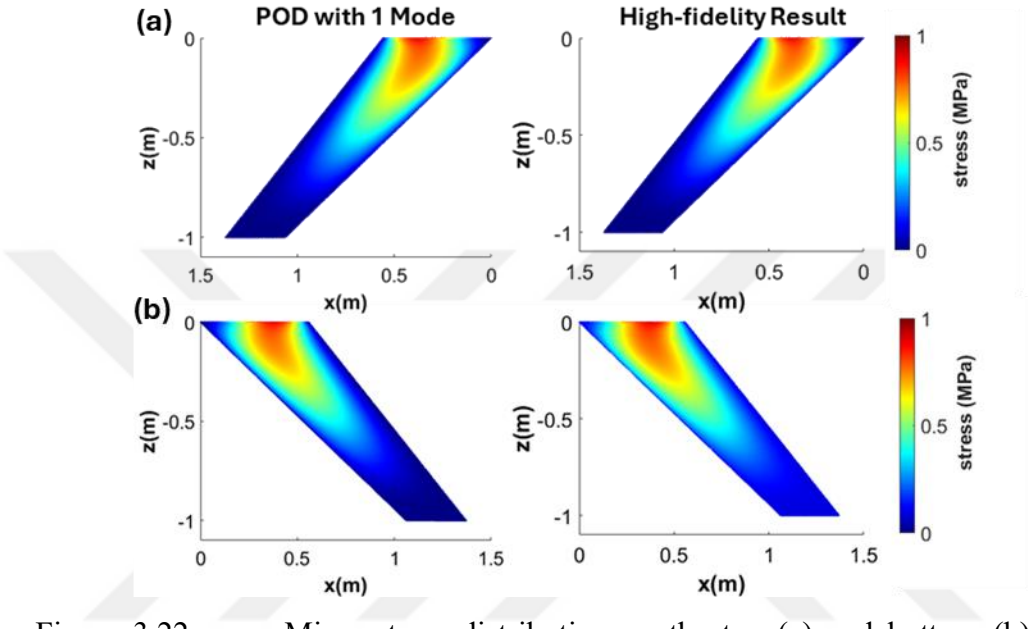

Figure 3.22. von-Mises stress distribution on the top (a) and bottom (b) wing surfaces obtained by the high-fidelity aeroelastic analysis and the reconstructed result with 1 mode (M=0.55 & AOA=1º)

Figure 3.22 demonstrates that the POD with a single mode yields almost the same von Mises distribution as the high-fidelity result for the least accurate flow condition. In addition, for this flow condition of M=0.55 and AOA=1º, maximum von-Mises is obtained as 1.0110 MPa, while the reconstructed maximum von-Mises stress via POD is 1.0179 MPa, which also shows the accuracy of the reduced order model.

3.2.3 Dataset Involving Higher Mach Numbers

In the dataset presented in Figure 3.1 no shock formation is observed on the wing. In this part of the study, the snapshot matrix, originally constructed from the data points shown in Figure 3.1, is extended to include cases with higher Mach numbers.

These additional cases result in the formation of shock waves, thereby introducing considerable nonlinearity into the problem. The POD method is then assessed using this extended dataset, with a focus on its effectiveness in reconstructing the flow field under these more complex conditions. In this case, it should be noted that for transonic flow conditions, where highly nonlinear flow behavior is present, the mesh configuration should be tailored to ensure greater accuracy. However, in this study, the snapshot matrix is generated using data from individual nodes, which necessitates maintaining a consistent number of nodes across different flow conditions. Consequently, the same mesh is used for higher Mach numbers as the observed discrepancies are within an acceptable range (the effect of increasing mesh density is discussed in Appendix C). However, in cases involving significant changes in flow conditions, developing separate ROMs can be necessary to improve the fidelity of the results.

To include higher Mach numbers into the dataset, the flow conditions at Mach 0.9 and 0.95 are added to the snapshot matrix, preserving the uniform interval. The extended dataset, consisting of 81 data points, is shown in Figure 3.23.

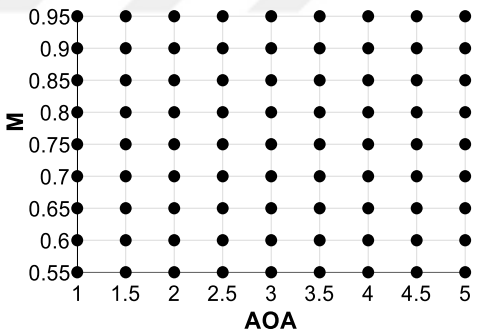

Figure 3.23. Extended dataset with 81 data points

At a Mach number of 0.95, a flow discontinuity is observed, introducing a noticeable nonlinearity to the problem. For this flow condition with 5º AOA, the Cp distribution on the wing surface and the variation in Mach number at different span locations are given in Figure 3.24.

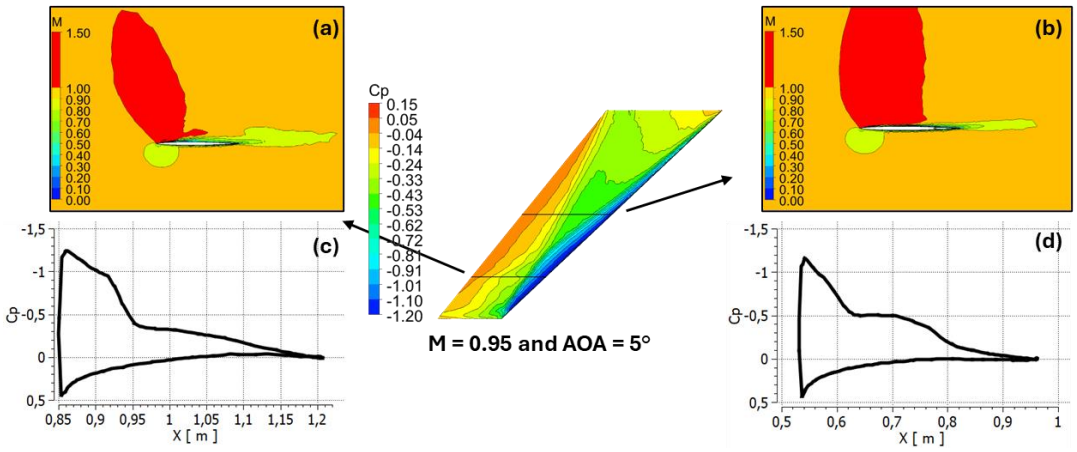

Figure 3.24. The Cp distribution on the wing; as well as the Mach variation at 0.8 m (a) and 0.5 m (b) span locations, chordwise Cp distributions at 0.8 m (c) and 0.5 m (d) span locations on the rigid wing for M=0.95 and AOA=5° flow condition

At the freestream Mach number of 0.95, the flow accelerates toward Mach 1 and exceeds it on the upper surface, then drops rapidly. This behavior indicates a presence of shock. This phenomenon is also accompanied by a sudden change in pressure, as seen in the chordwise Cp distributions shown in Figure 3.24 where the abrupt changes can be seen clearly. In Appendix D, an additional sample flow condition is provided at M=0.93 and AOA=4.5°, where shock formation is observed, as well as a reference case at M=0.85 and AOA=5°, where no shock is present.

A similar shock-related behavior is observed in the aeroelastic wing configuration under the same flow conditions. In this case, shocks primarily occur along the inboard wing section (close to wing root), as shown by the variations in Mach number and Cp distribution in Figure 3.25.

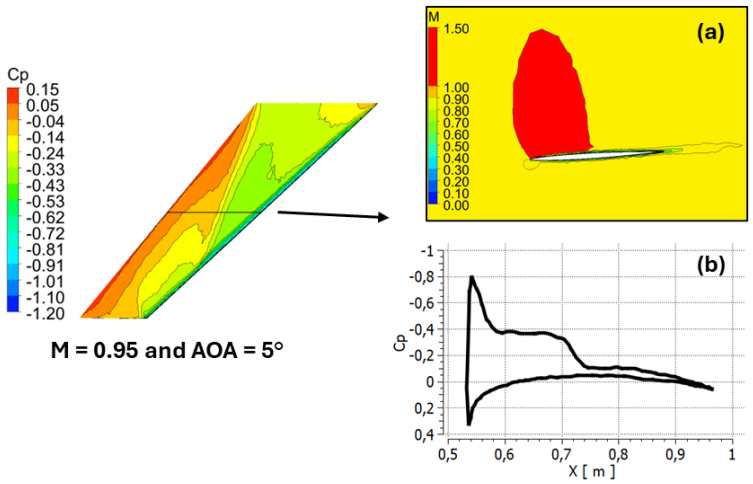

Figure 3.25. The Cp distribution on the wing, as well as the variation of M at the 0.5 span location (a) and the chordwise Cp distribution at the 0.5 span location of the aeroelastic wing (b)

For the extended snapshot matrix constructed for Cp results, which includes Mach numbers of 0.9 and 0.95, 14 POD modes are required to capture 90% of the energy for the rigid wing, while 8 POD modes are required for the aeroelastic wing. The accumulated energy for both configurations is shown in Figure 3.26.

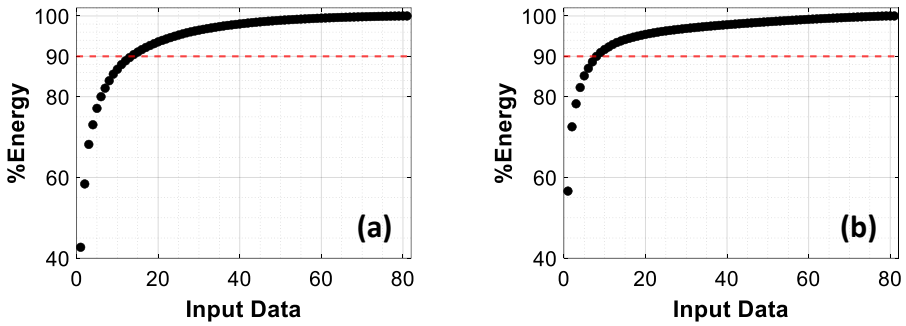

Figure 3.26. Accumulated energy for the Cp of the rigid wing (a) and the aeroelastic wing (b)

The Table 3.3 compares the number of POD modes required in the current case with those in the previous 63-sample case to capture at least 90% of the total energy.

Table 3.3. Comparison of the POD mode numbers for different cases

	63 Data Samples (M=0.55-0.85)	**81 Data Samples (M=0.55-0.95)**
Rigid Wing	8 modes	14 modes
Aeroelastic Wing	5 modes	8 modes

The results indicate that the number of POD modes required nearly doubles in the case with 81 data samples, compared to the case with 63 samples. This increase is primarily attributed to the presence of shock formations in the 81-sample dataset, which introduces significant distortions to the flow field. In contrast, the 63-sample case exhibits flow patterns with fewer discontinuities, resulting in a more efficient modal representation.

3.2.3.1 Rigid Wing Configuration

The Cp results are reconstructed using 14 modes for the rigid wing. The NRMSE and R^2 error distributions for each 81 flow cases are given in Figure 3.27.

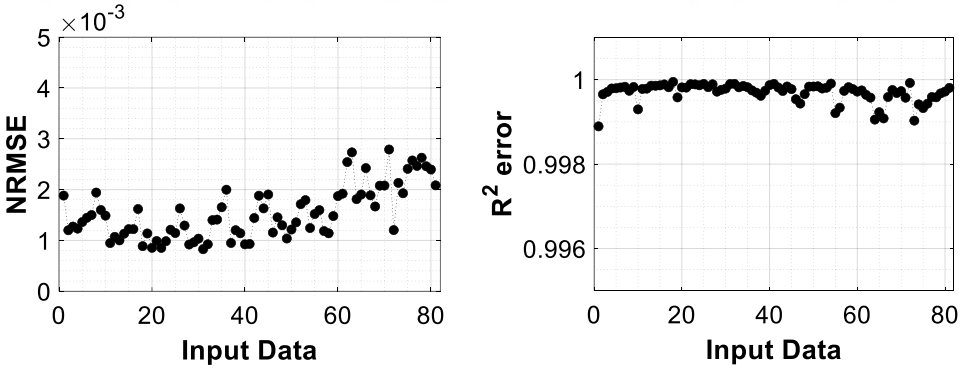

Figure 3.27 NRMSE and R^2 errors for the reconstructed Cp results using 14 modes for the rigid wing

Based on the NRMSE values, the least accurate result corresponds to the 71st flow condition, with a Mach number of 0.9 and AOA of 4.5°, and the R^2 errors indicate that 1st flow condition (M=0.55 and AOA=1º) is the least accurate. For these flow conditions, the chordwise Cp distribution is given in Figure 3.28 along with the last flow condition where shock is observed.

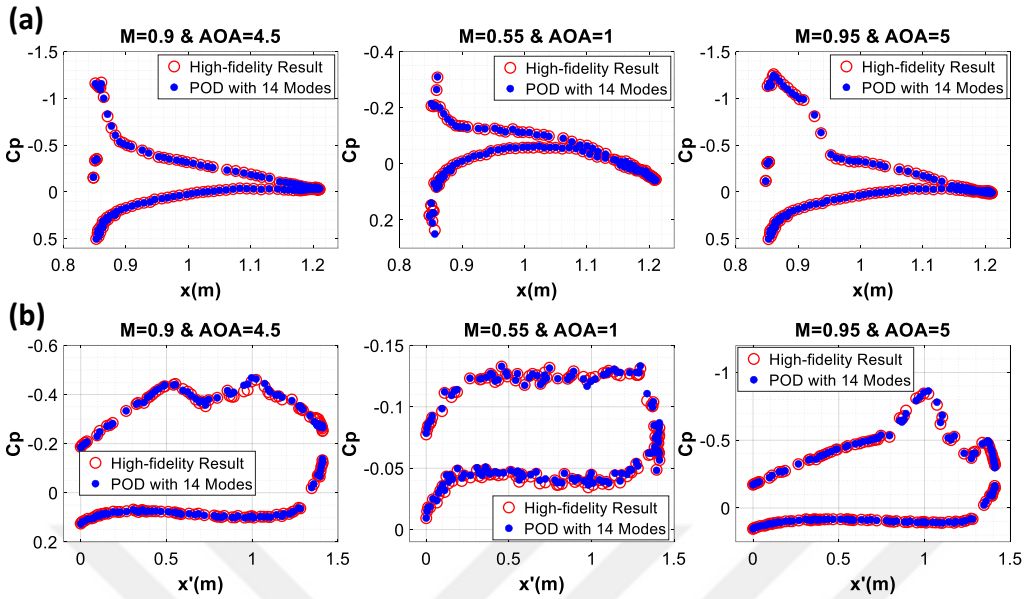

Figure 3.28 Chordwise (at 0.8 m of the span) (a) and spanwise (b) Cp distributions of the rigid wing for the 71st, 1st and 81st flow conditions reconstructed with 14 modes

The Cp distributions reconstructed with 14 POD modes are well matched with the full order model (FOM) results as can be seen in Figure 3.28.

3.2.3.2 Aeroelastic Wing Configuration

The Cp results for the aeroelastic wing are reconstructed using 8 modes. The NRMSE and R^2 error distributions for each 81 flow cases are given in Figure 3.29 for the aeroelastic wing.

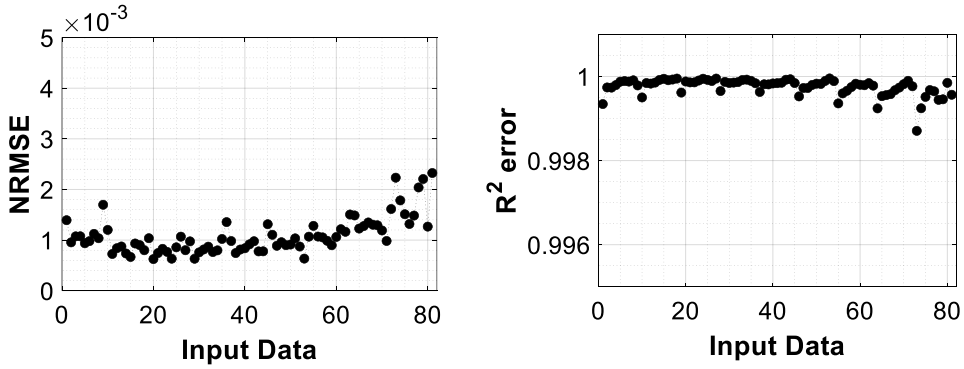

Figure 3.29 NRMSE and R^2 errors for reconstructed Cp results using 8 modes for the aeroelastic wing

The least accurate result corresponds to the 81st, the last flow condition of M=0.95 and AOA=5° based on the NRMSE results and the R^2 error results show that the least accurate one is the 73rd flow condition (M=0.95 and AOA=1º) when the results are reconstructed using 8 POD modes. For these flow conditions, the chordwise Cp distributions are shown in Figure 3.30 at 0.8m spanwise location as well as 0.5m where shock is observed for the last flow condition.

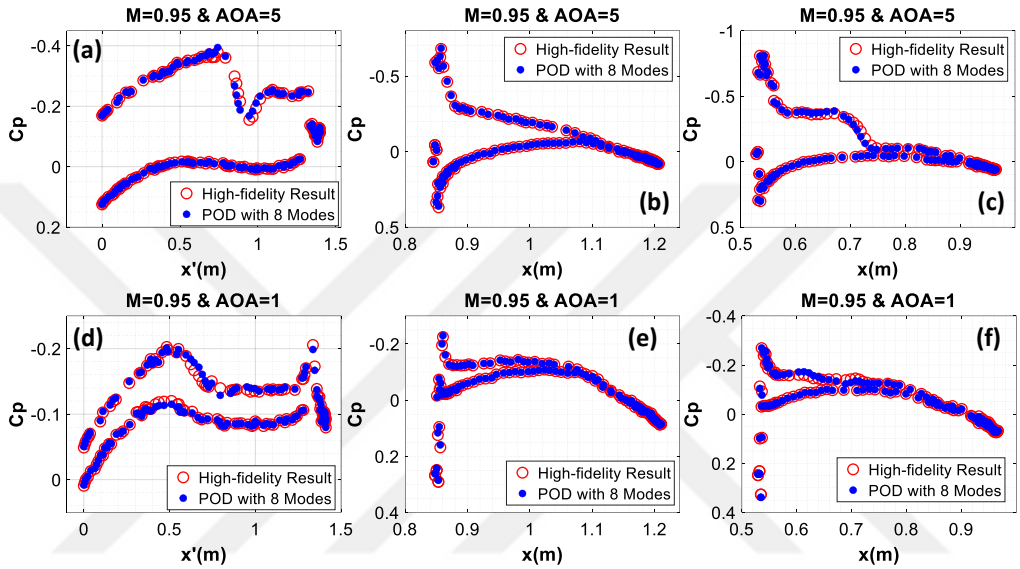

Figure 3.30 Spanwise (a) and chordwise (at 0.8 (b) and at 0.5 (c)) Cp distributions for the 81st and spanwise (d) and chordwise (at 0.8 (e) and at 0.5 (f)) Cp distributions for the 71st flow condition for the aeroelastic wing

Similar as before, for the aeroelastic wing case, a ROM is also constructed for x, y, z positions of the nodes using 1 mode. Without considering node positions, chordwise Cp distribution shows a mismatch with the high-fidelity results as shown in Figure 3.31.

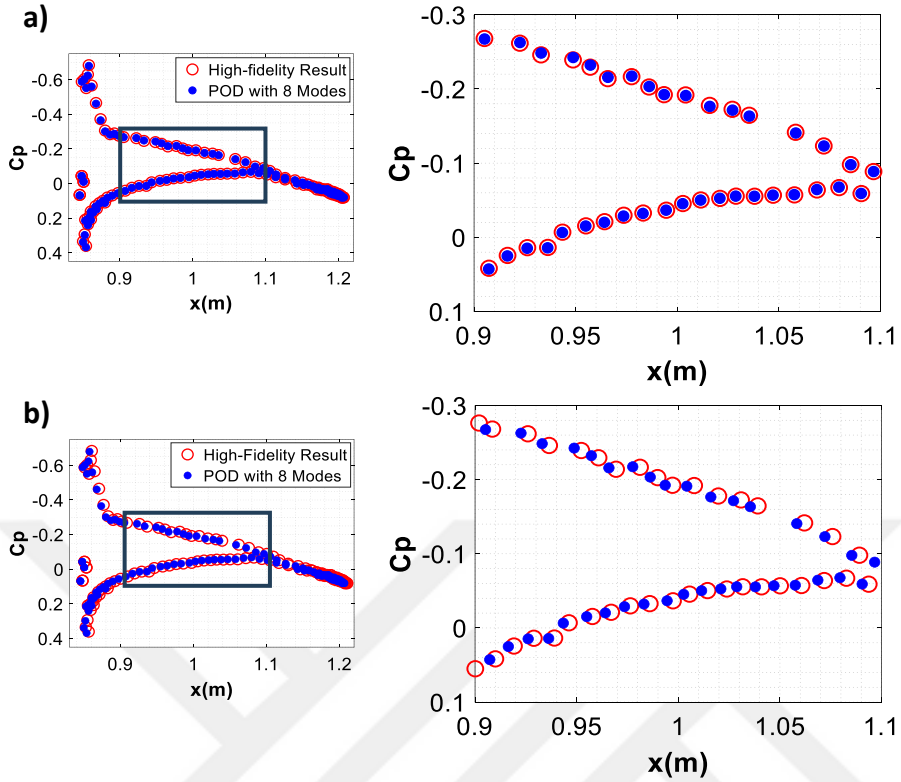

Figure 3.31 Chordwise Cp distributions at 0.8 m span of the aeroelastic wing with the reconstructed nodes using 1 mode (a) and the rigid nodes (b) (M=0.95 and AOA=5°)

As explained before, the maximum displacement can also be determined from the nodal positions. The reconstructed displacement, obtained from the ROM of the node positions, is presented in Figure 3.32.

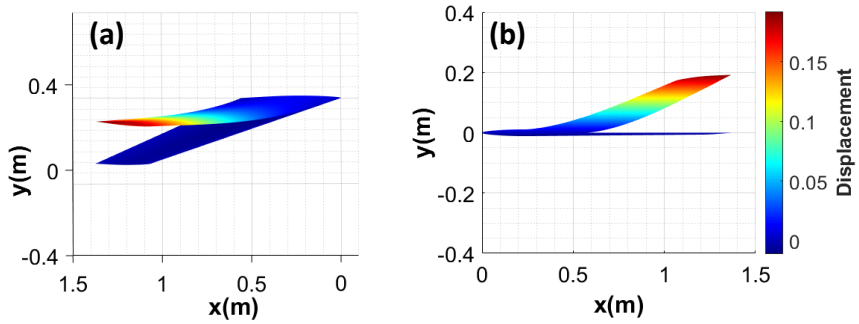

Figure 3.32 Isometric view (a) and side view (b) of the reconstructed displacement of the aeroelastic wing using POD based ROM (M=0.95 and AOA=5°)

The maximum displacement of POD reconstruction is found to be 0.1920 m while the high-fidelity result is 0.1912 m.

The results indicate that the POD method is more effectively applied to the dataset with 63 samples, which exhibits moderate nonlinearity. This is particularly evident in the aeroelastic wing configuration, where only 5 out of 63 modes are sufficient to accurately reconstruct all flow cases in the original dataset. However, the introduction of shock formations in the 81-sample dataset nearly doubles the number of required POD modes compared to the 63-sample case.

CHAPTER 4

REDUCED ORDER MODELING WITH POD-RBF METHOD AND SURROGATE MODELING WITH RADIAL BASIS FUNCTIONS

Having verified the accuracy of the reduced-order model constructed through the POD method for data reconstruction, this model is now employed to predict the results at intermediate variable values that do not exist in the original data ensemble. To achieve this, the POD-based reduced-order model must be coupled with an interpolation method. As discussed in the literature review in the introduction part, several techniques can be used for this purpose and among them the RBF method is one of the most favored option and stands out by its ease of implementation with high accuracy when applied to scattered multi-dimensional datasets; therefore, the RBF method has been adopted in this study for its capability to effectively handle the complexities of the data involved. Furthermore, the RBF method can be effectively employed to construct a surrogate model independently of the POD, by directly applying it to the snapshot matrix. In the last part of this chapter, the application of the RBF method for surrogate model construction is demonstrated, with a focus on its accuracy and efficiency.

4.1 Radial Basis Function (RBF) Method

The RBF model is a linear combination of basis functions evaluated at the Euclidean distance between the point x, at which the interpolation is made, and all the other points in the known data set. RBF model does not require regular data for accurate approximation, in particular, it is suitable for scattered data. RBF approximation of a function is built as,

$$f(x)_k = \sum_{i=1}^{m} \beta_i \phi(\|x - x_i\|) \qquad k = 1, \dots n \tag{11}$$

where, m is the number of data points, x_i's are the values at data points, ϕ is the chosen RBF and ||.|| is used to denote the Euclidean norm. In the current study, multiquadric basis function given in Equation (12) is used as the RBF.

$$\phi = \sqrt{1 + (c\,\|x\|)^2} \tag{12}$$

where the constant $c > 0$ is called the shape parameter. In Equation (11), β_i's are unknown coefficients to be found by making use of the existing data. Denoting the training data vector as f, the coefficient vector as β, and the interpolation matrix as ϕ, one can express the relation between them as,

$$\mathbf{f} = \boldsymbol{\phi}\boldsymbol{\beta} \tag{13}$$

where,

$$\mathbf{f}_k = \begin{Bmatrix} f_1 \\ f_2 \\ \vdots \\ f_m \end{Bmatrix} \boldsymbol{\beta}_k = \begin{Bmatrix} \beta_1 \\ \beta_2 \\ \vdots \\ \beta_m \end{Bmatrix} \boldsymbol{\phi}_k = \begin{bmatrix} \phi_{11} & \phi_{12} & \cdots & \phi_{1m} \\ \phi_{21} & \ddots & \ddots & \phi_{2m} \\ \vdots & \ddots & \ddots & \vdots \\ \phi_{m1} & \cdots & \cdots & \phi_{mm} \end{bmatrix}, k = 1, \ldots n$$

and $\boldsymbol{\phi}_{ij} = \boldsymbol{\phi}(\|\mathbf{x}_i - \mathbf{x}_j\|)$. Once the equation is solved for undetermined coefficients $\boldsymbol{\beta}$, approximation function f(x) can be evaluated for any data points that are not in the original data set.

Coupled with the POD method, RBF interpolation can be used to predict the solutions at intermediate parameters that are not sampled in the original snapshot matrix. However, it is also possible to perform RBF interpolation directly on the snapshot matrix for the same purpose. When data reduction is not the main concern, this approach could also be adopted. In this study, the two approaches are compared in terms of accuracy and computational cost.

4.2 Reduced Order Modeling with the POD coupled with the RBF

In this section, the POD-based reduced order models are coupled with the RBF method to predict the results for intermediate variables that do not exist in the original data set, consisting of the parameters presented in Figure 3.1. For this

purpose, Latin hypercube sampling (LHS) [58] is adopted to identify ten distinct flow conditions in the selected interval. The LHS is a statistical method that partitions the parameter domain into 'n' intervals forming n^m subintervals where m is the number of parameters, ensuring that each subinterval is represented by a single sample. This partitioning technique enhances the sampling process by providing a better uniformity compared to random sampling even if the samples are selected randomly. In Figure 4.1, parameter pairs obtained from the LHS that are used for the assessment of the POD-RBF model are shown. Parameter pairs shown as black dots are the data samples from the snapshot matrix, whereas the 10 parameter pairs derived from the LHS are shown as red dots. Moreover, an intermediate flow condition at high M and AOA (M=0.83 and AOA=4.75°) is also added to make the effect of deflection of the aeroelastic wing more visible. This data point is shown as the green dot in Figure 4.1.

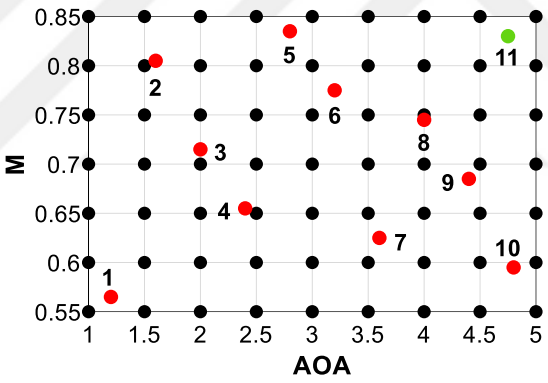

Figure 4.1. Samples from the LHS

4.2.1 Prediction of the Results for the Three-dimensional Rigid Wing Configuration

In Chapter 3, it is found that 8 modes out of 63 are required for the rigid wing to capture 90% of the energy to provide sufficient accuracy in flow reconstruction. In this section, the POD coefficients corresponding to these 8 POD modes are interpolated using the RBF method to obtain the POD coefficients for the flow cases

given in Figure 4.1. The NRMSE of Cp distribution for each 11 flow case is given in Figure 4.2.

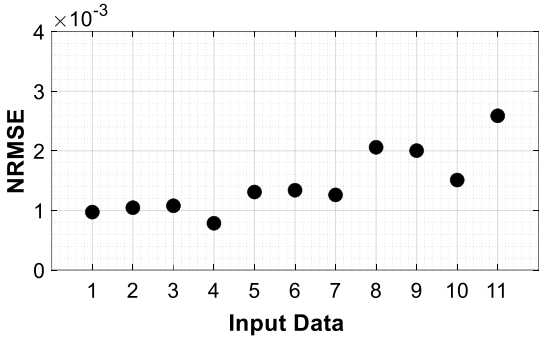

Figure 4.2. NRMSE of the Cp results for the rigid wing

The results of the NRMSE for ten randomly selected data points, along with an additional manually included 11th data point, indicate that notable accuracy is obtained for the rigid Cp distribution, with NRMSE values less than 4×10^{-3}. To further investigate the prediction performance, particular attention is given to the flow condition characterized by a Mach number of 0.83 and an AOA of 4.75°, which represents the highest Mach number and AOA pair within the intermediate dataset. This flow case exhibits the least accuracy in comparison to the other randomly selected points, requiring a more detailed investigation. For this reason, the resultant Cp distributions obtained by the high-fidelity CFD analysis and the coupled POD–RBF method for M=0.83 and AOA=4.75° are displayed on the 3D rigid wing in Figure 4.3.

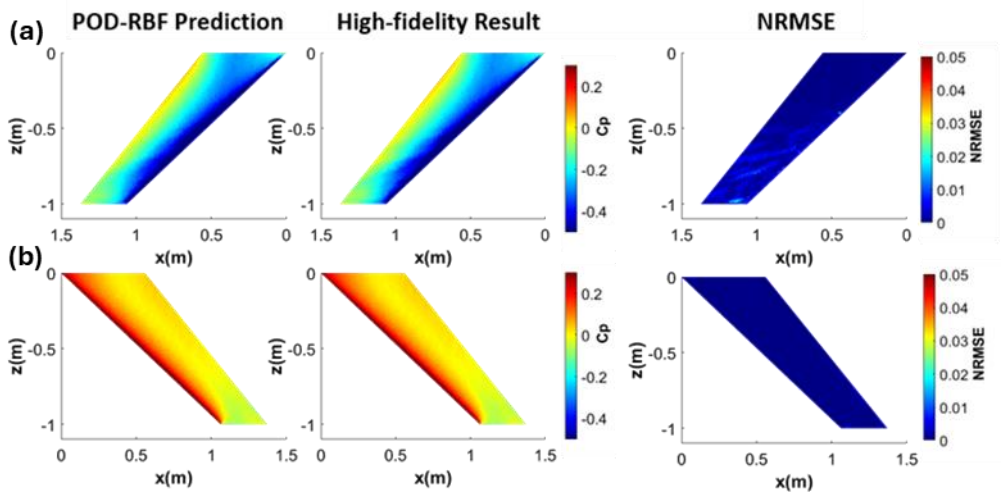

Figure 4.3 Cp distribution on the top (a) and the bottom (b) surfaces of the rigid wing obtained by high-fidelity CFD analysis and the predicted Cp via POD-RBF interpolation (M=0.83 and AOA=4.75°)

Figure 4.3 shows that predicted pressure distributions align closely with the high-fidelity CFD results. The NRMSE plots indicate that the NRMSE is higher on the top surface of the rigid wing in comparison to the bottom surface, which can be attributed to the greater distortion of the flow over the top surface compared to the bottom surface as discussed in Chapter 3. To observe the differences more clearly, sectional results at 0.95, 0.55 and 0.15 span locations are given in Figure 4.4.

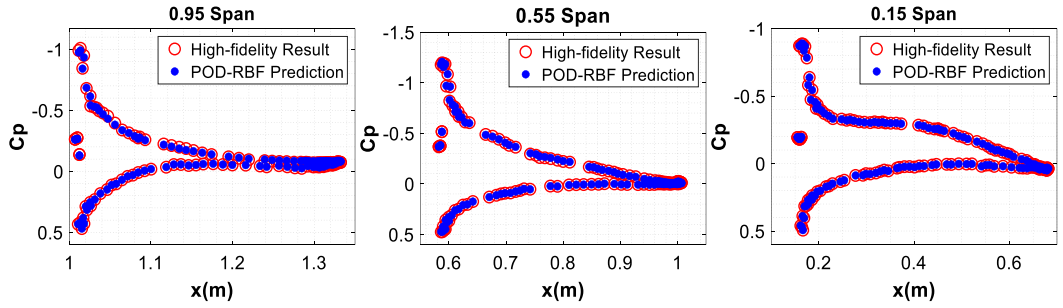

Figure 4.4 Variation of the Cp for different chordwise sections of the rigid wing obtained by high-fidelity CFD analysis and the predicted Cp via the POD-RBF interpolation (M=0.83 and AOA=4.75°)

The Cp distribution at a spanwise section taken through the aerodynamic center displayed in Figure 3.2 is also shown in Figure 4.5.

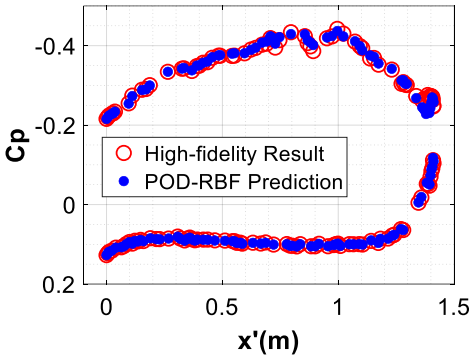

Figure 4.5 Variation of the Cp at the spanwise section of the rigid wing obtained by high-fidelity CFD analysis and the predicted Cp via the POD-RBF interpolation (M=0.83 and AOA=4.75°)

Figure 4.4 and Figure 4.5 reveal that the sectional Cp variations predicted by the POD-RBF method match well with the full order result. For the rigid wing, the R^2, RMSE and NRMSE for the POD-RBF prediction of the Cp at the flow condition M=0.83 and M=4.75° are calculated to be 0.9996, 0.0058 and 0.0026, respectively. These metrics show the great accuracy of the POD-RBF method in predicting Cp for the rigid wing. Furthermore, the lift coefficient (C_L) of the wing is computed numerically by approximating the Cp at each element as the average of the values at its nodes. In this case, the C_L obtained from the full order model (FOM) is 0.3236, while the POD-RBF yields a C_L of 0.3234, which also shows a close agreement between the FOM and ROM prediction.

4.2.2 Prediction of the Results for the Three-dimensional Aeroelastic Wing Configuration

For the aeroelastic wing configuration, it is seen in Chapter 3 that only 5 out of 63 modes are required to capture 90% of the energy associated with the aeroelastic Cp distribution, leading to the construction of a reduced-order model based on these 5 modes. In this case, POD coefficients corresponding to these POD modes are interpolated via the RBF method to derive the POD coefficients for the flow conditions presented in Figure 4.1. For these flow conditions the NRMSE of the

aeroelastic Cp distribution is given in Figure 4.6 along with the NRMSE for rigid wing, allowing for comparison.

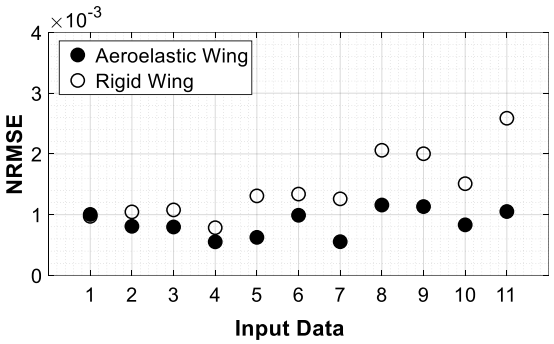

Figure 4.6. NRMSE of the Cp results for aeroelastic and rigid wings

Similar to the rigid wing case, great accuracy is achieved for the Cp distribution with all NRMSE values remaining below 2×10^{-3}. As inferred from the reconstruction study presented in Chapter 3, Figure 4.6 shows that the accuracy of the predictions for the aeroelastic wing, utilizing the POD-ROM with 5 modes, surpasses that of the rigid wing, which employs 8 modes. This observation highlights the effectiveness of the reduced-order modeling approach in capturing the aerodynamic characteristics of the aeroelastic wing with greater fidelity.

Similar to the analysis conducted for the rigid wing, the flow condition of M=0.83 and M=0.75°, which corresponds to the highest wing deflection is investigated in more detail. The Cp distribution for this flow condition is presented in Figure 4.7.

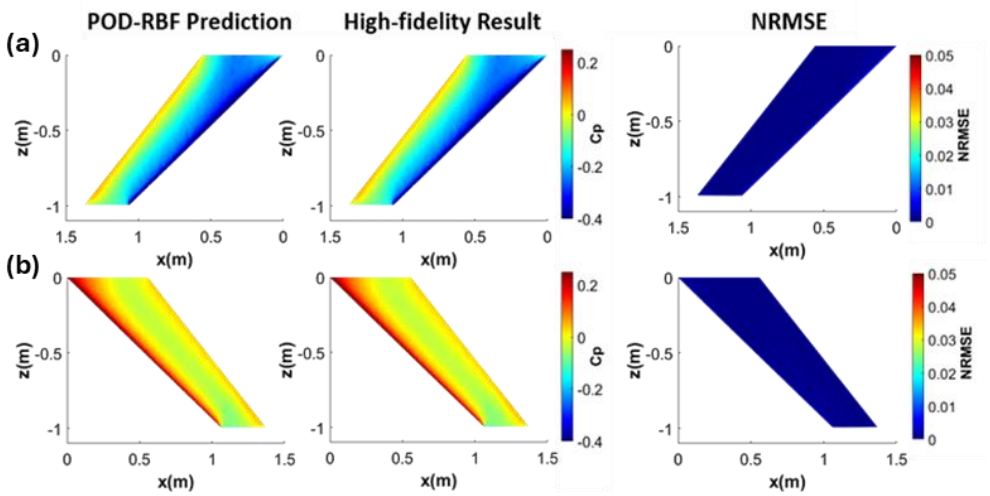

Figure 4.7. Cp distribution on the top (a) and the bottom (b) surfaces of the wing obtained by high-fidelity static aeroelastic analysis and the predicted Cp via the POD-RBF interpolation (M=0.83 and AOA=4.75°)

Figure 4.7 shows that predicted Cp distributions align perfectly with those obtained from high-fidelity static aeroelastic analysis. For the aeroelastic wing, the R^2, RMSE and NRMSE for the POD-RBF prediction of the Cp at the flow condition M=0.83 and M=4.75° are calculated as 0.9999, 0.0024 and 0.0011, respectively. Furthermore, the NRMSE values on the top and bottom surfaces of the aeroelastic wing are notably closer to each other compared to those obtained in the rigid wing case. As displayed in Figure 3.17, this phenomenon arises from the bending–twisting coupling effect of the sweptback wing geometry, which results in a reduced distortion of pressure distributions on the top and bottom surfaces of the aeroelastic wing relative to the rigid wing. In this case, the C_L from the FOM is 0.1990, while the POD-RBF prediction yields 0.1992, demonstrating close agreement between the full-order and reduced-order models.

For the aeroelastic wing configuration, accurate construction of Cp plots requires consideration of the position change of the nodes due to the wing deflection. It can be recalled from Chapter 3 that for the position of the nodes, a single mode is sufficient to construct a highly accurate reduced order model. Hence, by interpolating the POD coefficients corresponding to a single mode, the required POD coefficients for the M=0.83 and AOA=4.75° flow case are obtained. In Figure 4.8

and Figure 4.9 Cp variations are displayed along the chordwise and spanwise sections of the aeroelastic wing by utilizing the ROMs constructed for both Cp values and the coordinates of the nodes. Additionally, these figures display the Cp distribution using constant node positions, as in the case of rigid wing case, in order to enable a comparison and evaluate the effect of wing deflection on the representation of the Cp distribution.

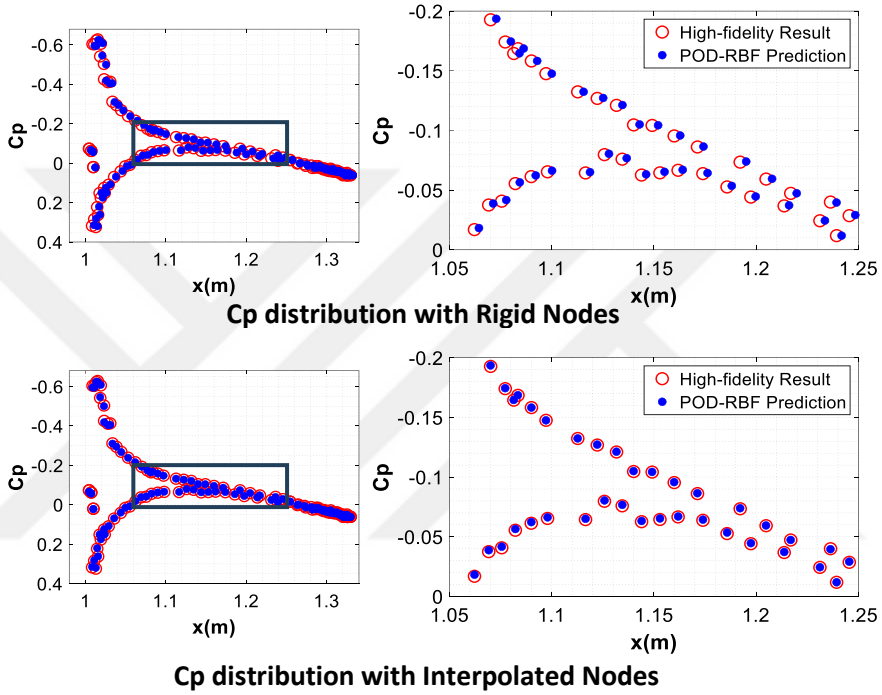

Figure 4.8. Chordwise (at the 0.95 m span location) Cp variation of high-fidelity static aeroelastic analysis and the predicted Cp of the POD-RBF interpolation (M=0.83 and AOA=4.75°)

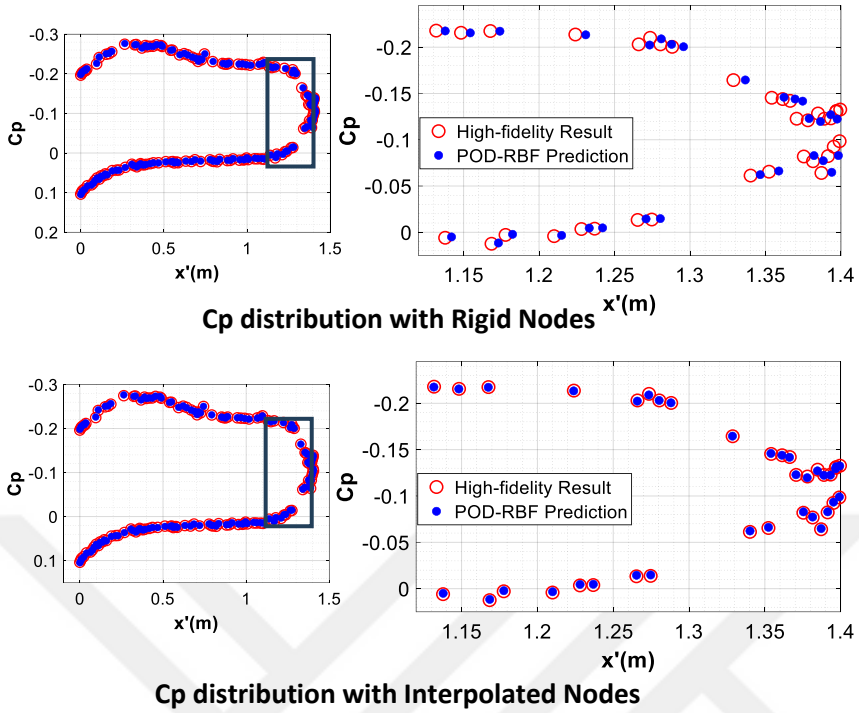

Figure 4.9. Spanwise Cp variation of high-fidelity static aeroelastic analysis and the predicted Cp of the POD-RBF interpolation (M=0.83 and AOA=4.75°)

Zoomed views in Figure 4.8 and Figure 4.9 clearly demonstrate that the predicted Cp distribution via the POD-RBF interpolation exhibits a notable improvement when the positions of the nodes are also taken into account by constructing a separate POD model and coupling it with the RBF method for interpolation. It is important to note that for more flexible wings, the discrepancies in Cp distribution obtained by utilizing rigid nodes and interpolated nodes will be more pronounced; hence, a dedicated ROM for the positions of the nodes is essential for accurately capturing the behavior of flexible wings. Moreover, as a by-product of utilizing a separate POD-RBF coupled ROM for node positions facilitates the calculation of the aeroelastic wing's displacement. For the M=0.83 and AOA=4.75° flow condition, while the maximum displacement is calculated as 0.1454 m by the full order analysis, utilizing the coupled POD-RBF ROM method maximum wing deflection is predicted very accurately as 0.147 m. This close alignment shows the effectiveness of the proposed approach in capturing both Cp distributions and wing displacements.

Moreover, for the aeroelastic wing, an additional reduced order model was constructed specifically for the von Mises stress distribution, utilizing the results obtained from the two-way static aeroelastic analysis. As indicated in Chapter 3, it was found that a single mode captures 96.5% of the energy associated with the Cp distribution. Utilizing this reduced order model, the von Mises stress distribution at M=0.83 and AOA=4.75° is calculated. The predicted von Mises stress distributions via the coupled POD-RBF method and von Mises stress distributions calculated by high-fidelity static aeroelastic analysis on the top and bottom wing surfaces are shown in Figure 4.10.

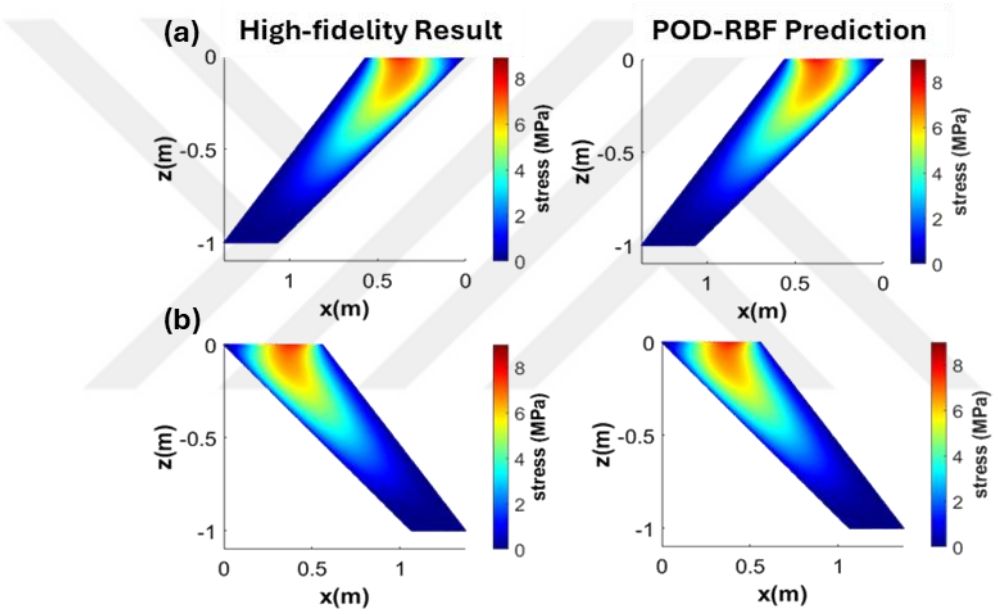

Figure 4.10. von Mises Stress distribution on the top (a) and bottom (b) wing surfaces (M=0.83 and AOA=4.75°)

Figure 4.10 shows the well-matched results of the high-fidelity analysis and the POD-RBF predicted von Mises stress distributions with R^2, RMSE and NRMSE of 0.9997, 0.0384 and 0.0043, respectively. Moreover, the maximum von Mises stresses obtained by the full order aeroelastic analysis is 8.88 MPa, whereas from the coupled POD-RBF approach it is found to be 8.94 MPa. This analysis demonstrates the effectiveness of the POD-RBF approach in accurately capturing the stress distribution within the aeroelastic wing structure.

4.2.3 Prediction of the Results for a Dataset Involving Higher Mach Numbers

In this section, the POD-RBF approach is evaluated for its predictive capability in terms of Cp distribution under higher Mach number cases. To support this analysis, 4 additional data points, located between Mach numbers 0.85 and 0.95, are introduced, in addition to the previously selected 11 data points (in Figure 4.1), indicated by red markers in Figure 4.11.

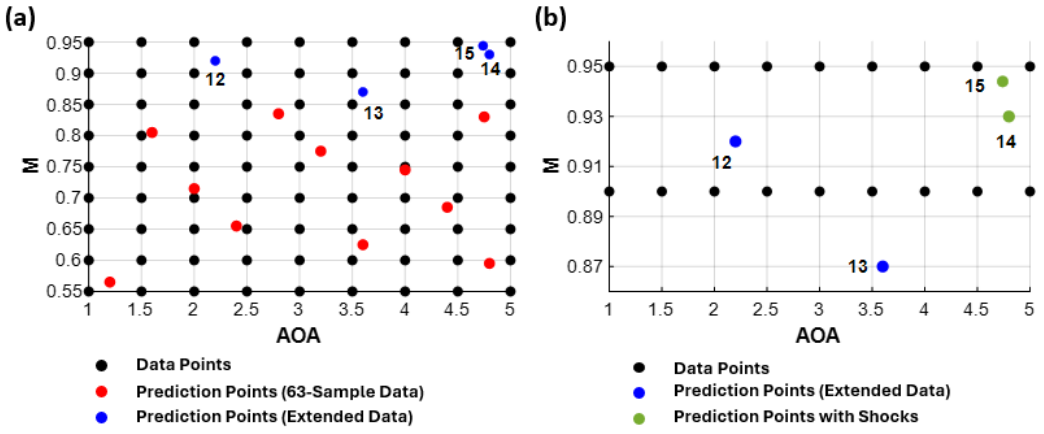

Figure 4.11 Intermediate points to be predicted (a) and the new prediction points (b)

In Figure 4.11 (b), the prediction points where shock formation is observed are indicated with green markers, corresponding to the last two flow conditions, labeled as 14 and 15. The NRMSE results for the Cp predictions of the rigid wing for these 15 sample points are given in Figure 4.12 for both previous 63-data sample case and current 81-sample case.

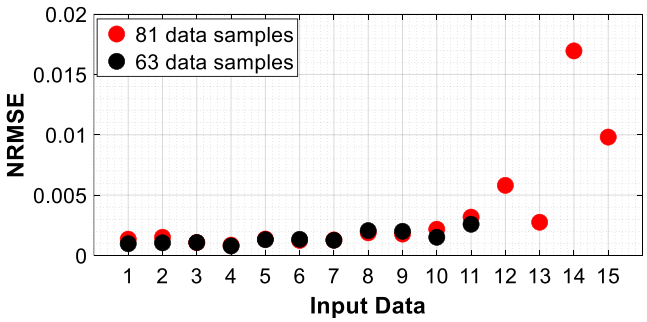

Figure 4.12 NRMSE of the Cp results for the rigid wing using 63-sample and 81-sample cases

Figure 4.12 clearly shows that, as the Mach number exceeds 0.9, the prediction accuracy tends to decrease for the case with 81 data samples. In particular, the highest NRMSE values correspond to the last two prediction points, where shock formation is observed. The sectional Cp predictions obtained using the POD-RBF method for the 14th flow condition, least accurate case, are given in Figure 4.13.

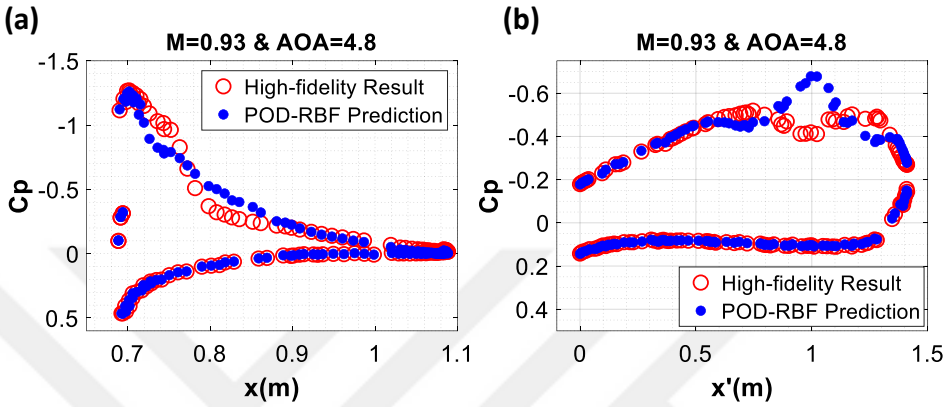

Figure 4.13 Chordwise (at 0.65 m span) (a) and spanwise (b) Cp distributions of the rigid wing predicted using POD-RBF with 81 data samples (M=0.93 and AOA=4.8°)

Figure 4.13 shows a notable discrepancy between the actual results and those predicted by the POD-RBF method. In addition, the predicted Cp distribution on the upper surface of the 3D wing, obtained using the POD-RBF model, are compared with the FOM results in Figure 4.14.

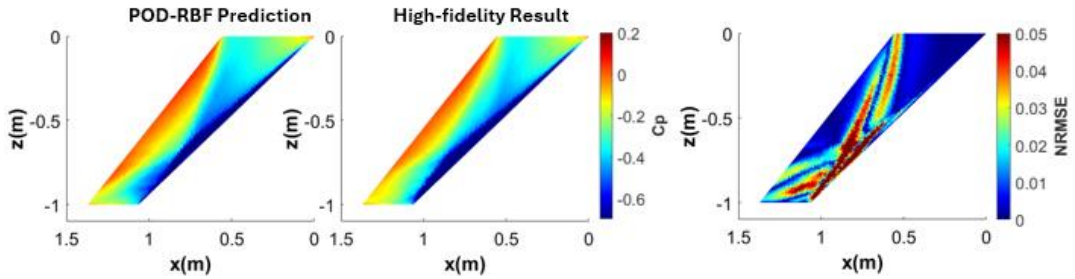

Figure 4.14 Cp distribution on the upper surface of the rigid wing for the 14th flow condition (M=0.93 and AOA=4.8°)

Figure 4.14 also reveals a noticeable difference between the predicted and FOM results, particularly at the outboard section of the wing where flow distortion is more pronounced. In this case, the C_L obtained from the FOM is 0.3827, while the POD-

RBF yields 0.3813. Despite notable differences in Cp at certain locations, the overall C_L difference is approximately 0.4%.

A comparison of the NRMSE distribution for the Cp results of both rigid and aeroelastic wings are given in Figure 4.15.

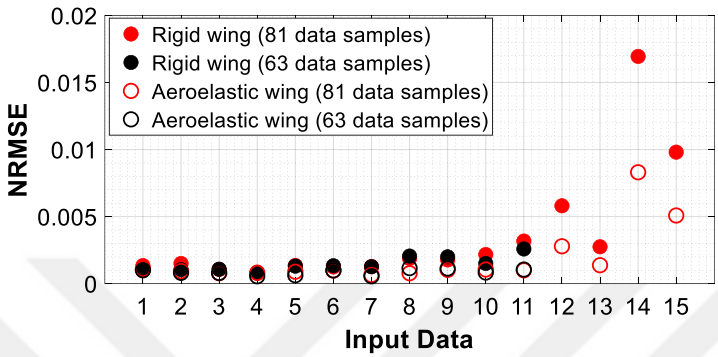

Figure 4.15 NRMSE of the Cp results for the rigid and aeroelastic wings obtained using POD-RBF approach

Consistent with the results from the 63-sample case, the aeroelastic wing exhibits higher prediction accuracy than the rigid wing across all prediction points. However, similar to the rigid wing case, the prediction accuracy decreases for flow conditions with Mach numbers greater than 0.9. The least accurate flow condition corresponds to the 14th prediction point, with M=0.93 and AOA=4.8°, as in the rigid wing. For this case, the predicted sectional Cp distributions are shown in Figure 4.16.

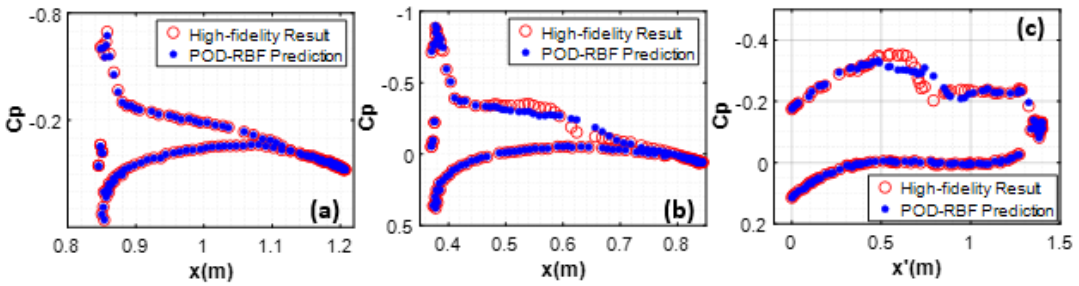

Figure 4.16 Chordwise (at 0.8m (a) and 0.35m (b) span) and spanwise (c) Cp distributions of the aeroelastic wing for the 14th prediction point

As can be seen in Figure 4.16, although the results exhibit a better agreement than those for the rigid wing case (Figure 4.13), noticeable discrepancies are still evident. A good match is observed along chordwise sections where no shock occurs;

however, mismatches appear in regions affected by shock formation. In this case, the C_L from the FOM is 0.2059, while the POD-RBF yields 0.2042. Despite local discrepancies in Cp, the overall C_L difference of approximately 0.8% can be acceptable for many applications. The Cp distribution on the upper surface of the 3D wing is also presented in Figure 4.17, clearly illustrating the reduction in prediction accuracy within the shock region.

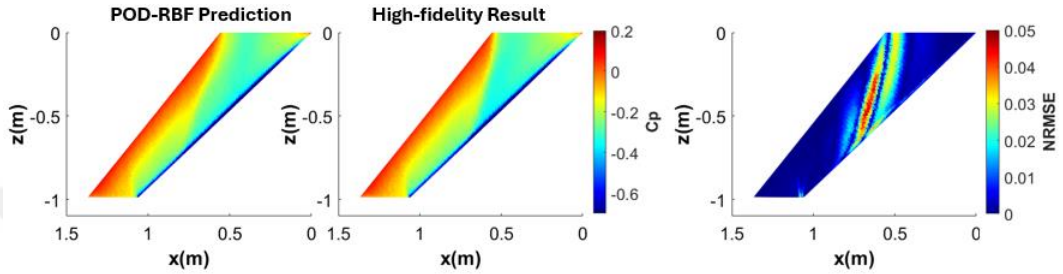

Figure 4.17 Cp distribution on the upper surface of the aeroelastic wing for the 14th flow condition (M=0.93 and AOA=4.8°)

As can also be seen in Figure 4.17, the results show better agreement at the outboard wing sections as opposed to the rigid wing case. However, at the inboard sections where shock formation occurs, the prediction accuracy decreases. To improve prediction accuracy for both rigid and aeroelastic wing configurations under flow conditions where shock formation occurs, the data density is increased between Mach 0.9 and 0.95.

Extended Dataset with 90 Data Samples

To be able to increase the prediction accuracy between the M=0.9 and 0.95, the results of M=0.93 flow condition are also added to the snapshot matrix given in Figure 3.1. The extended dataset is illustrated in Figure 4.18 consisting of 90 data points.

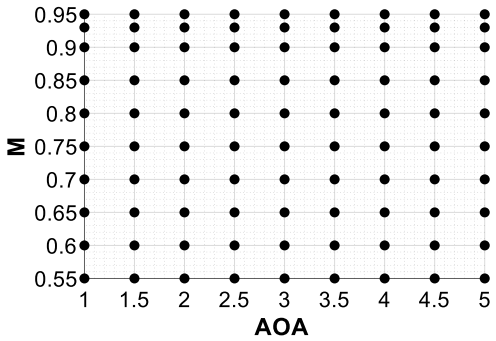

Figure 4.18. Updated dataset with 90 data points

The flow condition M=0.93 is chosen since it lies approximately in the middle of the previously used Mach numbers of 0.9 and 0.95 and also it also represents the onset of shock formation (Table D.1, in Appendix D). For this case, it is observed that 17 and 10 POD modes must be used in order to reach 90% of the energy for the rigid and aeroelastic wings, respectively. The accumulated energy, along with the NRMSE distribution across the 90 parameter points for the Cp values using these modes is provided in Appendix E. A comparison of the NRMSE distributions for the rigid and aeroelastic wings with those from the 81-sample case is presented in **Error! Reference source not found.**.

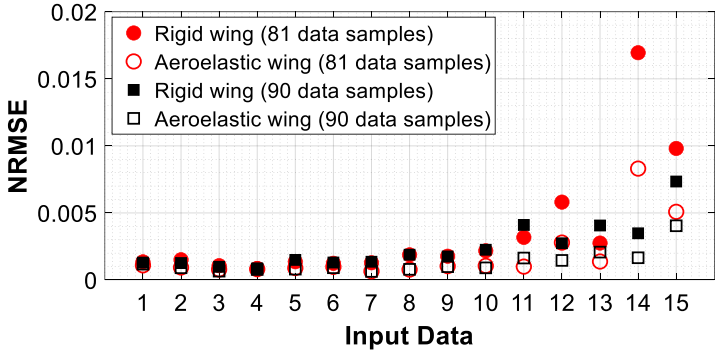

Figure 4.19. NRMSE of the Cp results for the rigid and aeroelastic wings obtained using POD-RBF

In this case, there is an increase in accuracy for the 14th prediction point, which is expected since this point corresponds to M=0.93. Additionally, improvements are observed for previously less accurate predictions, such as the 12th and 15th points. On the other hand, a slight decrease in accuracy occurs at certain points, including

the 11th and 13th. The sectional Cp distributions for the least accurate, last prediction point are presented in Figure 4.20, along with the Cp distribution on the upper surface of the 3D rigid wing shown in Figure 4.21.

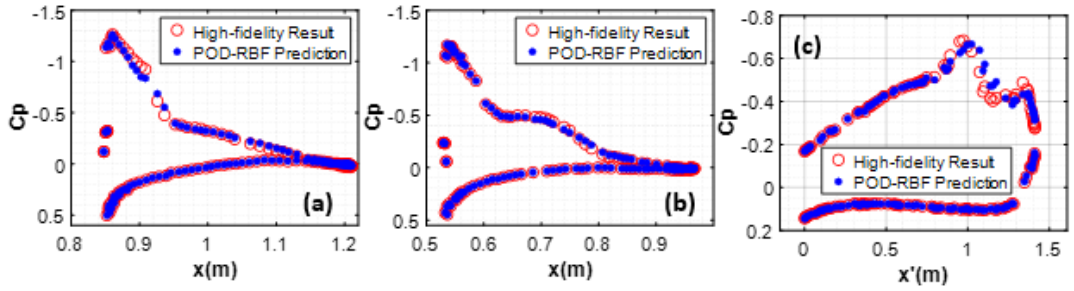

Figure 4.20. Chordwise (at 0.8m (a) and 0.5m (b) span) and spanwise (c) Cp distributions of the rigid wing for the 15th prediction point

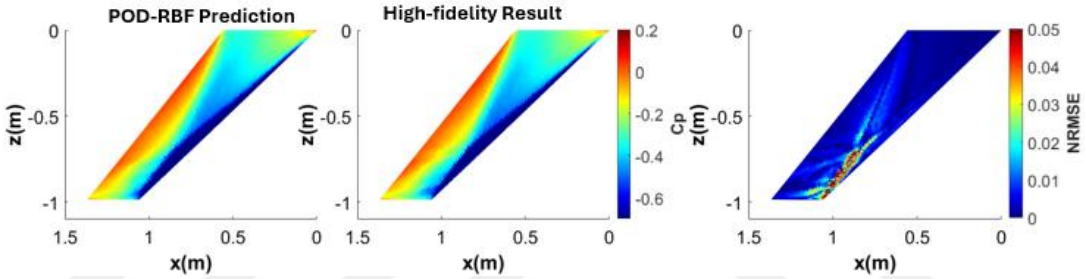

Figure 4.21. Cp distribution on the upper surface of the rigid wing for the 15th flow condition (M=0.944 and AOA=4.74°)

A better match is observed compared to the previous case as expected, however, as clearly shown by the NRMSE distribution on the upper surface of the wing (Figure 4.21), the accuracy decreases near the wing tip where flow distortion intensifies.

Similarly, the corresponding results for the aeroelastic wing are presented in Figure 4.22 and Figure 4.23.

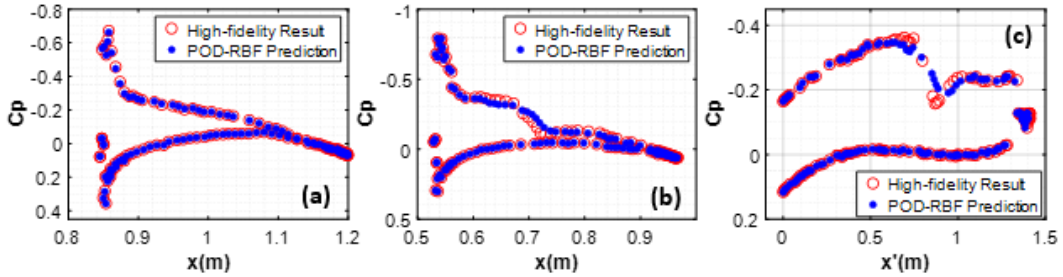

Figure 4.22. Chordwise (at 0.8m (a) and 0.5m (b) span) and spanwise (c) Cp distributions of the aeroelastic wing for the 15th prediction point

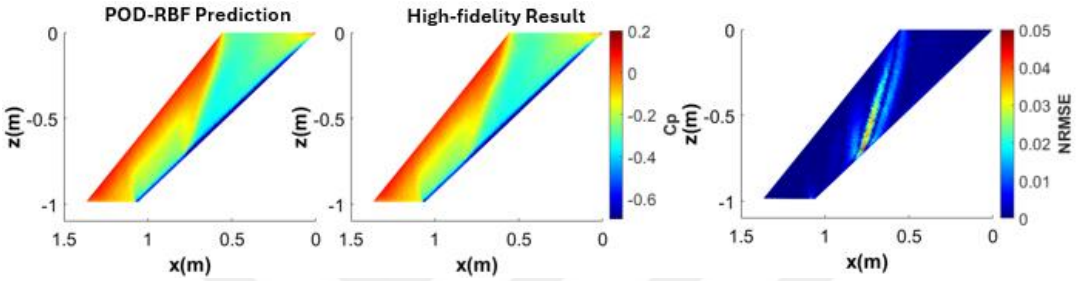

Figure 4.23. Cp distribution on the upper surface of the aeroelastic wing for the 15th flow condition (M=0.944 and AOA=4.74°)

For the least accurate flow condition of the aeroelastic wing, the overall prediction accuracy remains satisfactory. However, compared to the results obtained using the 63-sample dataset, a clear reduction in accuracy is observed in the shock-affected regions. This suggests that while the global flow features are well captured, the model's ability to accurately resolve localized flow discontinuities, particularly shock locations, deteriorates when using the expanded dataset which includes flow conditions with shock formation. However, it should be noted that, for the least accurate flow condition, the C_L values from the FOM are 0.2044 for aeroelastic wing and 0.3840 for the rigid wing, while the corresponding ROM results are 0.2045 and 0.3850, respectively using 90 data samples. Given the close agreement, these ROM predictions are suitable for many applications where C_L is required.

4.3 Surrogate Modeling with RBF

In this part, a surrogate model is developed based on the RBF interpolation method using the dataset given in Figure 3.1, which has previously been employed in

conjunction with POD based ROM. The surrogate model aims to predict the results at intermediate variables that do not exist in the original data ensemble as before, however; unlike the previous application, the model is not reduced instead it is constructed directly using the original snapshot matrix. For both rigid and aeroelastic wings, NRMSE values of the Cp distribution for each intermediate variable given in Figure 4.1 is presented in Figure 4.24. These values are derived from both the coupled POD-RBF reduced order and the RBF-based surrogate model, providing a comparative analysis of their predictive performance across the different flow conditions.

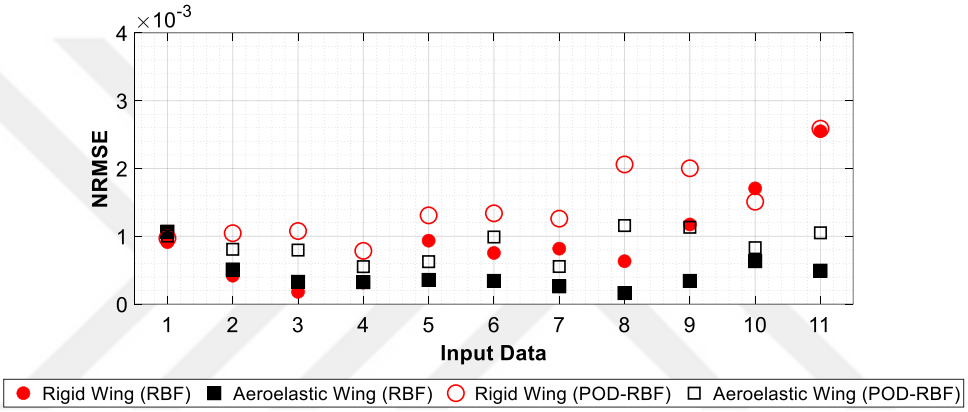

Figure 4.24. NRMSE of the Cp results for rigid and the aeroelastic wings via the coupled POD-RBF ROM and the RBF-based surrogate model predictions

As with the POD-RBF ROM predictions, all NRMSE values for the RBF based surrogate model are below 3×10^{-3} for both rigid and aeroelastic wing configurations, showing the high accuracy of the surrogate model in terms of Cp variation results (the NRMSE results of the surrogate model constructed by cubic spline interpolation method are also provided in Appendix F). Similar to the findings from the POD-RBF predictions, the results for the aeroelastic wing exhibit greater accuracy than those for the rigid wing in most of the flow cases. On the other hand, it is seen that for flow conditions with a low Mach number, the accuracy of the results for both configurations is very similar. In addition, it is also seen that even though both methods give highly accurate results, the predictions from the RBF-based surrogate model show a slightly higher accuracy than those from the POD-RBF ROM. The reason can be attributed to the fact that the RBF method is applied directly to the

original snapshot matrix in the surrogate model, eliminating the loss of accuracy associated with reduced-order modeling. Thus, the slight increase in accuracy observed for the surrogate model is a reasonable outcome as it exploits the full dataset. Cp variations along the spanwise and the chordwise sections given in Figure 3.2 at the intermediate flow variable pair of M=0.83 and AOA=4.75° for the rigid and the aeroelastic wings are presented in Figure 4.25.

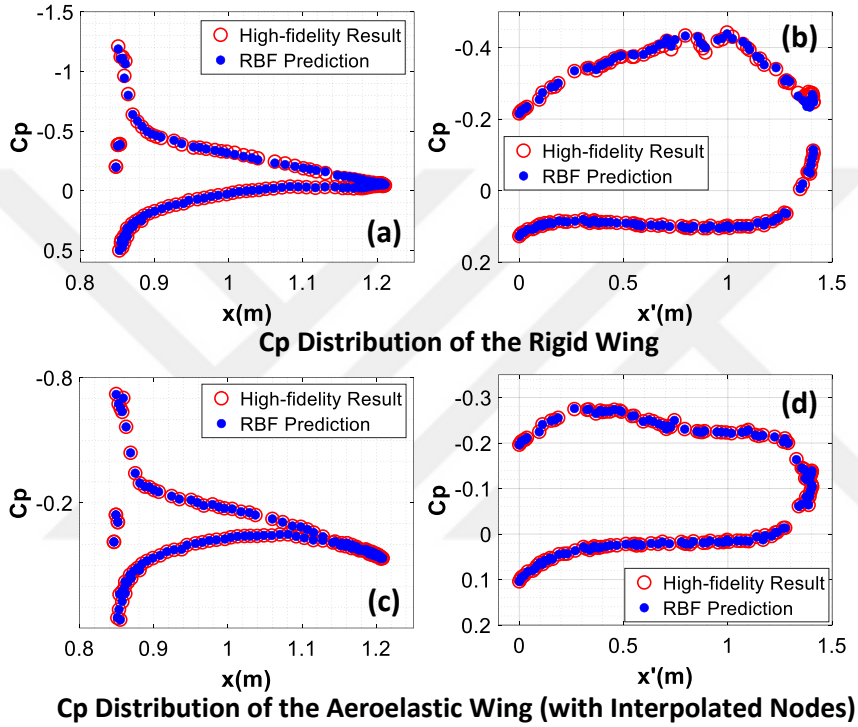

Figure 4.25. Variation of Cp along the chordwise ((a) and (c)) and spanwise ((b) and (d)) wing sections predicted via the RBF-based surrogate model

As Figure 4.25 shows that the sectional Cp variations predicted by the surrogate model exhibit very good agreement with those obtained from the high-fidelity CFD analysis.

As in the case of the coupled POD-RBF ROM approach for the aeroelastic wing, a separate surrogate model is constructed utilizing the snapshot matrices corresponding to the positions of the nodes. Maximum deflections at the intermediate flow condition of M=0.83 and AOA=4.75° obtained from high-fidelity static aeroelastic analysis and the RBF surrogate model prediction are 0.1454 m and 0.1459

m, respectively, indicating a great match. Additionally, the von Mises stress distribution for the same flow conditions is derived from the snapshot data using the RBF-based surrogate model. The maximum von Mises stresses as well as maximum deflections obtained from both methods are summarized in Table 4.1.

Table 4.1. Maximum deflection and von Mises stress results for the POD-RBF ROM and RBF based surrogate models (M=0.83 and AOA=4.75°)

	High-fidelity	**POD-RBF**	**RBF**
Maximum Deflection (m)	0.1454	0.1470	0.1459
Maximum von Mises Stress (MPa)	8.88	8.94	8.95

The results show that both the POD-based ROM coupled with the RBF method and the RBF-based surrogate model have almost the same accuracy, very close to the results of the high-fidelity analysis. In terms of computational time, a comparison of the methods is given in Table 4.2.

Table 4.2. Comparison of the computational time for the Cp distribution for the rigid and the aeroelastic wing (M=0.83 and AOA=4.75°)*

	High-fidelity	**POD-RBF**	**RBF**
Rigid Wing	1366.5 s	3.2 s	3.6 s
Aeroelastic Wing	3251.2 s	10 s	13 s

* On an AMD Ryzen 7-5800X 8-Core processor and 3.80 GHz computer

As shown in Table 4.2, employing either the POD-based ROM or the RBF-based surrogate model to predict the solutions for flow conditions not contained in the original data set results in significant savings in computational time. It should be noted that for the aeroelastic wing, the interpolation of the nodal positions is also included in the computational time for both the POD-RBF based ROM and the RBF-based surrogate modeling; therefore, the overall computational time is higher for aeroelastic wing than for the rigid wing.

In this part of the study, it is seen that both the coupled POD-RBF ROM and RBF-based surrogate modeling exhibit almost the same level of accuracy. However, there is a slight difference in terms of computational time such that the RBF-based

surrogate model has higher computational cost than the POD-RBF-based reduced order model. This discrepancy arises because the RBF-based surrogate model involves the RBF interpolation of the whole data set; whereas, for the POD-based ROM, RBF interpolation is applied only to the POD coefficient matrix whose data size is notably smaller in size than the snapshot matrix. In scenarios involving complex analysis models with a greater number of data points and nodes, the difference in computational time is likely to increase substantially, accompanied by an inevitable increase in memory demand.

4.3.1 Sampling with Latin Hypercube Sampling Method

In the preceding part, it was asserted that highly accurate results are achieved through the utilization of RBF-based surrogate model constructed from a uniformly sampled snapshot matrix. While uniform sampling is straightforward and easy to implement, it can be highly computationally expensive for high-dimensional and complex problems. For such cases, the LHS method is frequently favored as a design of experiment solution, as in the studies referenced in [18],[37],[42],[51]. Therefore, in this part LHS is employed to reduce the number of parameter pairs used to create a snapshot matrix for the aeroelastic wing. Exploiting the LHS method, the number of samples are reduced consecutively, with the goal of lowering the computational cost associated with high-fidelity analyses while maintaining the accuracy of the surrogate model predictions. This approach aims to achieve an optimal balance between efficiency and accuracy in the modeling process. Within the intervals of Mach numbers ranging from 0.55 to 0.85 and AOA from 1º - 5º as before, results for 30, 15 and 7 parameter pairs are compared. The parameter pairs generated through the LHS method are shown in Figure 4.26

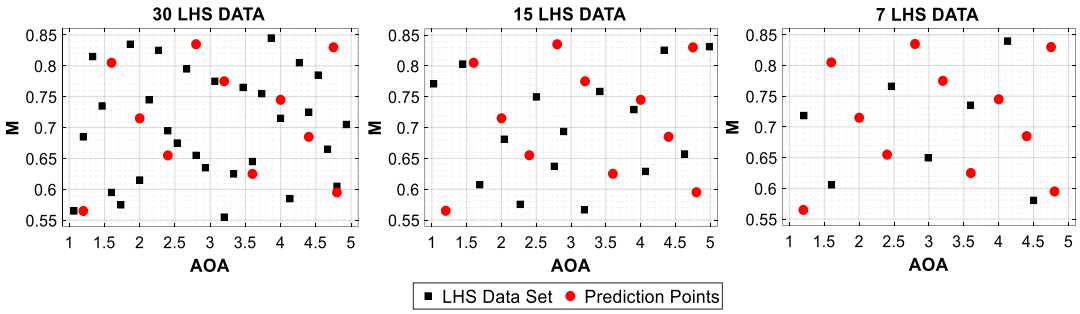

Figure 4.26. Parameter pairs used for the snapshot matrix and prediction

To construct a surrogate model, snapshot matrices for new parameter sets generated through the LHS method must be created. For this reason, instead of performing high-fidelity analyses, the previously constructed, highly accurate RBF-based surrogate model using the 63-parameter set is utilized to obtain the results for the new parameters thereby enabling a significant time saving. For 2 randomly chosen LHS parameters (employed to create a surrogate model) given in Figure 4.27, a comparison is made between the RBF based surrogate model utilizing 63 samples and the high-fidelity results.

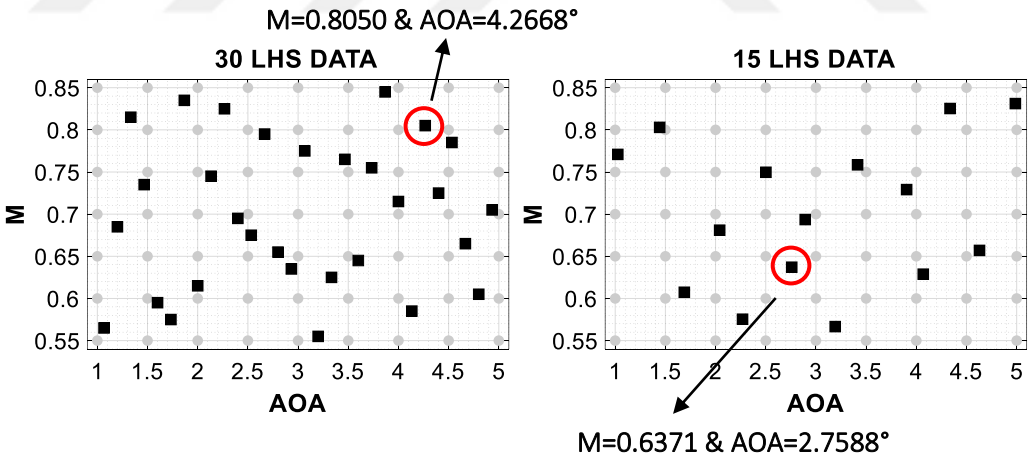

Figure 4.27. Randomly selected parameters pairs of M=0.8050 and AOA=4.2668° and M=0.6371 and AOA= 2.7588° from 30 LHS parameters and 15 LHS parameters case, respectively

The sectional Cp distribution results are given in Figure 4.28 which demonstrates the accuracy of the model.

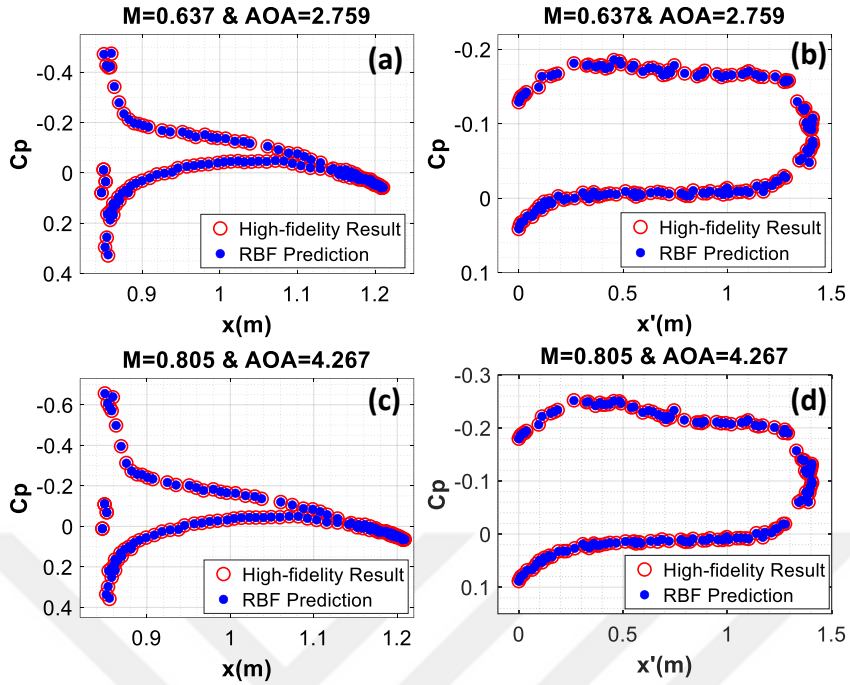

Figure 4.28. Chordwise ((a) and (c)) and spanwise ((b) and (d)) Cp distributions for aeroelastic wings at two different flow conditions

As in the previous case, the Cp results at the same intermediate flow conditions given in Figure 4.1 are predicted using the RBF surrogate model constructed with LHS parameters and the results are compared with the high-fidelity analysis results. The predicted results from the surrogate models constructed with 30, 15 and 7 LHS parameter sets are shown in Figure 4.29.

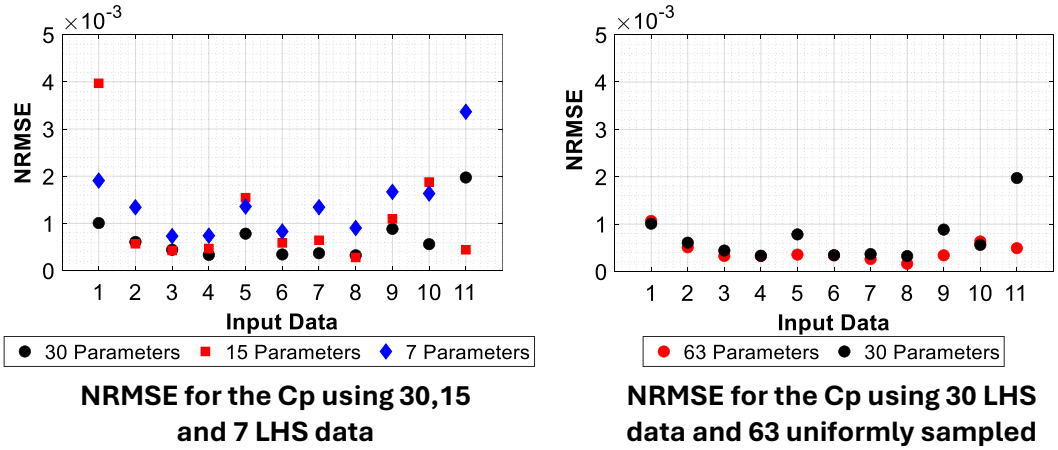

Figure 4.29. NRMSE for the Cp results using the RBF method with different number of input pairs

The NRMSE results indicate that despite a significant reduction in the number of parameter pairs, the predictions still maintain a satisfactory level of accuracy. As shown in Figure 4.29a, the results from the case with 30 parameters exhibit the highest accuracy for most intermediate flow conditions, as expected. Additionally, Figure 4.29b compares the NRMSE values for the Cp predictions derived from the RBF-based surrogate model constructed using both 63 uniformly sampled and 30 LHS-sampled datasets. It is seen that both cases demonstrate nearly equivalent accuracy levels. The accuracy of each case is also compared with the results obtained using the linear interpolation method, as presented in Appendix G. For the 11th intermediate flow condition (M=0.83 & AOA=4.75º), where the difference is more than the others, the results are investigated in detail at the chordwise and spanwise sections of the wing in Figure 4.30.

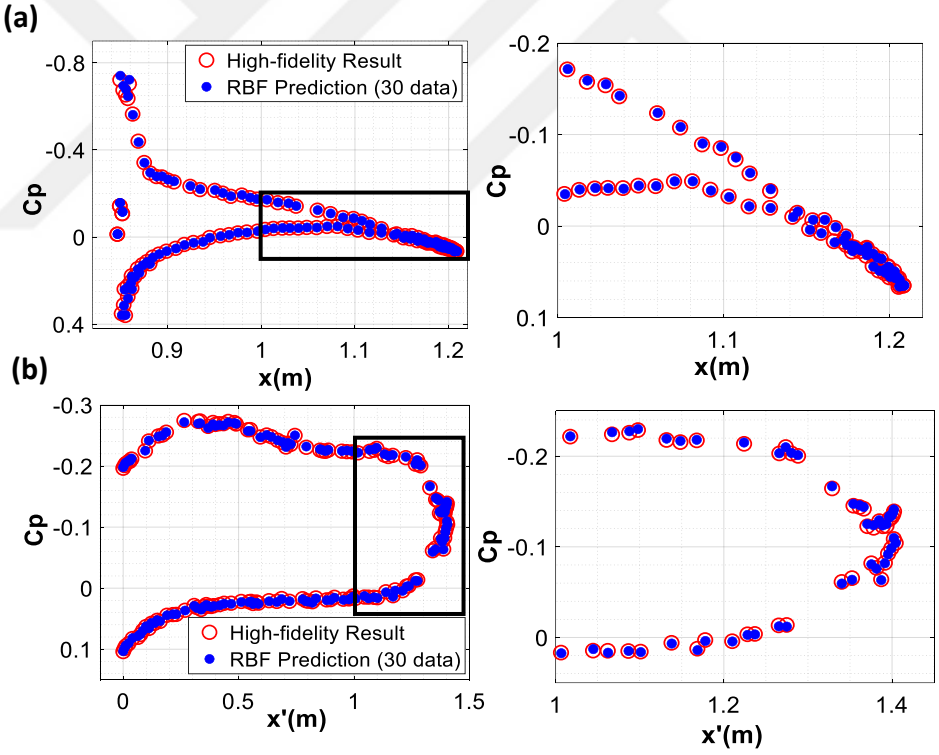

Figure 4.30. Variation of the Cp along the chordwise (a) and spanwise (b) wing sections obtained by the high-fidelity analysis and the predicted Cp via the RBF model with 30 LHS parameters (M=0.83 & AOA=4.75º)

As in previous analyses, the change in the positions of the nodes is taken into account while constructing the Cp distribution plots. Similarly, the snapshot matrices

constructed for the node positions are sampled using 30 parameter pairs defined by the LHS method. The results corresponding to these 30 LHS parameter sets are obtained from the highly accurate RBF-based surrogate model developed earlier. In this case, the maximum displacement is found as 0.1437 m while the high-fidelity result is 0.1454 m. These findings demonstrate that the sample size can be significantly reduced through the application of the LHS method without compromising accuracy.

CHAPTER 5

REDUCED ORDER MODELING WITH POD-ANN METHOD AND SURROGATE MODELING WITH ARTIFICIAL NEURAL NETWORKS

In the preceding chapter, the RBF method was adopted to develop a reduced-order model through coupling with the POD method. Additionally, it was also employed to construct an efficient surrogate model. This chapter focuses on leveraging the artificial neural network methodology which has gained significant attention and widespread adoption across various engineering fields. This chapter aims to investigate the potential of ANN in achieving similar objectives with the RBF, namely, the construction of an efficient surrogate model and the development of reduced order model by coupling it to the POD.

5.1 Artificial Neural Network (ANN) Method

ANN is a powerful data-driven method inspired by the functioning of biological neural networks. While processing data, artificial neural networks are prone to errors during their initial learning phases which enables improvements through the learning process. Network structure calculates its error and adjusts the weights of its nodes or neurons to compensate. This iterative process of error correction and adaptive learning enables neural networks to refine their performance over time. Among the various types of ANN, the feedforward neural network is the type of the ANN where the information is transmitted only in one direction, from input to output, with no loops or circles. As it is illustrated in Figure 5.1, a typical network comprises an input layer, one or more hidden layers and an output layer, each consisting of interconnected neurons. This structure enables the network to create a nonlinear mapping between input and output spaces that may have different dimensionalities.

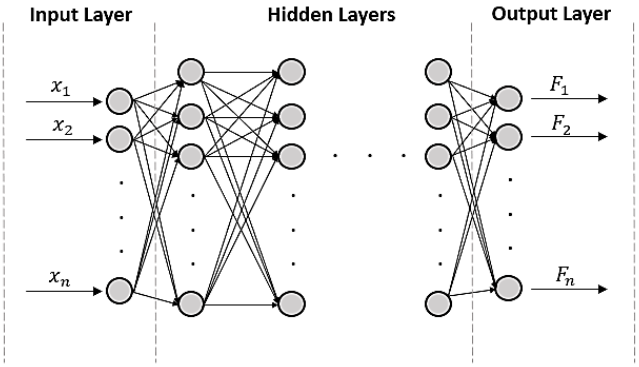

Figure 5.1. Schematic diagram of the artificial neural network

The inputs are transferred through successive layers appointed by an appropriate weight. Each layer has a corresponding transfer or activation function and each neuron has an associated bias. This process can be viewed as a sequence of intermediary transformations that bridge the input space to the output space. Applying a transfer or activation function, f, to the weighted inputs and the bias forms the outputs of the neuron which feeds the neurons of the following layer. For the l^{th} layer, input (x) of the neuron is obtained as:

$$x_n^l = f^l\left(\sum_{m=1}^{N^{l-1}} w_{nm}^l \, x_m^{l-1} + b_n^l\right) \tag{14}$$

here w_{nm}^l and b_n^l denotes the weight and bias of the n^{th} neuron of the l^{th} layer, respectively; m denotes the number of neurons of the preceding layer (l-1) and N is the total number of neurons. Feedforward neural networks often have hidden layers with sigmoid neurons and an output layer of linear neurons. The use of multiple layers with nonlinear activation functions enables the network to learn complex, nonlinear relationships between inputs and outputs. Sigmoid functions are nonlinear, monotonic, continuous, and differentiable, and their derivatives can be expressed in terms of the function itself, which simplifies the process of deriving weight update equations using the backpropagation algorithm. For pattern recognition tasks, the log-sigmoid function is commonly used at the output layer because it restricts the output to a range between 0 and 1. However, for function fitting problems, such as

the one in this study, a linear transfer function is more appropriate for the output layer. The tan-sigmoid function, which is similar to the log-sigmoid, confines the output between -1 and 1. One key difference is that the gradient of the tan-sigmoid is greater than that of the log-sigmoid, which helps accelerate the training process. In this study, the tan-sigmoid function is used in the hidden layers while a linear transfer function is applied at the output layer which are shown in Figure 5.2.

$$f(x) = \frac{2}{1 + e^{-2x}} - 1 \qquad f(x) = x$$

Figure 5.2. Tan-Sigmoid and Linear Transfer Functions

Having constructed the network structure, the process is followed by the training stage. In this stage weights and biases are adjusted by some learning rule until the network provides acceptable responses for the inputs. The accuracy of the network is determined by the mean squared error (MSE) between the network output (p) and targets (t).

$$\mathrm{MSE} = \frac{1}{N}\sum_{i=1}^{N}(t_i - p_i)^2 \tag{15}$$

The algorithm should adjust the network parameters in order to minimize the mean square error or loss/performance function. A backpropagation algorithm is utilized where the errors in the output of the network are propagated back through the layers to determine the optimal values of weight and bias. Since the derivatives are processed from the last layer of the network to the first, the process is referred to as backpropagation. During training, backpropagation is used to optimize the weights and biases by computing the gradient of the MSE with respect to each parameter and adjusting them to minimize the error as given Equation (15). At the $(k+1)^{th}$ iteration, the weights (w) and biases (b) are updated as given in Equation (16).

$$w_{k+1} = w_k - \alpha\frac{\partial \mathrm{MSE}}{\partial w} \qquad b_{k+1} = b_k - \alpha\frac{\partial \mathrm{MSE}}{\partial b} \tag{16}$$

where α is the learning rate. This equation is iterated until the network converges. For the training of multilayer feedforward networks, Matlab Neural Network Toolbox offers many optimization algorithms in its library as it is given in Table 1.

Table 5.1. Training Algorithms [59]

Training Algorithms
Levenberg-Marquardt
Bayesian Regularization
BFGS Quasi-Newton
Resilient Backpropagation
Scaled Conjugate Gradient
Conjugate Gradient with Powell/Beale Restarts
Fletcher-Powell Conjugate Gradient
Polak-Ribiére Conjugate Gradient
One Step Secant
Variable Learning Rate Gradient Descent
Gradient Descent with Momentum
Gradient Descent

The differences between the algorithms occur in the way in which the resulting derivatives are used to update the weights. Among the training algorithms given in Table 5.1, Levenberg-Marquart (LM) [60] stands out as the fastest backpropagation algorithm in the toolbox and utilized as a first-choice algorithm [61]. LM is a combination of gradient descent and Gauss-Newton methods, providing the advantages of both; it behaves like gradient descent when far from the solution for stability and like Gauss-Newton when near the solution for faster convergence.

Levenberg-Marquart Algorithm

According to Newton's method, optimizing a performance function, F(**x**), is written as:

$$\mathbf{x}_{k+1} = \mathbf{x}_k - \left[\nabla^2 F(\mathbf{x})|_{x=x_k}\right]^{-1} \left[\nabla F(\mathbf{x})|_{x=x_k}\right] \tag{17}$$

where,

$$F(\mathbf{x}) = \sum_{i=1}^{N} (t_i - p_i)^2 = \sum_{i=1}^{N} v_i^2(\mathbf{x}) = \mathbf{v}^{\mathbf{T}}(\mathbf{x})\mathbf{v}(\mathbf{x}) \tag{18}$$

The gradient of the $F(\mathbf{x})$ can be written in terms of the Jacobian Matrix as:

$$\nabla F(\mathbf{x}) = 2\mathbf{J}^{\mathbf{T}}(\mathbf{x})\mathbf{v}(\mathbf{x}) \quad \text{where } \mathbf{J}(\mathbf{x}) = \begin{bmatrix} \frac{\partial v_1(\mathbf{x})}{\partial x_1} & \cdots & \frac{\partial v_1(\mathbf{x})}{\partial x_n} \\ \vdots & \ddots & \vdots \\ \frac{\partial v_N(\mathbf{x})}{\partial x_1} & \cdots & \frac{\partial v_N(\mathbf{x})}{\partial x_n} \end{bmatrix} \tag{19}$$

The other term in Equation (17) is the Hessian Matrix. In terms of Jacobian Matrix, it can be approximated as:

$$\nabla^2 F(\mathbf{x}) = 2\mathbf{J}^{\mathbf{T}}(\mathbf{x})\mathbf{J}(\mathbf{x}) \tag{20}$$

Then Equation (17) can be rewritten as:

$$\mathbf{x}_{k+1} = \mathbf{x}_k - [\mathbf{J}^{\mathrm{T}}(\mathbf{x}_k)\mathbf{v}(\mathbf{x}_k)]^{-1}\, \mathbf{J}^{\mathrm{T}}(\mathbf{x}_k)\mathbf{v}(\mathbf{x}_k) \tag{21}$$

which is the Gauss-Newton approximation. For the Levenberg-Marquart approximation, the equation is updated by introducing the damping factor, μ.

$$\Delta\mathbf{x}_k = -[\mathbf{J}^{\mathrm{T}}(\mathbf{x}_k)\mathbf{v}(\mathbf{x}_k) + \mu_k \mathbf{I}]^{-1}\, \mathbf{J}^{\mathrm{T}}(\mathbf{x}_k)\mathbf{v}(\mathbf{x}_k) \tag{22}$$

where $\mathbf{I}$ is the identity matrix. Here as μ_k increases the algorithm approaches the steepest descent algorithm while μ_k decreases to 0, the algorithm becomes the Gauss-Newton. It can be seen that the main drawback of the LM algorithm is the storage requirement. The algorithm must store the Hessian matrix of nxn where n is the number of weights and biases in the network. When the number of parameters exceed the available storage capacity, then the method cannot be applied. Then, for training of the large networks, Scaled Conjugate Gradient (SCG) method developed by Moller [62] is an efficient algorithm to be used.

Scaled Conjugate Gradient Algorithm

SCG is an extension of the Conjugate Gradient (CG) method that introduces a scaling mechanism to improve convergence, especially in large-scale and complex optimization problems. The CG method is an iterative technique aiming to minimize a function. It generates a series of search directions that are conjugate (or orthogonal) relative to the Hessian matrix. The main concept is to move towards the minimum by following these conjugate directions, which helps to achieve faster convergence.

In the CG method, the update rule for the parameters (weight and bias) is given as,

$$\mathbf{x}_{k+1} = \mathbf{x}_k + \alpha_k \mathbf{d}_k \tag{23}$$

where $\mathbf{x}_k$ is the parameter vector and α_k is the step size. In the CG method, the update direction $\mathbf{d}_k$ (at iteration k) is determined by the following:

$$\mathbf{d}_{k+1} = -\nabla F(\mathbf{x}_k) + \beta_k \mathbf{d}_k \tag{24}$$

Here, β_k is the scalar that controls how the search direction changes over time and F is the objective function given in the quadratic form as:

$$F(\mathbf{x}) = \frac{1}{2}\mathbf{x}^T(\nabla^2 F(\mathbf{x}))\mathbf{x} - (\nabla F(\mathbf{x}))\mathbf{x} \tag{25}$$

The SCG method aims to scale the gradients and use the conjugate directions for faster convergence without needing the full Hessian matrix as given by Equation (26),

$$\nabla F_{scaled}(\mathbf{x}) = C\nabla F(\mathbf{x}) \tag{26}$$

where C is a diagonal scaling matrix. d_k in SCG can be written as,

$$\mathbf{d}_{k+1} = -\nabla F_{scaled}(\mathbf{x}_k) + \beta_k \mathbf{d}_k \tag{27}$$

In SCG, the step size is determined based on the gradient and conjugate directions as,

$$\alpha_k = \frac{\nabla F(\mathbf{x}_k)^T \nabla F_{scaled}(\mathbf{x}_k)}{\mathbf{d}_k{}^T \mathbf{H} \mathbf{d}_k} \tag{28}$$

where **H** is the approximation of the Hessian. A key advantage of Moller's SCG method [62] is that it does not require the computation or storage of the full Hessian matrix. Instead, the SCG method uses only first-order derivatives (the gradients) to perform the update.

In this study, both LM and SCG methods are employed for training different models. It should be noted that each time a network is trained, the initialization of the weight and bias values can lead to different solutions. As a result, the network is retrained multiple times to achieve the most accurate results of the targets. For training, 70% of the data is used, while the remaining 30% is split equally for validation (15%) and testing (15%). The training points are required to adjust the network parameters while the validation points serve to assess the network's ability to generalize and impede overfitting. Training of the network stops when there is no improvement in the generalization. The test points do not affect the training process, they provide an independent measure of the network performance. Once the network is trained and validated, it can be used to provide solutions at intermediate data points. The results obtained using different data split ratios are detailed in Appendix H.

5.2 Reduced Order Modeling with POD coupled with ANN

In Chapter 3, it is demonstrated that a reduced order model with POD method can be constructed for pressure coefficient distribution employing 8 modes for rigid wing and 5 modes for the aeroelastic wing. Subsequently, in Chapter 4, RBF is adopted as an interpolation method for the POD basis coefficients. In the current chapter, ANN is used for this purpose. To construct a network, the two flow parameters are used as inputs while the corresponding POD coefficients are the outputs based on the data from 63 sampled flow condition.

5.2.1 Prediction of the Results for Three-dimensional Rigid Wing Configuration

For the rigid wing case there are 8 outputs of basis coefficients for Cp corresponding to 2 input parameters. As explained in Section 5.1, Levenberg-Marquart algorithm is appropriate for the current problem. It is important to note that, each time a neural network is trained, different solutions can be obtained due to the different initialization of the weight and bias values. Therefore, the number of neurons is incrementally increased and the neural networks are retrained at least ten times to achieve the most accurate results of the targets. It should be noted that there is no rigorous rule for deciding the number of neurons in the hidden layers, and other options may also be viable. For the rigid sweptback wing and the flow conditions given in Figure 4.1, the NRMSE of the Cp results predicted via the ANN method with varying neuron numbers are presented in Figure 5.3.

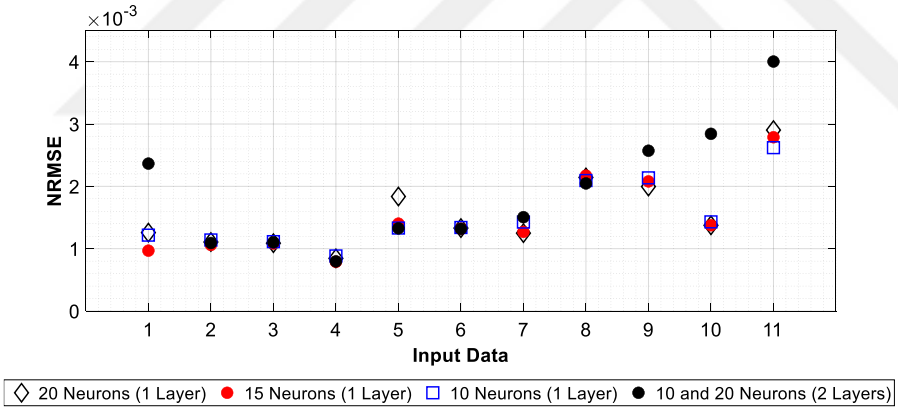

Figure 5.3. NRMSE for the Cp results of the rigid wing using the POD-ANN model with different neuron numbers

In the present study, it is observed that increasing the number layers does not make any contribution in terms of accuracy. The NRMSE comparison between the results of the single-layer networks and a two-layer network example, shown in Figure 5.3, illustrates this point. As shown in Figure 5.3, ANNs with 10, 15 and 20 neurons achieve a great accuracy with NRMSE values below 3×10^{-3} for all cases. For the majority of the cases, ANN with 15 neurons provides the most accurate results. To

validate the model's performance across the entire dataset, the relationship between the outputs (ANN predictions) and the targets (actual results) for this particular ANN configuration is given in Figure 5.4.

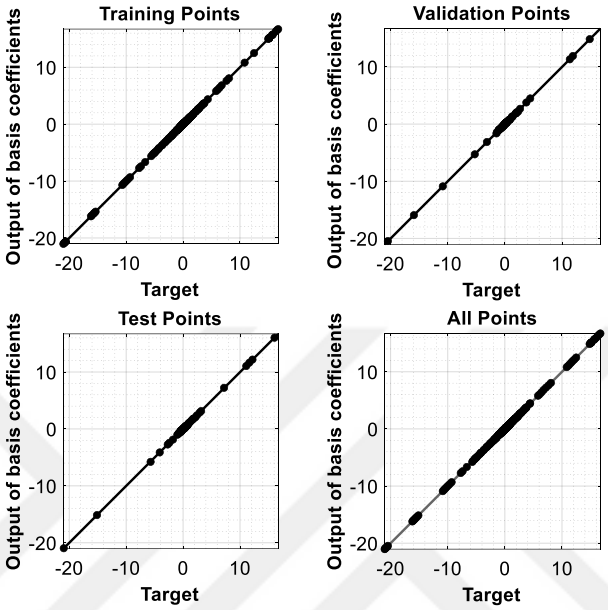

Figure 5.4. Output vs. target plots of basis coefficients for the ANN with 15 neurons

Figure 5.4 presents a comparison between the network's outputs and the corresponding targets for the training, validation, and test datasets. The proximity of the data to the diagonal line indicates the accuracy of the network; the closer the points are to the diagonal line, the more accurate the predictions. The concentration of data along the diagonal line demonstrates that the predictions of the network align closely with the actual results across all training, validation and test datasets. A disparity in accuracy between the datasets may suggest potential issues such as overfitting or extrapolation. In such cases, it would be necessary to retrain the network or consider constructing an alternative model. During the training process of the ANN, the mean squared error (MSE) plot for training, validation and test points with respect to epoch (iteration) numbers is given in Figure 5.5.

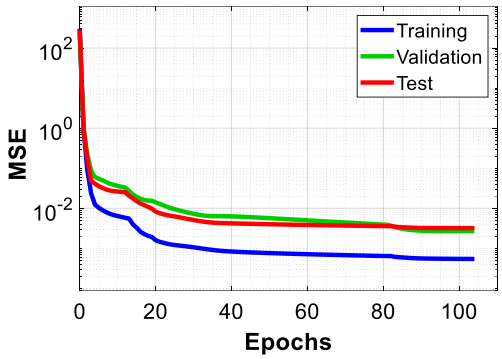

Figure 5.5. MSE vs epoch number for the ANN with 15 neurons

As mentioned in Section 5.1, validation points are used for the assessment of network generalization and if there is no improvement on the error for the validation data, the training process of the network stops. The validation error is expected to drop gradually throughout the training process, however, once the network begins to overfit the data, the error starts to increase. If the validation error continues to increase for six consecutive iterations, the training stops and the weights and biases are reverted to their values at the point of minimum validation error. For this instance, as can be seen in Figure 5.5., the training process consists of 104 epochs, which indicates that the error for the validation points reaches its minimum at the 98^{th} epoch and starts to increase in the following iterations. Therefore, the iteration process ceases at the 104^{th} epoch taking a total time of 0.204 seconds. To demonstrate the accuracy of the results further, the 11^{th} flow condition added to the LHS data set is investigated. This flow condition also corresponds to the highest NRMSE value observed for the chosen network. The Cp distributions on the top and the bottom surfaces of the rigid wing along with the NRMSE results on these surfaces are presented in Figure 5.6.

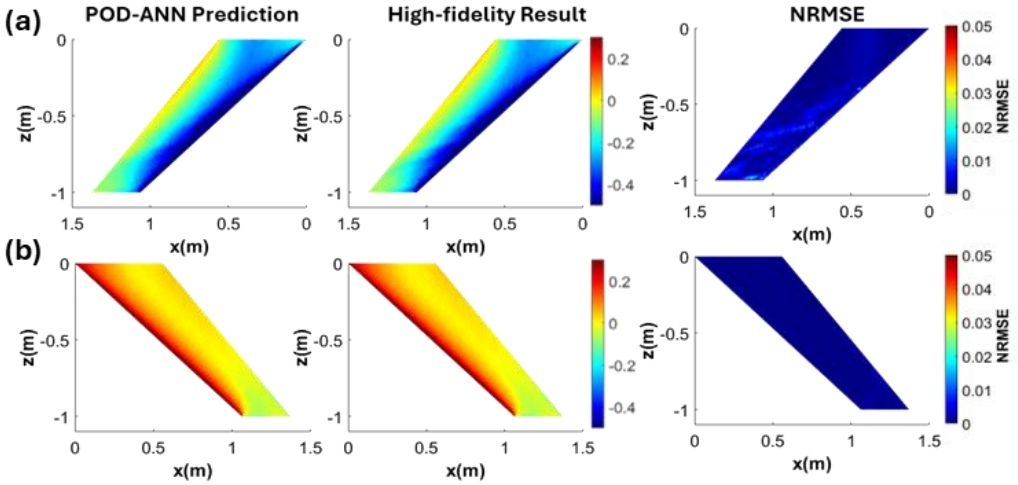

Figure 5.6. Cp distribution on the top (a) and bottom (b) surfaces of the rigid wing obtained by the high-fidelity analysis and predicted results via the POD-ANN reduced order model (M=0.83 and AOA=4.75º)

Compared to the high-fidelity results, the predicted results of ANN based surrogate model show a very good match, however; there are some local regions where the accuracy diminishes slightly on the top surface close to the tip. For this case, predicted Cp results have a R^2, RMSE and NRMSE of 0.9996, 0.0084 and 0.0037, respectively.

5.2.2 Prediction of the Results for Three-dimensional Aeroelastic Wing Configuration

In the case of aeroelastic wing, there are 5 outputs of basis coefficients for Cp corresponding to 2 input parameters. Similar to the rigid wing case, Levenberg-Marquart algorithm is used for the training of the network. The number of neurons is incrementally increased and the neural networks are retrained at least ten times to obtain the most accurate predictions of the target values. For the aeroelastic sweptback wing and the flow conditions given in Figure 4.1, the NRMSE of the Cp results predicted via the ANN method with varying neuron numbers are presented in Figure 5.7.

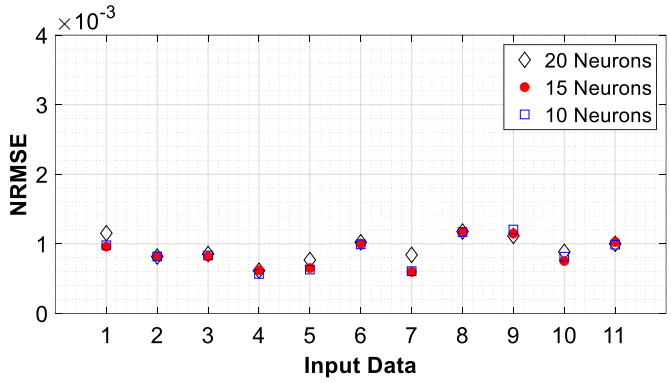

Figure 5.7. NRMSE for the Cp results of the aeroelastic wing using the POD-ANN model with different neuron numbers

Figure 5.7 presents the NRMSE of Cp results for the ANNs with a single layer containing 20, 15 and 10 neurons respectively. In all cases, NRMSE values are below 1.5×10^{-3}, indicating a high level of accuracy. However, as in the case of rigid wing, the network with 15 neurons yields the most accurate results in the majority of cases. To verify the network's performance across all flow conditions in the dataset, the output versus target plots for the training, validation, and test points are shown Figure 5.8.

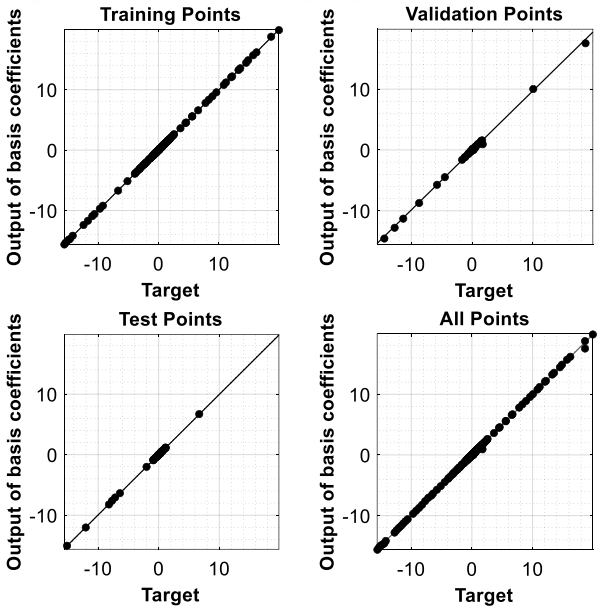

Figure 5.8. Output vs. target plots of basis coefficients for the ANN with 15 neurons for the aeroelastic wing

As Figure 5.8 shows, a perfect match is attained for all training, validation and test points. For this particular case, the performance or MSE plot for training, validation and test points with respect to epochs is given Figure 5.9.

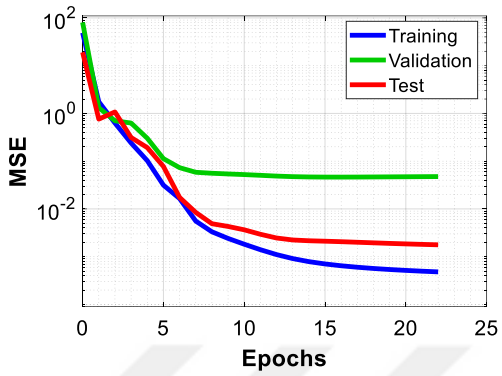

Figure 5.9. MSE vs epoch number for the ANN with 15 neurons for the aeroelastic wing

This time, the training process completes with 22 epochs and takes 0.056 s. Similarly, the minimum validation error is reached at 16th epoch and starts to increase in the following iterations. Therefore, the iteration process ceases at the 22th epoch taking a total time of 0.056 seconds. The Cp distribution is shown in Figure 5.10 on 3D wing for the 11th flow condition.

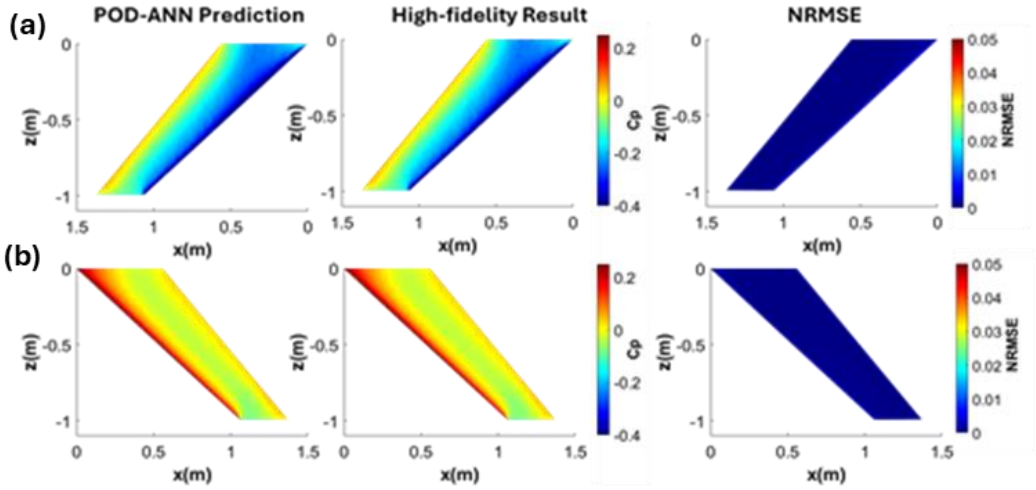

Figure 5.10. Cp distribution on the top (a) and bottom (b) surfaces of the aeroelastic wing obtained by the high-fidelity analysis and predicted results via the POD-ANN reduced order model (M=0.83 and AOA=4.75º)

The predicted results obtained using the coupled POD-ANN reduced order model have a great accuracy. The error values for aeroelastic wing and rigid wing configurations are summarized in Table 5.2.

Table 5.2. Comparison of the errors for both wing configurations using POD-ANN ROM method

	R^2	RMSE	NRMSE
Aeroelastic Wing	0.9999	0.0023	0.0010
Rigid Wing	0.9996	0.0084	0.0037

The POD–ANN method demonstrates high accuracy in predicting intermediate parameters. In the following section, the performance of the POD-ANN model is further evaluated using a dataset that includes higher Mach number conditions.

5.2.3 Prediction of the Results for a Dataset Involving Higher Mach Numbers

Similar to Section 4.2.3 where the POD-RBF is evaluated, the predictive capability of the POD-ANN method is also assessed for cases involving higher Mach numbers. The comparison of the NRMSE results for both approaches, based on the 81-sample dataset case (Figure 3.23) is presented in Figure 5.11 for the prediction points displayed in Figure 4.11.

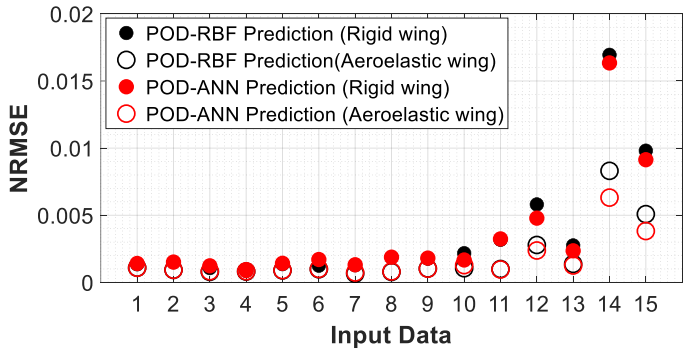

Figure 5.11 NRMSE of the Cp results obtained by using POD-RBF and POD-ANN (1 layer-35 neurons for rigid and 1 layer-9 neurons for aeroelastic wing) approaches (81 dataset)

For the rigid wing case, the NRMSE results are similar for both methods; however, the POD-ANN approach exhibits slightly higher accuracy across all data points. The most accurate ANN-based predictions for the rigid wing are obtained using a single layer containing 35 neurons. As outlined in Appendix H, the dataset is divided into 95% of training and 5% of validation data. Figure 5.12 (a) presents the NRMSE values for various ANN configurations. Although the prediction accuracies are relatively close, the highest overall accuracy is attained with the configuration comprising a single layer and 35 neurons. The corresponding output versus target plot for this configuration, including all training and validation points, is provided in Figure 5.12 (b).

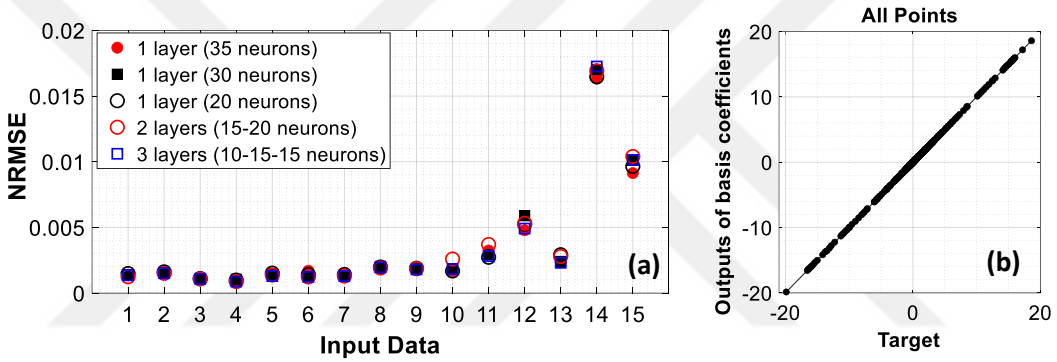

Figure 5.12 NRMSE distribution for Cp predictions of the rigid wing using POD-ANN method with different ANN configurations (a) and output vs target plot for ANN with 1 layer and 35 neurons (b)

In Figure 5.11, the difference between both POD-RBF and POD-ANN methods are more noticeable in the case of aeroelastic wing. The sectional Cp distributions for the least accurate prediction, corresponding to the 14th prediction point, using both approaches are presented in Figure 5.13.

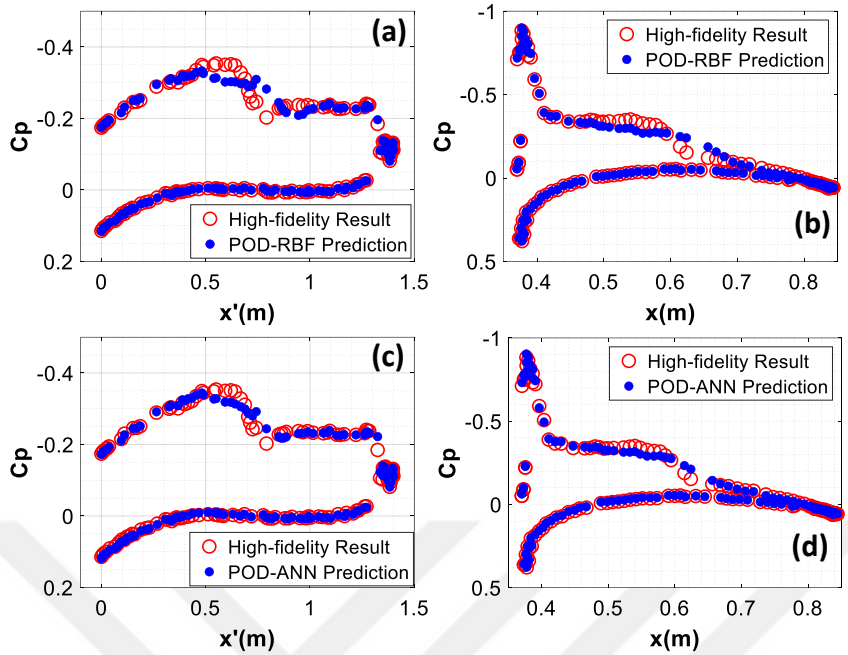

Figure 5.13 Difference in results for the aeroelastic wing at the 14th prediction point

A better match is achieved using the POD-ANN compared to POD-RBF method; however, discrepancies remain at the same locations.

For the aeroelastic wing case, the most accurate results are obtained with the POD-ANN approach, specifically using an ANN configuration consisting of a single hidden layer with 9 neurons. The performance of different ANN configurations, along with the output versus target plot for the optimal configuration (1 layer with 9 neurons), are shown in Figure 5.14 (a) and Figure 5.14 (b), respectively.

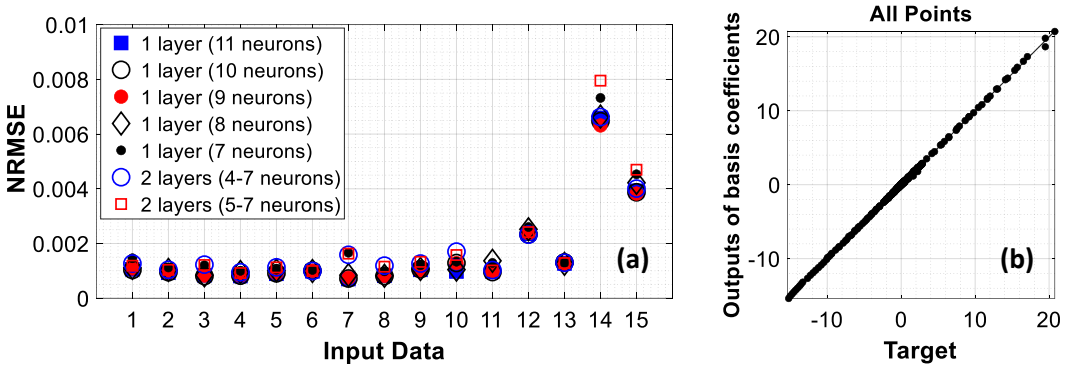

Figure 5.14 NRMSE distribution for aeroelastic Cp prediction using POD-ANN method with different ANN configurations (a) and output vs target plot for ANN with 1 layer and 9 neurons (b)

Similar to the case discussed in Section 4.2.2, in order to improve prediction accuracy under conditions with a Mach number greater than 0.9, the data density between M=0.9 and 0.95 is increased by adding flow conditions at M=0.93. A comparison of the NRMSE results for datasets containing 81 and 90 samples is given in Figure 5.15.

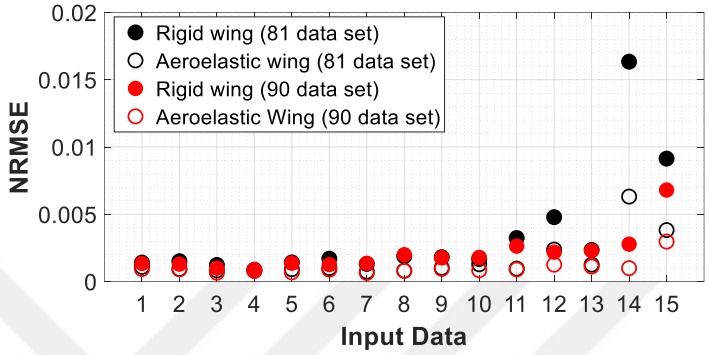

Figure 5.15 NRMSE of the Cp results for the rigid and aeroelastic wings obtained by using different datasets with POD-ANN method

With the inclusion of the intermediate Mach number M=0.93, the prediction accuracy improves across all data points. The results show that maintaining the same Mach number interval does not provide sufficient accuracy. Therefore, the interval must be reduced by introducing an additional Mach number condition of M=0.93. According to the NRMSE results, the least accurate prediction corresponds to the 15th flow condition for the rigid wing using 90-sample dataset. The sectional Cp distribution and the Cp distribution on the upper surface of the 3D rigid wing are displayed in Figure 5.16 and Figure 5.17, respectively.

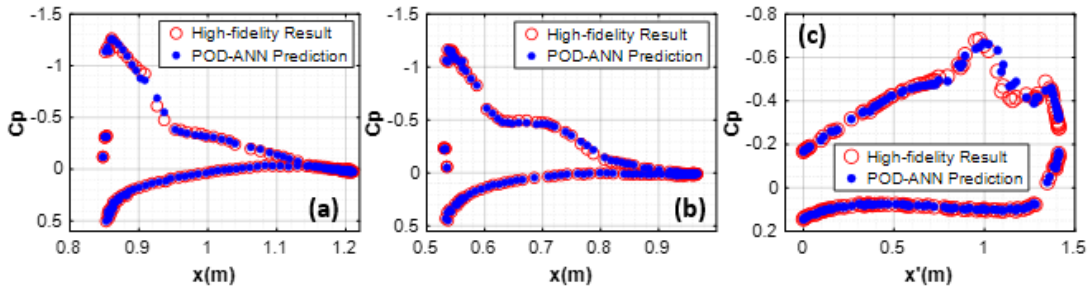

Figure 5.16 Chordwise (at 0.8m (a) and 0.5m (b) span) and spanwise (c) Cp distributions of the rigid wing obtained from POD-ANN for 15th prediction point

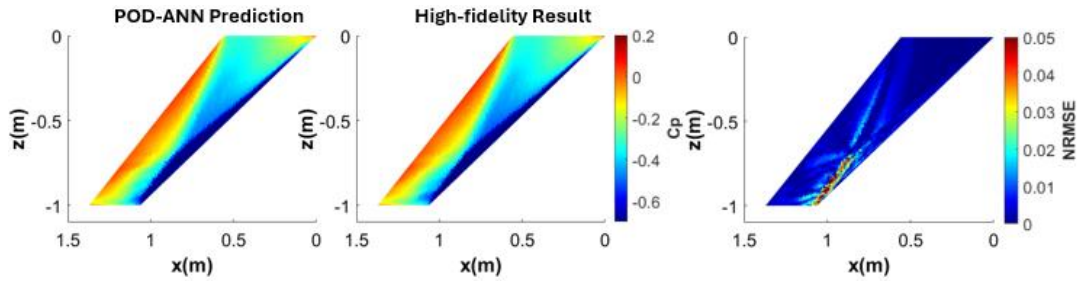

Figure 5.17 Cp distribution on the upper surface of the rigid wing for the 15th flow condition (M=0.944 and AOA=4.74°)

As observed in the case of the POD-RBF method, mismatches still occur in certain localized regions, particularly near the outboard section of the wing close to the leading edge, where flow distortions are more pronounced. The results obtained with the POD-ANN method are similar to those from the POD-RBF approach, with a slight improvement in accuracy. However, this difference in accuracy between the two methods becomes more noticeable at some prediction points. A comparison of the NRMSE results for both methods, using the dataset with 90 samples, is presented in Figure 5.18.

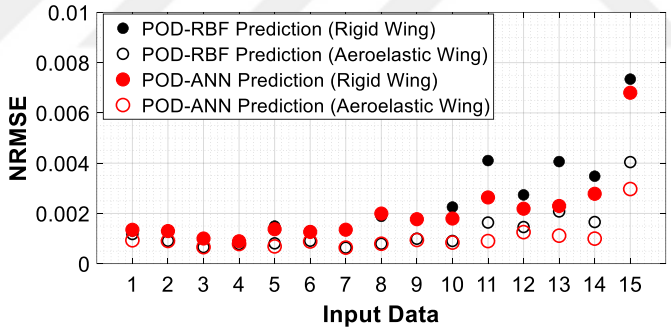

Figure 5.18 NRMSE of the Cp results for the rigid and aeroelastic wings obtained from different approaches using 90 data samples

For all prediction points, the POD-ANN approach yields more accurate results than the POD-RBF method. Moreover, the difference in accuracy between both approaches has increased compared to the case with 81 data samples. For the 13th prediction point (M=0.87 &AOA=3.6°) the spanwise Cp distributions and NRMSE distribution on the upper 3D wing surface obtained from both approaches are presented in Figure 5.19 and Figure 5.20 for rigid and aeroelastic wings, respectively.

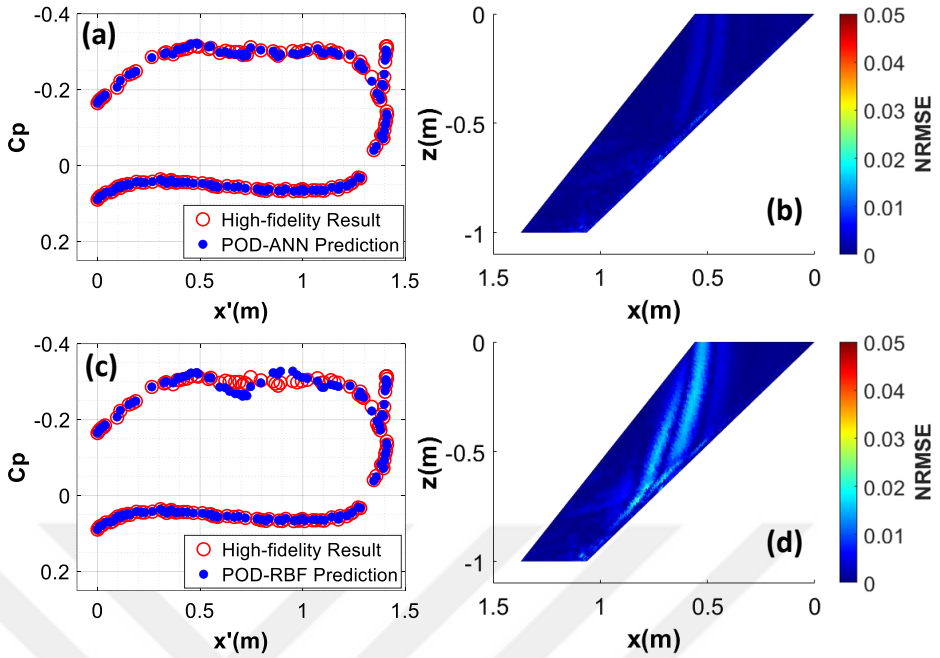

Figure 5.19. Spanwise ((a) & (c)) Cp distribution and NRMSE distribution ((b) & (d)) of the rigid wing obtained from POD-ANN and POD-RBF for the 13th point

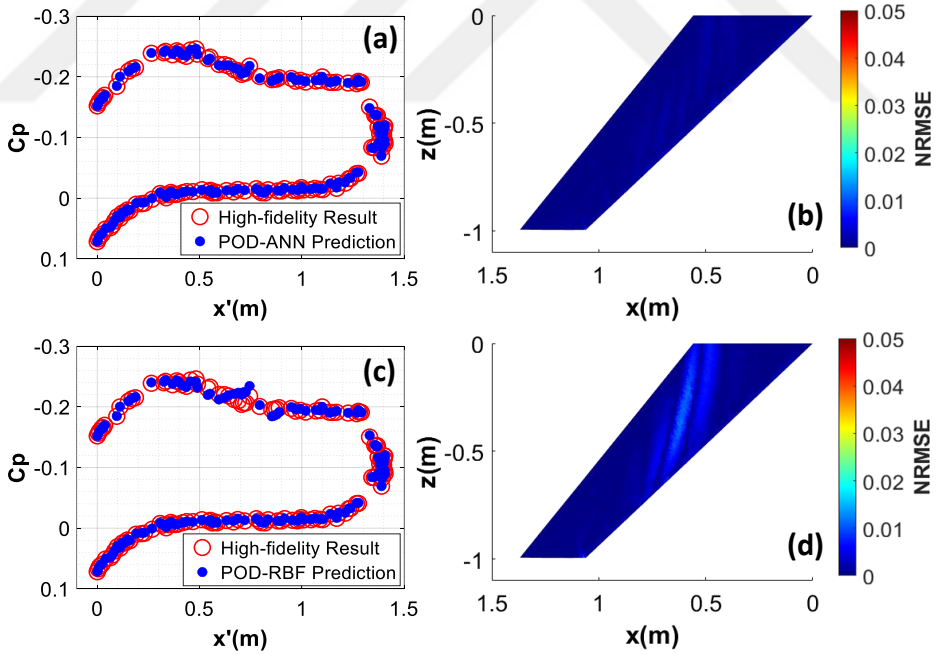

Figure 5.20. Spanwise ((a) & (c)) Cp distribution and NRMSE distribution ((b) & (d)) of the aeroelastic wing obtained from POD-ANN and POD-RBF for the 13th point

As observed in Figure 5.19 and Figure 5.20, the prediction accuracy is enhanced through the use of the POD–ANN method for both the rigid and aeroelastic wing cases, compared to the POD–RBF approach. For the rigid wing case, the highest accuracy is achieved using an ANN configuration comprising 2-layers with 10 and 20 neurons, respectively. In the aeroelastic wing case, the most accurate results are obtained with a 2-layer ANN containing 15 and 20 neurons. Output versus target plots for this ANN configuration are provided in Appendix I, along with the NRMSE values for alternative ANN configurations.

Figure 5.21 presents the predicted displacement results at the same prediction point for the aeroelastic wing case.

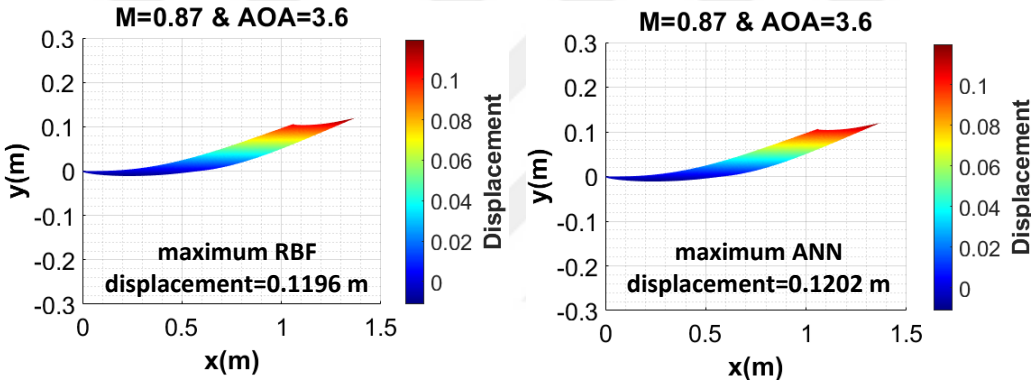

Figure 5.21. Predicted displacement using both approaches for the 13th prediction point (M=0.87 and AOA=3.6°)

The corresponding ANN used for nodal positions consists of a single layer with 15 neurons for each coordinate direction. The actual maximum displacement obtained from the FOM analysis is 0.1198 m, confirming that both methods yield highly accurate approximations in terms of displacement results as seen in Figure 5.21.

Figure 5.22 presents the sectional Cp distributions, along with the NRMSE distribution on the upper surface of the wing, for the least accurate case (the 15th flow condition) of the aeroelastic wing.

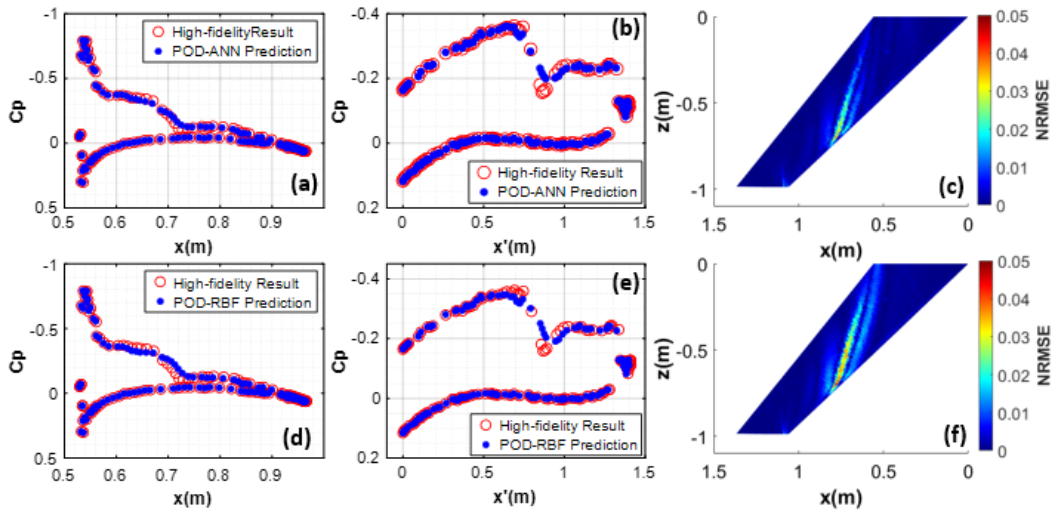

Figure 5.22. Chordwise at 0.5 m span ((a) & (d)) and spanwise Cp distributions ((b) & (e)) along with the NRMSE distribution on the upper surface of the aeroelastic wing ((c) & (f)) obtained from POD-ANN and POD-RBF predictions at 15th point

Similarly, it can be seen that the prediction accuracy increases compared to POD-RBF method with the use of the POD-ANN prediction. The NRMSE results show that the prediction accuracy for the aeroelastic wing is higher than that for the rigid wing configuration consistent with the findings discussed in Chapter 3. In this section, higher Mach numbers are included into the parameter domain to increase the system nonlinearity by introducing shock formations. The impact of high Mach numbers is more pronounced in the rigid wing configuration. Figure 5.23 presents the variation in Cp distribution with increasing Mach number for both configurations.

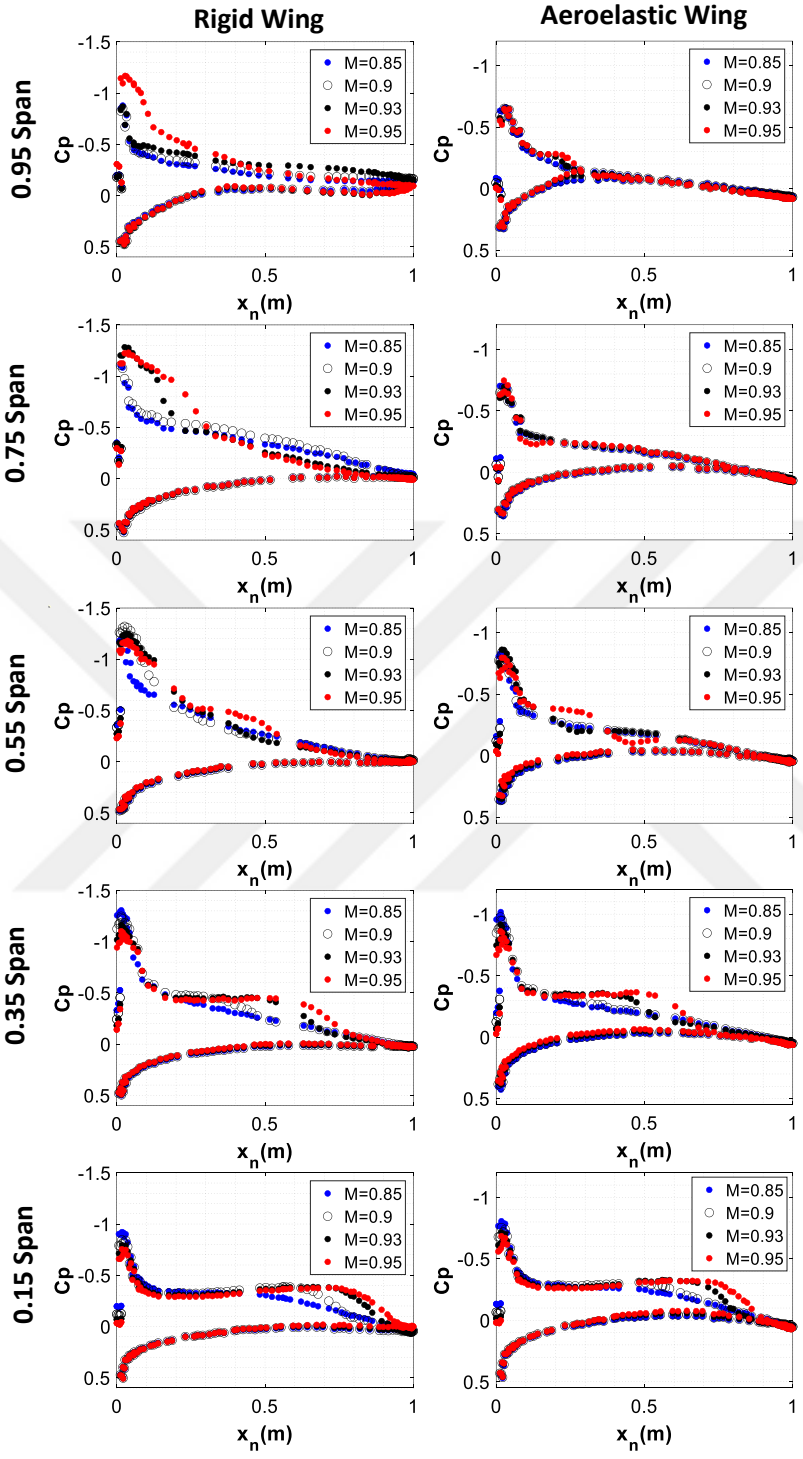

Figure 5.23. Cp vs normalized chord (x_n) of the rigid wing and the aeroelastic wing (AOA = 5º for M = 0.85, 0.9, 0.93 and 0.95)

In Figure 5.23, the chordwise Cp distributions are presented taken from various wing sections, as illustrated in Figure 3.17. The graphs reveal that the aeroelastic wing's Cp results are less sensitive to changes in Mach number compared to those of the rigid wing. In the aeroelastic configuration, flow discontinuities are primarily observed at the middle and inboard section of the wing. In contrast, the rigid wing exhibits more pronounced variations in Cp; a rapid change observed around the 0.75 span location, indicating a presence of shock. On the inboard section of the wing, close to the root, both configurations display similar behavior. The discrepancy on the outboard half can be attributed to significant change in the effective angle of attack due to the bending-torsion coupling of the aeroelastic wing, as discussed in detail at Chapter 3. Consequently, the data for rigid wing exhibit higher nonlinearity, making it a more challenging case. Therefore, while the results for the aeroelastic wing can be considered acceptable using the POD-ANN approach with the 90-sample dataset, the results for the rigid wing can be improved. For this reason, the data density for the rigid wing is increased by reducing the Mach interval to 0.01 between Mach 0.90 and 0.95 in order to evaluate its effect on prediction accuracy. Additionally, a Mach condition of M=0.96 is included to further enrich the dataset, resulting in 126 parameter pairs as displayed in Figure 5.24.

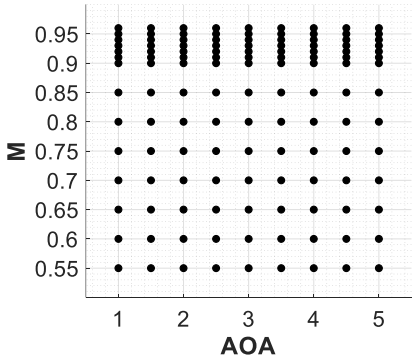

Figure 5.24. Extended dataset with 126 samples

In this case, there are 126 flow conditions in total, and capturing 90% of the energy requires using 24 out of the 126 modes. The accumulated energy based on the mode numbers and the NRMSE distribution for the reconstructed Cp of the rigid wing is given in Appendix E.

Using the POD-based reduced order model constructed with 24 modes, the NRMSE distribution of the 15 prediction points is presented in comparing the performances of both POD-RBF and POD-ANN methods.

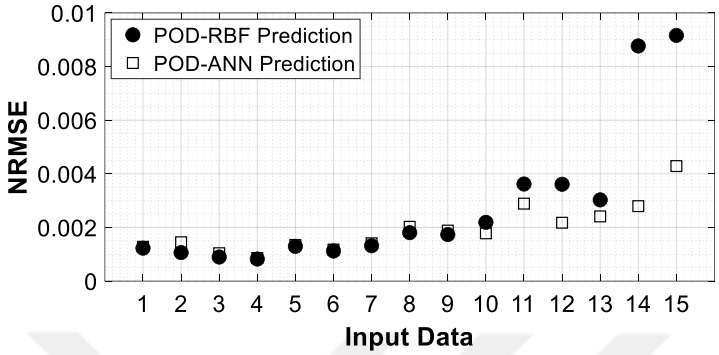

Figure 5.25 NRMSE of the Cp results for the rigid wing obtained from both approaches using 126-sample dataset

Figure 5.25 shows that the POD-ANN approach significantly outperforms the POD-RBF method at higher Mach conditions. In this case, the most accurate results are achieved using a network with 3 layers containing 10, 15 and 25 neurons, respectively. Similar with the other cases investigated in this Section of 5.2.3, 95% of the data is used for training and 5% is used for validation, as detailed in Appendix H. All NRMSE values are below 0.005, indicating great prediction accuracy compared to the RBF method. The NRMSE results for other ANN configurations as well as the output vs. target plots of basis coefficients for the chosen ANN configuration are provided in Appendix I. The spanwise Cp distributions for the 14th and 15th prediction points are given in Figure 5.26.

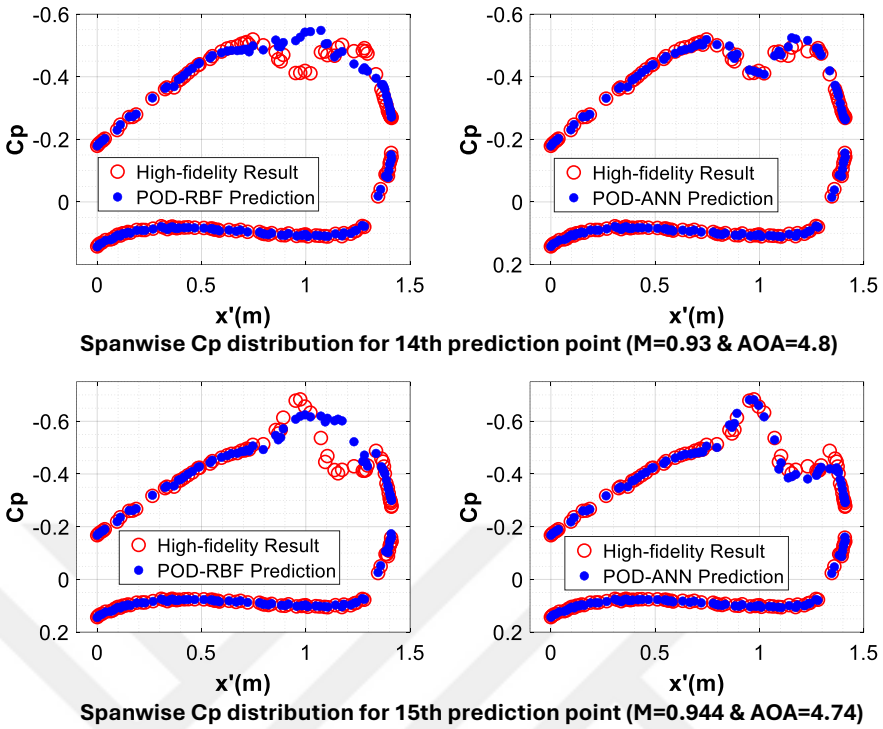

Figure 5.26 Spanwise Cp distributions for the 14th and 15th prediction point obtained using POD-ANN and POD-RBF approaches (126-sample dataset)

In the case involving 126 data samples, it is clear that the Cp predictions obtained using the POD-ANN method are significantly more accurate than those produced by the POD-RBF approach A summary of the NRMSE results for varying dataset sizes is provided for both methods in Figure 5.27

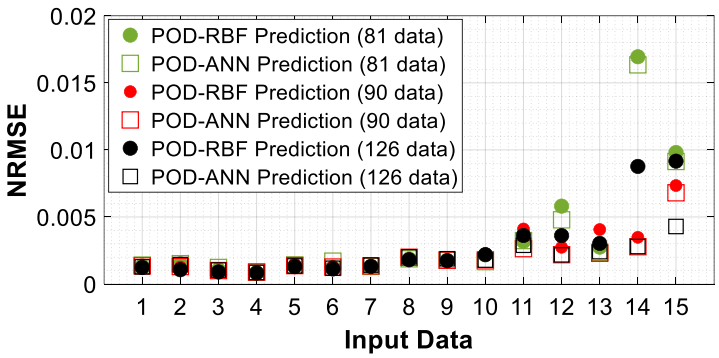

Figure 5.27. NRMSE distribution for Cp prediction of the rigid wing using POD-ANN and POD-RBF methods for different number of datasets

The results show that, across all cases the POD-ANN approach consistently yields more accurate predictions than the POD-RBF method. This suggests that in cases where nonlinear behaviour is present, the ANN approach is more effective in capturing the underlying complexities of the system. It is also noteworthy that while the accuracy of the ANN predictions improves with an increasing number of data points, this trend is not observed for the RBF method. Specifically, when the data interval between Mach 0.90 and 0.95 is reduced - resulting in an increase in the total number of data points from 90 to 126 - the prediction accuracy of the RBF method actually decreases within this range. This decrease in performance appears to result from the RBF model becoming too sensitive to small fluctuations in the densely sampled region, indicating potential overfitting and a reduced ability to generalize across the entire domain. Therefore, in such cases, the POD-ANN method is recommended over the POD-RBF method due to its superior robustness and predictive accuracy. In addition, the performance of basic bilinear interpolation across different dataset sizes is also provided in Appendix J. These results suggest that when data density is sufficiently high and computational efficiency or minor accuracy differences are not a primary concern, simpler interpolation methods may also serve as a viable alternative.

5.3 Surrogate Modeling with ANN

In this section, the training of the ANN is conducted using 2 input parameters; while the Cp results at 20366 nodes on the wing surface serve as the output variables for 63 uniformly sampled flow conditions, presented in Figure 3.1. The large size of the output significantly increases the network's complexity, leading to considerable memory demands. To manage the training of such large networks, the SCG method, as described in Section 5.1 is employed for optimizing the ANN structure. In this case, the results from ANN models with more than one layer show that increasing the number of layers does not improve performance. However, increasing the number of neurons in the network has a notable impact on the accuracy of the results.

For the rigid wing and the flow conditions shown in Figure 4.1, the NRMSE of the Cp results predicted via the ANN method with varying neuron numbers are presented in Figure 5.28.

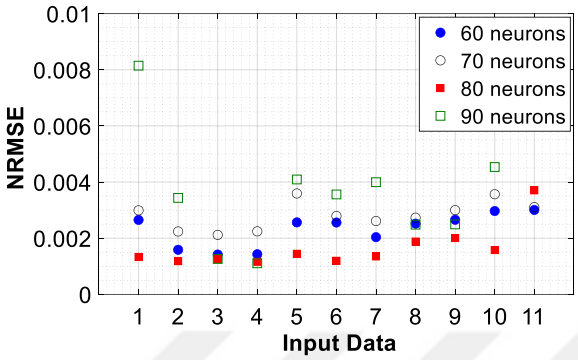

Figure 5.28. NRMSE for the Cp results using the ANN based surrogate model with different neuron numbers for the rigid wing

From the NRMSE results for each flow condition presented in Figure 4.1, it is observed that for all cases NRMSE results are below 4×10^{-3} indicating the accuracy of the predictions. However, the most accurate predictions are achieved with the ANN model containing 80 neurons in the majority of cases. The plots given in Figure 5.29 shows the relationship between the outputs and the targets for this particular ANN configuration, constructed for the rigid wing, with a single layer consisting of 80 neurons.

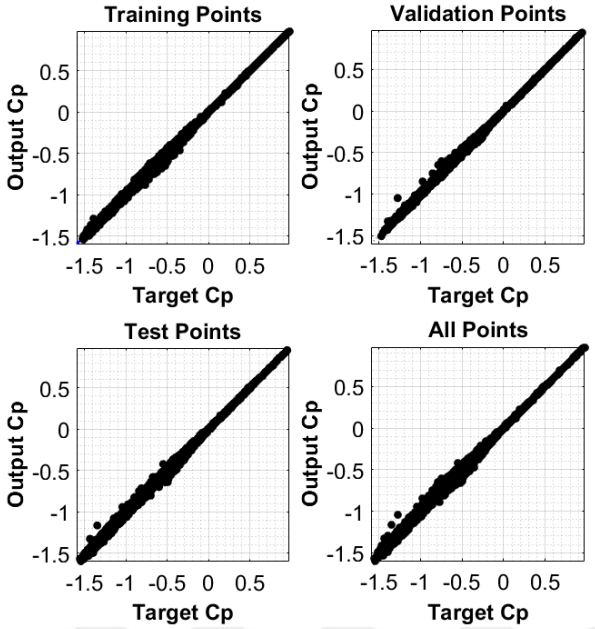

Figure 5.29. Output vs. target plots of Cp results for the ANN with 80 neurons for the rigid wing

In the current case, despite the presence of a few outliers, the outputs show good alignment across all subsets of training, validation, and test points, demonstrating the network's adequacy. The NRMSE of the network predictions for the Cp results of the aeroelastic wing are presented in Figure 5.30.

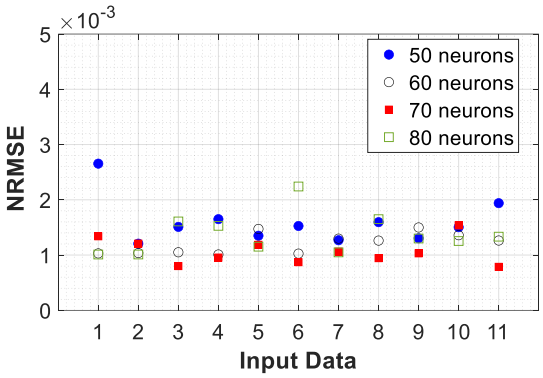

Figure 5.30. NRMSE for the Cp results using the ANN based surrogate model with different neuron numbers for the aeroelastic wing

Compared to the rigid wing, the increase in the accuracy of the results can be seen. For all cases NRMSE values are below 3×10^{-3}. This time the most accurate results are obtained with a network with 1 hidden layer consisting of 70 neurons. The

outputs and the targets for this ANN with a single layer consisting of 70 neurons are presented in Figure 5.31.

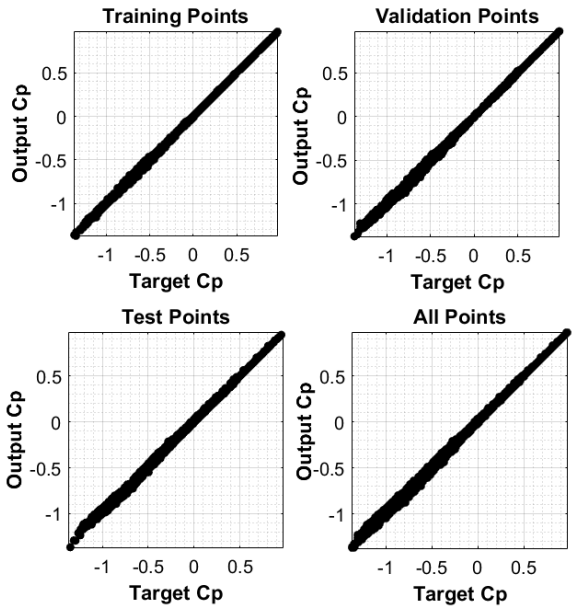

Figure 5.31. Output vs. target plots of Cp results for the ANN with 70 neurons for the aeroelastic wing

The predictions of the single layered ANN constructed with 70 neurons for the aeroelastic wing show a great accuracy for all the training, validation and test points in data set as can be seen in Figure 5.31. The MSE plot with respect to epoch number is given in Figure 5.32 for both ANNs constructed for rigid and aeroelastic wings.

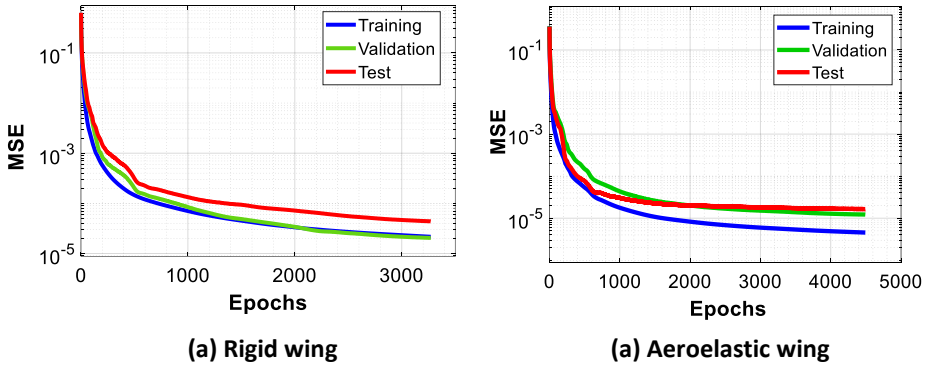

Figure 5.32. MSE vs epoch number for the ANN with 80 neurons for rigid wing (a) and 70 neurons for aeroelastic wing (b)

The epoch number and computational time of the training process are summarized in Table 5.3 together with the values for POD-ANN models constructed for 63-sample dataset.

Table 5.3. Comparison of the CPU time of training and epoch number for different methods*

	Rigid Wing		Aeroelastic Wing	
	Training Time	**Epoch Number**	**Training Time**	**Epoch Number**
POD-ANN ROM	0.204 s	104	0.056 s	22
ANN Surrogate Model	535 s	3271	674 s	4492

* On an AMD Ryzen 7-5800X 8-Core processor and 3.80 GHz computer

From the Table 5.3, a notable difference in computational time between the POD-ANN method and the ANN-based surrogate model is evident. This difference is expected, given that the surrogate model involves a significantly larger number of outputs compared to the POD-based ANN model. The increased output size requires a nearly five-fold increase in the number of neurons to reach accurate predictions. As the network size expands, the computational demands grow accordingly. In addition, the fastest training algorithm, Levenberg-Marquardt, available in the Matlab library, cannot be used due to its excessive memory requirements. Consequently, this increase in network complexity results in a considerable increase in the overall computational time required for the training process.

The computational time for predictions is also compared between both methods in the case of rigid wing at M=0.83 & AOA=4.75º as presented in Table 5.4.

Table 5.4. Comparison of the CPU time of prediction for different methods (rigid wing for M=0.83 & AOA=4.75º)*

Method	**High-fidelity Analysis**	**ANN Analysis**	**POD-ANN Analysis**
CPU Time	1366.5 s	0.3 s	1.2 s

* On an AMD Ryzen 7-5800X 8-Core processor and 3.80 GHz computer

It can be observed that the computational cost for the POD-ANN method is slightly higher than the ANN method. However, when compared to the computational cost of high-fidelity analysis, this difference becomes negligible, as both methods significantly reduce overall computational time. Even if the computational cost can be expensive especially for the ANN based surrogate model, it can be said that once the network is constructed, the prediction of the results for desired parameters are computationally efficient for both approximations. The accuracy of both methods is compared in Figure 5.33

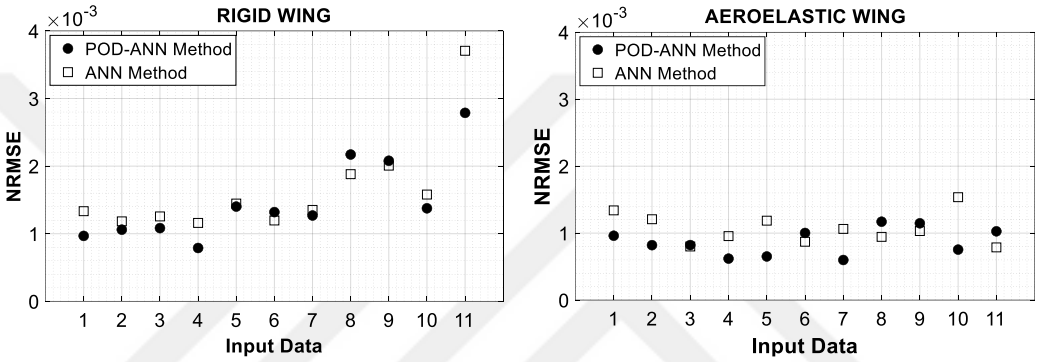

Figure 5.33. Comparison of NRMSE for the Cp results using 2 different methods for the rigid and aeroelastic wings

Figure 5.33 shows that, while the accuracy of the two methods is quite similar, the POD-ANN method yields slightly more accurate results in the majority of cases. This highlights the efficiency of the POD-ANN approach over the ANN-based surrogate model. Despite the potential loss of accuracy due to the reduced-order modeling, the POD-ANN method remains more accurate. Additionally, as presented in Table 5.3, the training process for the ANN-based surrogate model is significantly more computationally expensive than the POD-ANN method, considering that multiple trials are required to identify the optimal network configuration for maximum accuracy. Therefore, for the current study, it is clear that combining the ANN with the POD method offers a more efficient solution, both in terms of accuracy and computational cost. In Figure 5.34, the POD-ANN predictions of Cp are compared with the POD-RBF results for 63-sample dataset.

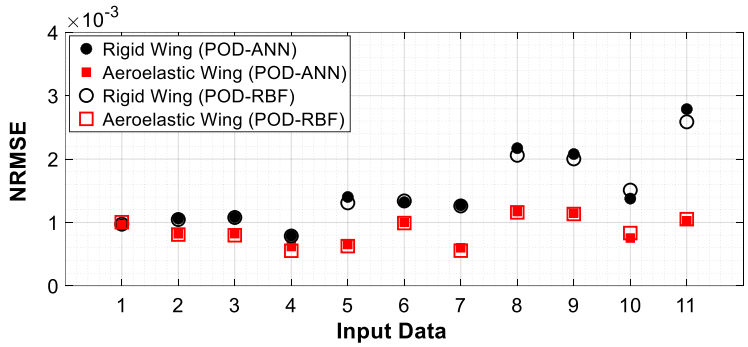

Figure 5.34. Comparison of NRMSE for the Cp results using POD based ROMs (63-sample dataset)

The comparison of NRMSE results indicates that the accuracy of the POD-based reduced-order models, when coupled with either ANN or RBF methods, is nearly identical, demonstrating a high level of accuracy in both cases, provided that higher Mach number conditions, which significantly distort the flow, are excluded from the dataset. It is also seen from the graphs that as the M and AOA increase, the NRMSE also increases as well in the rigid wing case. This can be attributed to the onset of flow separation at higher M and AOAs, a phenomenon that is discussed in detail in Section 3.2.2. As flow separation begins to occur on the rigid wing, the complexity of the aerodynamic behavior increases, leading to a higher prediction error and, consequently, a higher NRMSE. The predictive performance of the POD-based ROMs on parameter pairs outside the dataset is provided in Appendix K. Additionally, the CPU times are compared in Table 5.5.

Table 5.5. Comparison of the CPU time of prediction for different methods (rigid wing for M=0.83 & AOA=4.75º)*

Method	High-fidelity Analysis	POD-ANN Analysis	POD-RBF Analysis
CPU Time	1366.5 s	1.2 s	3.2 s

* On an AMD Ryzen 7-5800X 8-Core processor and 3.80 GHz computer

It can be observed that the computational cost for the POD-RBF method is slightly higher than the POD-ANN method. However, when compared to the computational cost of high-fidelity analysis, this difference becomes negligible, as both methods substantially reduce the overall computational time. Consequently, either approach

can be considered a suitable alternative, offering comparable advantages in terms of both accuracy and computational efficiency.

CHAPTER 6

CONCLUSIONS AND FUTURE WORKS

6.1 Conclusions

In this study, high-fidelity reduced order and surrogate models are developed by leveraging the POD, RBF and ANN methods. The findings reveal the notable effect of wing elasticity on the performance of these models. Specifically, it is observed that reduced-order modeling is more effectively applied to the aeroelastic wing when the Cp is taken as the output variable.

For the elongated AGARD 445.6 wing configuration under investigation, capturing 90% of the total energy requires 8 POD modes in the case of the rigid wing, based on the dataset presented in Figure 3.1. On the other hand, the aeroelastic wing achieves the same energy threshold with only 5 POD modes. The primary reason for this behavior can be attributed to the bending-torsion coupling mechanism that occurs in sweptback wing geometries. This coupling effect reduces the effective angle of attack in the aeroelastic wing configuration. Consequently, it is inferred that, due to the flow separation observed on the rigid wing as opposed to the aeroelastic wing, the Cp distribution pattern is disrupted, requiring a higher number of modes to capture 90% of the energy. In contrast, the Cp distribution pattern for the aeroelastic wing remains relatively stable compared to the rigid wing, leading to more efficient reduced-order modeling for the aeroelastic configuration.

The prediction capability of the POD-based ROM is further assessed by coupling it with both RBF and ANN approaches. To evaluate this, predictions are performed at 11 intermediate data points, which are not included in the original dataset. The test points are selected using the LHS method to ensure a representative distribution within the parameter space. The results show that, compared to the rigid wing case, both the coupled POD-RBF and POD-ANN reduced-order models, with only 5 POD

modes, yield slightly more accurate predictions of the Cp distribution for the aeroelastic wing. It is observed that, for the rigid wing, localized regions of reduced accuracy occur near the tip along the upper surface. The streamlines on the wing reveal that flow separation progressively increases from wing root toward the tip. This behavior is particularly noticeable due to the relatively thin airfoil, which tapers further toward the tip, making it more susceptible to separation. In contrast, for the aeroelastic sweptback wing, the streamlines remain undisturbed and smoothly follow the contour of the airfoil, with no significant separation. This improved flow characteristic is attributed to the reduction in the effective angle of attack caused by the inward twist of the aeroelastic wing as a result of bending, which prevents the onset of separation.

In addition, for the aeroelastic wing, the deflection causes the node positions to shift, requiring distinct node configurations for each analysis case, unlike the rigid wing. To improve the accuracy of Cp distribution predictions, separate snapshot matrices for the deformed x, y, and z coordinates of the nodes must be used, with the POD-based ROM applied to these positions. For highly flexible wings with significant deflections, the deformation of the nodes becomes essential for accurately capturing the Cp distribution as rigid node assumption is insufficient for precise Cp modeling in flexible wings. Moreover, as a by-product of the separate ROMs generated for the node positions, the wing's deflection can also be accurately predicted. Similarly, the von-Mises stress distribution for the aeroelastic wing can be reconstructed with high accuracy using the same process, while significantly reducing the model order.

To predict the results outside the original dataset, POD can be integrated with various regression techniques. In this study, RBF and ANN methods are employed for this purpose, with ANN specifically used for predicting Cp values. The findings show that, when coupled with the POD method, both the RBF and ANN approaches yield nearly identical predictions, demonstrating a high level of accuracy at intermediate prediction points within the dataset presented in Figure 3.1. In terms of computational cost of prediction time, the POD-RBF method is slightly more expensive than the POD-ANN method. However, when compared to the

computational cost of high-fidelity analyses, this difference is negligible, as both methods significantly reduce overall computational time. Therefore, either method can be considered a viable option, offering comparable benefits in terms of both accuracy and computational efficiency. On the other hand, each POD-based ROM approaches is further evaluated using the extended datasets that include higher Mach conditions, which lead to the formation of shock waves. Under these conditions, although the prediction accuracy decreases in regions near shock formation for both methods, the POD-ANN approach consistently outperforms the POD-RBF approach in terms of predictive accuracy. This implies that the ANN is better suited for capturing the complex dynamics associated with high-speed flows. Moreover, it is observed that while ANN performance improves with more data, RBF tends to overfit in densely sampled regions, reducing its accuracy. Hence, for such cases POD-ANN can be preferred over the POD-RBF method due to its enhanced robustness and predictive accuracy. It is also observed that as the dataset is expanded to include higher Mach numbers, the number of POD modes required to construct a ROM increases while the prediction accuracy decreases, particularly when the sampling interval is kept constant. This trend suggests that flow conditions characterized by distinct physical behaviors are better modeled using separate datasets, rather than combining them into a single snapshot matrix. Treating these regimes independently may enhance both the efficiency and accuracy of POD-based reduced-order models.

In addition to their application in POD-based reduced-order models, RBF and ANN methods are also utilized independently to construct surrogate models using the dataset presented in Figure 3.1. For the RBF-based surrogate model, predictions are made through direct interpolation of the data ensemble using the RBF method. The results from the POD-RBF ROM and the RBF-based surrogate models are found to be close to each other and to those from high-fidelity analyses, with the surrogate model yielding slightly more accurate predictions. Both approaches significantly reduce computational time compared to high-fidelity analysis. On the other hand, the surrogate model constructed using an ANN is less efficient than the POD-ANN

based ROM. The findings indicate that training the ANN-based surrogate model requires a significant amount of time, primarily due to the large number of outputs in the current case, which results in a large, complex network. By incorporating the POD method, the number of outputs is reduced, alleviating this issue. Furthermore, the results of this study show that the prediction accuracy of the POD-ANN model slightly exceeds that of the ANN-based surrogate model.

In this study, the main computational cost arises from the construction of a snapshot matrix that involves repeated high-fidelity analyses. To address this issue, LHS is employed to reduce the number of parameter pairs used to create a snapshot matrix presented in Figure 3.1. This approach is applied to the highly accurate case of RBF-based surrogate model for the aeroelastic wing, with the aim of determining whether accuracy can be maintained despite the reduction in sample size. The findings show that the LHS enables a substantial reduction in the sample size while preserving the desired level of accuracy.

In addition to the RBF and ANN models constructed in this study, simpler methods have also been employed in certain cases. Specifically, the performance of the CSI method is compared with that of an RBF model, while predictions from linear interpolation are evaluated against both POD-based RBF and ANN models under varying data densities, as well as against the RBF model using reduced datasets obtained via LHS. The results indicate that, in cases of increased data density, although the ANN gives the most accurate results; linear interpolation can sometimes yield more accurate results than the RBF model constructed in this study. However, as the number of data samples decreases, the difference in accuracy becomes more noticeable at certain points, favoring the RBF method. Nevertheless, when data reduction, computational cost or minor accuracy differences are not critical concerns, simpler interpolation methods still remain an option for addressing the type of problem examined in this study.

In conclusion, all methods proposed in this study offer significant reductions in overall computational time compared to high-fidelity analyses, making them viable

alternatives in terms of both accuracy and efficiency. The main computational expense lies in constructing the snapshot matrix, exceeding the time spent on building the reduced-order model that involves determining the optimal number of POD modes and training the ANN or evaluating the RBF. However, the initial investment in high-fidelity analyses is justified by the substantial efficiency gains achieved in subsequent modeling efforts, making it a worthwhile approach for future analyses.

6.2 Future Works

Future studies could benefit from expanding the parameter space to include additional aerodynamic conditions, structural properties, material characteristics, geometric variations, and operational environments. Such an extension would not only support the development of more optimal, adaptive, and generalizable models for aeroelastic design and analysis but also significantly broaden the scope of potential applications. Additionally, the impact of uncertainty in these variables on aeroelastic performance could be investigated.

Future studies could also investigate the use of separate datasets tailored to distinct flow regimes, especially when dealing with a wide range of Mach numbers. Grouping the data based on similar flow characteristics may enable the development of more efficient POD-based reduced-order models.

While this study focuses on static aeroelastic behavior, future research could extend the proposed ROM and surrogate modeling approaches to dynamic aeroelasticity, which involves time-dependent aerodynamic forces and structural deformations. This would allow for the analysis of dynamic responses such as flutter and other time-varying phenomena that are critical in aeroelastic design.

By extending these methods to dynamic aeroelasticity, optimization, and uncertainty quantification problems, future studies could enhance the applicability of the ROM

and surrogate modeling techniques proposed in this study, ultimately enabling more efficient aeroelastic analysis for a wide range of aerospace applications.

REFERENCES

[1] Berkooz G., Holmes P., Lumley J. L. 1993. The Proper Orthogonal Decomposition in the Analysis of Turbulent Flows, Annual Review of Fluid Mechanics, Vol.25, pp. 539-575, doi: 10.1146/annurev.fl.25.010193.002543.

[2] Amsallem D., Cortial J. and Farhat C. 2010. Toward Real-Time Computational-Fluid-Dynamics-Based Aeroelastic Computations Using a Database of Reduced-Order Information, AIAA Journal, Vol. 48-No. 9, doi: 10.2514/1.J050233.

[3] Beran P.S., Lucia D.J., Pettit C.L. 2004. Reduced-order Modelling of Limit-Cycle Oscillation for Aeroelastic Systems. Journal of Fluids and Structures, Vol. 19, pp: 575–590, doi: 10.1016/j.jfluidstructs.2004.04.002.

[4] Feng Z. and Soulaimani A. 2007. Nonlinear Aeroelasticity Modeling Using a Reduced Order Model Based on Proper Orthogonal Decomposition, ASME Pressure Vessels and Piping Division Conference, doi: 10.1115/PVP2007-26006.

[5] Xie D. and Dowell E.H. 2014. Proper Orthogonal Decomposition Reduced-Order Model for Nonlinear Aeroelastic Oscillations, AIAA Journal, Vol.52 - No.2, pp. 229-241, doi: 10.2514/1.J051989.

[6] Yao W., Marques S., Robinson T., Armstrong C., and Sun L. 2020. A Reduced-order Model for Aerodynamic Shape Optimization, Aerospace Science and Technology, doi:10.1016/j.ast.2020.106120.

[7] Wang Y., Yu B., Cao Z., Zou W., Yu G., 2012. A comparative study of POD interpolation and POD projection methods for fast and accurate prediction of heat transfer problems, International Journal of Heat and Mass Transfer 55, pp. 4827–4836, doi: 10.1016/j.ijheatmasstransfer.2012.04.053.

[8] Zimmermann R., Görtz S. 2012. Improved Extrapolation of Steady Turbulent Aerodynamics using a Non-Linear POD-Based Reduced Order Model, The Aeronautical Journal, Volume 116, Issue 1184, pp. 1079–1100, doi: 10.1017/S0001924000007491.

[9] Sinha A., Kumar R. and Umakant J. 2022. Reduced-Order Model for Efficient Generation of a Subsonic Missile's Aerodynamic Database. The Aeronautical Journal, 126, pp. 1546–1567, doi:10.1017/aer.2022.4.

[10] Hesthavena J.S., Ubbiali S. 2018. Non-intrusive Reduced Order Modeling of Nonlinear Problems Using Neural Networks. Journal of Computational Physics 363, pp. 55–78, doi: 10.1016/j.jcp.2018.02.037.

[11] San O, Maulik R, Ahmed M. 2019. An Artificial Neural Network Framework for Reduced Order Modelling of Transient Flows, Commun Nonlinear Sci Numer Simul., 77:271-287, doi:10.1016/j.cnsns.2019.04.025.

[12] Ding P., Wu X., He Y., Tao W. 2008. A Fast and Efficient Method for Predicting Fluid Flow and Heat Transfer Problems. Journal of Heat Transfer, Vol. 130, doi: 10.1115/1.2804935.

[13] Cao C., Cai J., Qu K., Li J. 2017. An Efficient Multistep ROM Method for Prediction of Flows over Airfoils. 55th AIAA Aerospace Sciences Meeting, doi:10.2514/6.2017-1421.

[14] Bui-Thanh T., Damodaran M., Willcox K. 2012. Proper Orthogonal Decomposition Extensions for Parametric Applications in Compressible Aerodynamics, 21st Applied Aerodynamics Conference, doi:10.2514/6.2003-4213.

[15] Tang L., Shyy W. 2005. Proper Orthogonal Decomposition and Response Surface Method for TPS/RLV Structural Design and Optimization: X-34 Case Study, 43rd AIAA Aerospace Sciences Meeting and Exhibit, doi: 10.2514/6.2005-839.

[16] Taeibi-Rahni M., Sabetghadam F. and Moayyedi M. K. 2010. Low-Dimensional Proper Orthogonal Decomposition Modeling as a Fast Approach of Aerodynamic Data Estimation. Journal of Aerospace Engineering, pp.44-54, doi:10.1061/(ASCE)0893-1321(2010)23:1(44).

[17] Malouin B., Trepanier J. and Gariepy M. 2013. Interpolation of Transonic Flows Using a Proper Orthogonal Decomposition Method, International Journal of Aerospace Engineering, doi: 10.1155/2013/928904.

[18] Mifsud M. J., Shaw S. T. and MacManus D. G. 2010. A High-fidelity Low-Cost Aerodynamic Model Using Proper Orthogonal Decomposition. International Journal for Numerical Methods in Fluids, 63:468-494, doi:10.1002/fld.2085.

[19] Coelho R. F., Breitkopf P., Knopf-Lenoir C., Villon P. 2009. Bi-level Model Reduction for Coupled Problems: Application to a 3D Wing, Struct Multidisc Optim, 39:401–418, doi:10.1007/s00158-008-0335-3.

[20] Xiao D., Yanga P., Fang F., Xiang J., Pain C.C., Navon I.M. 2016. Non-Intrusive Reduced Order Modelling of Fluid–Structure Interactions, Comput. Methods Appl. Mech. Engrg. 303, pp:35–54, doi: 10.1016/j.cma.2015.12.029.

[21] Li K., Huang T., Li L., Lanteri S. 2021. Non-Intrusive Reduced-Order Modeling of Parameterized Electromagnetic Scattering Problems using Cubic Spline Interpolation, Journal of Scientific Computing, 87:52, doi:10.1007/s10915-021-01467-2.

[22] Fossati M. and Habashi W. G. 2013. Multiparameter Analysis of Aero-Icing Problems Using Proper Orthogonal Decomposition and Multidimensional Interpolation. AIAA Journal, Vol. 51, No. 4., doi:10.2514/1.J051877.

[23] Yasong Q., Junqiang B. 2015. Stationary Flow Fields Prediction of Variable Physical Domain Based on Proper Orthogonal Decomposition and Kriging Surrogate Model. Chinese Journal of Aeronautics, 28(1): 44–56,doi: 10.1016/j.cja.2014.12.017

[24] Mohammadi A. and Raisee M. 2019. Stochastic Field Representation Using Bi-Fidelity Combination of Proper Orthogonal Decomposition and Kriging. Comput. Methods Appl. Mech. Engrg, 357, doi: 10.1016/j.cma.2019.112589.

[25] Bhattacharyya B. 2022. Uncertainty Quantification of Dynamical Systems by a POD–Kriging Surrogate Model. Journal of Computational Science, 60(2):101602, doi: 10.1016/j.jocs.2022.101602.

[26] Walton S., Hassan O., Morgan K. 2013.Reduced Order Modelling for Unsteady Fluid Flow Using Proper Orthogonal Decomposition and Radial Basis Functions Applied Mathematical Modelling, 8930–8945, doi:10.1016/j.apm.2013.04.025

[27] Wang X., Wang Y., Cao Z., Zou W., Wang L., Yu G., Yu B., Zhang J. 2013. Comparison Study on Linear Interpolation and Cubic B-Spline Interpolation Proper Orthogonal Decomposition Methods. Advances in Mechanical Engineering, doi:10.1155/2013/561875.

[28] Sun X., Pan X., Choi J. 2021. Non-intrusive Framework of Reduced-Order Modeling Based on Proper Orthogonal Decomposition and Polynomial Chaos Expansion. Journal of Computational and Applied Mathematics, 390-113372, doi: 10.1016/j.cam.2020.113372.

[29] Hua J. and Sørheim E.A. 2022. Nonintrusive Reduced-Order Modeling Approach for Parametrized Unsteady Flow and Heat Transfer Problems. Int J Numer Meth Fluids. 94:976–1000, doi: 10.1002/fld.5080.

[30] Xiao D., Fang F., Pain C., Hu G. 2015. Non-intrusive Reduced-Order Modelling of The Navier–Stokes Equations Based on RBF Interpolation. International Journal for Numerical Methods in Fluids, 79:580–595, doi: 10.1002/fld.4066.

[31] Fornberg, B., Flyer, N. 2005. Accuracy of Radial Basis Function Interpolation and Derivative Approximations On 1-D Infinite Grids, Adv Comput Math 23, pp: 5–20, doi: 10.1007/s10444-004-1812-x.

[32] Sun G., Li G., Gong Z., He G., Li Q. 2011. Radial Basis Functional Model for Multi-Objective Sheet Metal Forming Optimization Engineering Optimization, 43:12, pp:1351-1366, doi: 10.1080/0305215X.2011.557072.

[33] Li X., Gao W., Gu L., Gong C., Jing Z., Su H. 2017. A Cooperative Radial Basis Function Method for Variable-Fidelity Surrogate Modeling, Struct Multidisc Optim, 56:1077–1092, doi: 10.1007/s00158-017-1704-6.

[34] Song X., Lv L., Sun W., Zhang J. 2019. A Radial Basis Function-Based Multi-Fidelity Surrogate Model: Exploring Correlation Between High-Fidelity and Low-Fidelity Models, Structural and Multidisciplinary Optimization, 60:965–981, doi: 10.1007/s00158-019-02248-0.

[35] Ribeiro L. G., Maia M. A., Parente Jr E., de Melo A.M.C. 2020. Surrogate Based Optimization of Functionally Graded Plates Using Radial Basis Functions. Composite Structures 252, 112677 doi: 10.1016/j.compstruct.2020.112677.

[36] Yamanaka Y., Matsubara S., Hirayama N., Moriguchi S. and Terada K. 2023. Surrogate modeling for the homogenization of elastoplastic composites based on RBF interpolation, Comput. Methods Appl. Mech. Engrg. 415, 116282 doi: 10.1016/j.cma.2023.116282.

[37] Gong Y., Gao C. and Zhang W. 2024. Transonic Buffet Suppression by Airfoil Optimization, Aerospace, 11, 121. doi: 10.3390/aerospace11020121.

[38] Oh S. 2020. Comparison of a Response Surface Method and Artificial Neural Network in Predicting the Aerodynamic Performance of a Wind Turbine Airfoil and Its Optimization, Appl. Sci., 10, 6277. doi:10.3390/app1018627.

[39] Schroder L., Dimitrov N. K., Sorensen J.A. 2020. Uncertainty propagation and sensitivity analysis of an artificial neural network used as wind turbine load surrogate model, Journal of Physics: Conference Series, 042040 doi:10.1088/1742-6596/1618/4/042040.

[40] Schweidtmann A.M., Huster W. R., Lüthje J. T. and Mitsos A. 2019. Deterministic global process optimization: Accurate (single-species) Properties via Artificial Neural Networks, Computers and Chemical Engineering 121, 67–74 doi: 10.1016/j.compchemeng.2018.10.007.

[41] Wang Q., Hesthaven J. S., Ray D. 2019. Non-Intrusive Reduced Order Modeling of Unsteady Flows Using Artificial Neural Networks with Application to a Combustion Problem, Journal of Computational Physics 384(2019)289–307.

[42] Sun Z., Wang C., Zhengb Y., Bai J., Li Z., Xia Q., Fu Q. 2020. Non-Intrusive Reduced-Order Model for Predicting Transonic Flow with Varying Geometries, Chinese Journal of Aeronautics, 33(2): 508–519.

[43] Şugar-Gabor O. 2021. Parameterized Nonintrusive Reduced-Order Model for General Unsteady Flow Problems Using Artificial Neural Networks, Int J Numer Meth Fluids, 93:1309–1331, doi: 10.1002/fld.4930.

[44] Yu J., Hesthaven J. S. 2019. Flowfield Reconstruction Method Using Artificial Neural Network, AIAA Journal, Vol. 57, No. 2, pp:1-17, doi: 10.2514/1.J057108.

[45] Renganathan SA, Maulik R. and Rao V. 2020. Machine Learning for Nonintrusive Model Order Reduction of the Parametric Inviscid Transonic Flow Past an Airfoil. Phys Fluids, 32(4):047110, doi:10.1063/1.5144661.

[46] Lindhorst K., Haupt M. C. and Horst P. 2014. Efficient Surrogate Modelling of Nonlinear Aerodynamics in Aerostructural Coupling Schemes, AIAA Journal, Vol. 52, No. 9, doi: 10.2514/1.J052725.

[47] Lindhorst K., Haupt M. C. and Horst P. 2016. Reduced-Order Modeling of Non-Linear, Transient Aerodynamics of the HIRENASD wing, The Aeronautical Journal, Volume 120, No 1226, doi: 10.1017/aer.2016.12.

[48] Ripepi M., Verveld M. J., Karcher N. W., Franz T., Abu-Zurayk M., Görtz S., Kier T. M. 2018. Reduced-order Models for Aerodynamic Applications, Loads and MDO, CEAS Aeronautical Journal 9:171–193, doi:10.1007/s13272-018-0283-6.

[49] Kafkas A. and Lampeas G. 2020. Static Aeroelasticity Using High Fidelity Aerodynamics in a Staggered Coupled and ROM Scheme, Aerospace 2020, 7, 164, doi:10.3390/aerospace7110164.

[50] Changchuan X., Chao A, Yi L., Chao Y. 2017. Static Aeroelastic Analysis Including Geometric Nonlinearities Based on Reduced Order Model, Chinese Journal of Aeronautics, 30(2): 638–650, doi: 10.1016/j.cja.2016.12.031.

[51] G. Berthelin, S.Dubreuil, M.Salaün, N.Bartoli, C. Gogu. 2022. Disciplinary Proper Orthogonal Decomposition and Interpolation for the Resolution of Parameterized Multidisciplinary Analysis, Int J Numer Methods Eng. 2022;123:3594–3626, doi:10.1002/nme.6981.

[52] ANSYS Inc. Ansys® Fluent, 2021, Release 21.2. Available online: https://www.ansys.com/

[53] ANSYS Inc. Ansys® Mechanical, 2021, Release 21.2. Available online: https://www.ansys.com/

[54] Ansys® Inc. System Coupling User's Guide, Release 20.1

[55] Yates E.C. 1995. AGARD Standard Aeroelastic Configurations for Dynamic Response, AGARD Report No .765. Meeting of the Structures and Materials Panel at Oberammergau, Germany; September 8 -13.

[56] Cai J., Liu F., Tsai H.M., Wong A.S.F. 2001. Static Aeroelastic Computation with a Coupled CFD and CSD Method, AIAA 2001-0717, Aerospace Sciences Meeting and Exhibit, 39th Reno NV, Jan. 8-11, doi: 10.2514/6.2001-717

[57] Kolonay R. M. 1996. Unsteady aeroelastic optimization in the transonic regime, Ph. D. Thesis, Purdue University.

[58] McKay, M.D., Beckman, R.J., Conover, W.J. 1979. A Comparison of Three Methods for Selecting Values of Input Variables in the Analysis of Output from a Computer Code. Technometrics, 21, 239–245, doi:10.2307/1268522

[59] Beale M. H., Hagan M.T., Demuth H. B., Neural Network Toolbox™ User's Guide, R2017b.

[60] Marquardt, D. 1963. An Algorithm for Least-Squares Estimation of Nonlinear Parameters, Journal on Applied Mathematics, Vol. 11, No. 2, pp. 431–441.

[61] Hagan M.T., Demuth H. B., Beale M. H. 1996. Neural Network Design, Boston, MA: PWS Publishing.

[62] Møller M.F. 1993. A Scaled Conjugate Gradient Algorithm for Fast Supervised Learning, Neural Networks, Vol. 6, pp.525-533, doi:10.1016/S0893-6080(05)80056-5

APPENDICES

A. Mesh Sensitivity for Structural Analysis

To demonstrate the mesh independence of the results in terms of structural analysis accuracy, the modal analysis outcomes are compared across different mesh densities. For this reason, the wing structure is analyzed using different mesh sizes, as shown in Figure A.1.

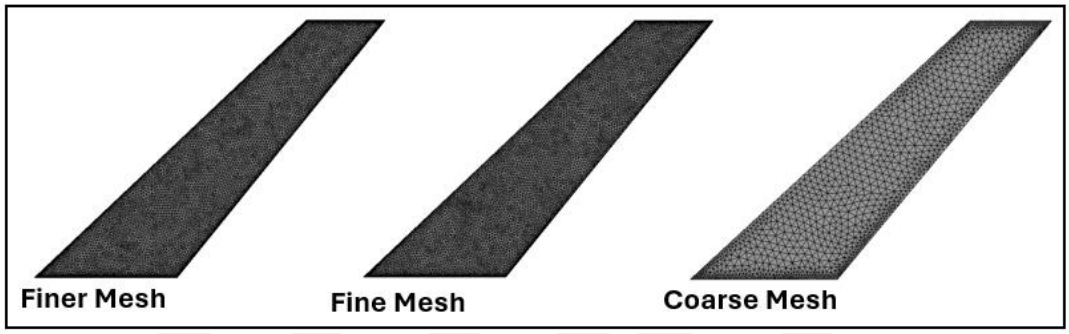

Figure A.1. The wing model with different structural mesh sizes

The number of nodes and elements corresponding to those meshes are given in Table A.1.

Table A.1. Number of nodes and elements for different mesh cases

	Finer Mesh	**Fine Mesh**	**Coarse Mesh**
Number of Nodes	217154	171702	17300
Number of Elements	130500	101288	8562

The comparison of the modal frequencies for these different mesh cases is given in Table A.2.

Table A.2. Comparison of modal frequencies for different mesh cases

	Finer Mesh	**Fine Mesh**	**Coarse Mesh**
1st Bending Mode	5.894	5.894	5.898
1st Torsion Mode	25.606	25.607	25.635
2nd Bending Mode	36.749	36.753	36.823
2nd Torsion Mode	62.416	62.420	62.520

The results indicate that the outcomes for all three mesh cases are very similar. By reviewing the structural analysis results, it can be concluded that the coarser mesh would have also yielded highly accurate results. However, using a coarse mesh leads to convergence issues during the two-way analysis. To avoid these convergence problems in the fluid-structural coupling, the fine mesh is adopted. When compared to the results obtained from a finer mesh than the current one (fine mesh), it is evident that the current mesh is sufficient for achieving accurate results.

B. NRMSE Distribution for Different Mode Numbers

The NRMSE distribution for all 63 data pairs is given in Figure B.1 for Cp results of the rigid wing.

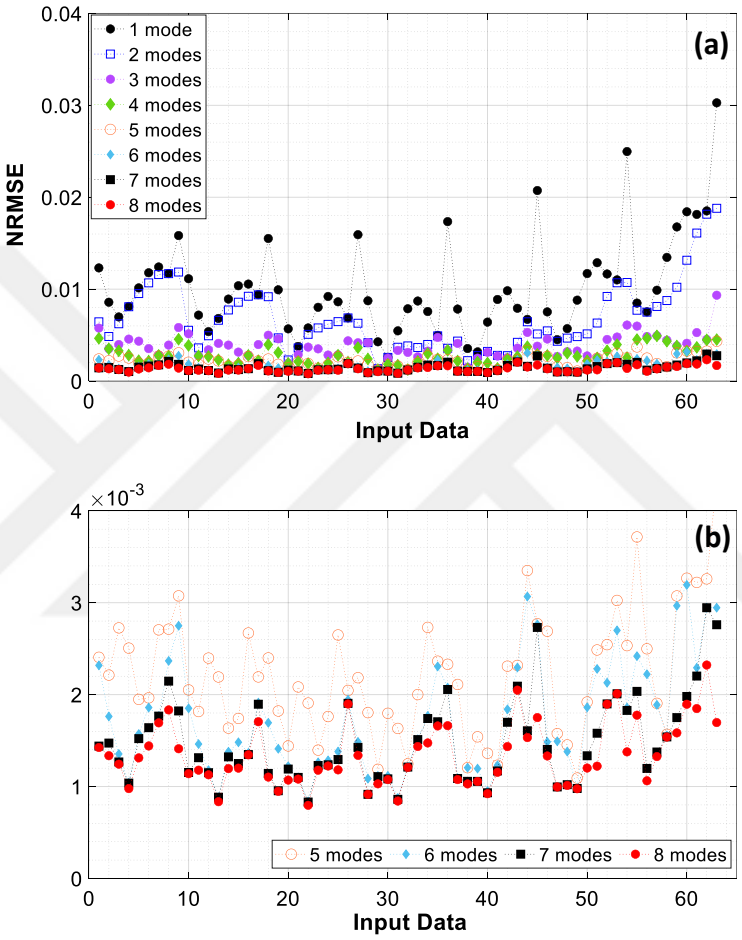

Figure B.1. NRMSE distribution of Cp results for different mode numbers (a) and the detailed view for higher mode numbers (b) for each parameter pair of the rigid wing

It is observed that the results for the 8 modes exhibit the smallest NRMSE values, as expected. With 8 modes, 90% of the energy is captured as explained in Section 3.2.1.

Similarly, the NRMSE distribution for each data pair is given in Figure B.2 for Cp results of the aeroelastic wing.

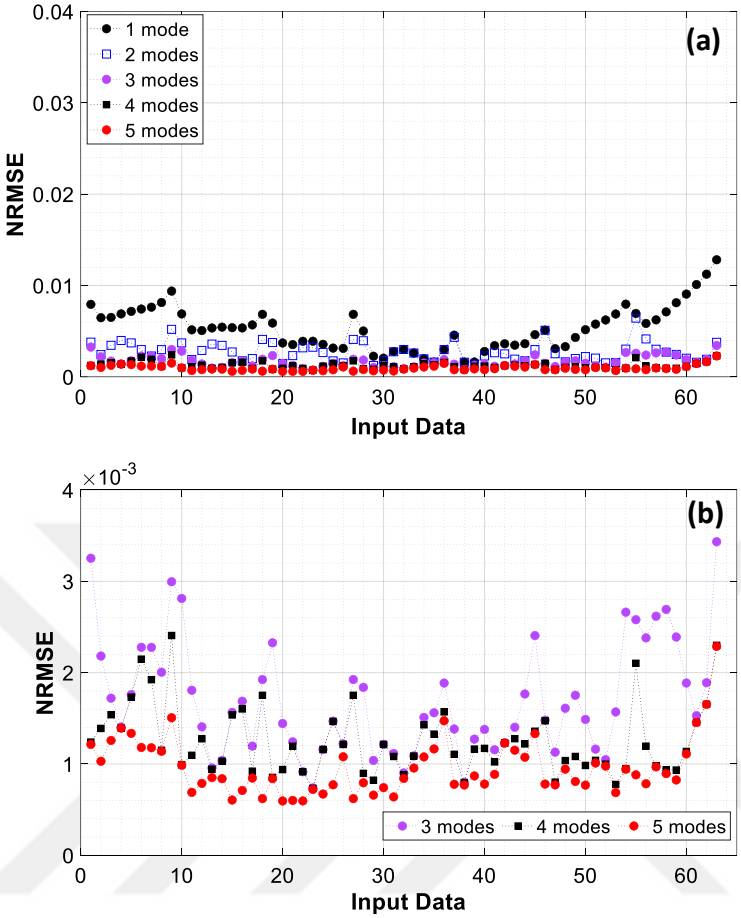

Figure B.2. NRMSE distribution of Cp results for different mode numbers (a) and the detailed view for higher mode numbers (b) for each parameter pair of the aeroelastic wing

It is seen that the results for the 5 modes exhibit the smallest NRMSE values of the Cp results of the aeroelastic wing, as expected. With 5 modes, 90% of the energy can be captured, as explained in Section 3.2.2.

In Section 3.2.2., separate snapshot matrices are constructed for the x, y, z coordinates of the nodes. The logarithmic plots displaying the fraction of energy corresponding to the x, y and z positions of the nodes are presented in Figure B.3.

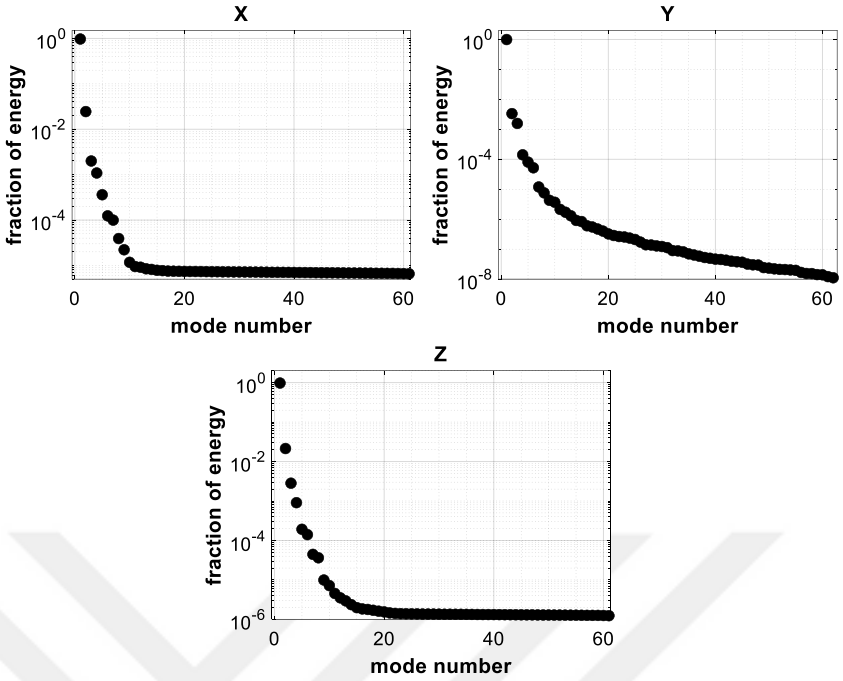

Figure B.3. Logarithmic plots of the energy fraction for the x, y, z positions of the nodes

C. Mesh Refinement Study for Higher Mach Conditions

In this part, the results obtained using the current mesh are compared with those from a finer mesh. For this reason, the overall mesh density on the wing surface is increased (Figure C.1). The chord locations at 0.55 m and 0.8 m span are highlighted in red in Figure C.1.

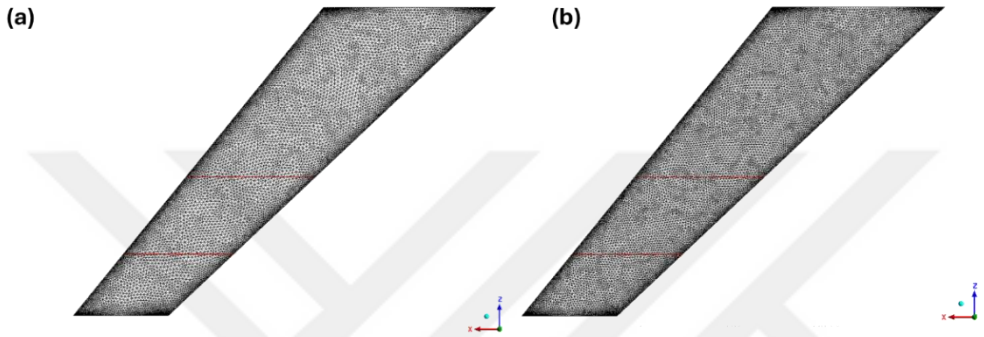

Figure C.1. Current mesh with 20366 nodes(a) and finer mesh with 23679 nodes(b)

The Cp distribution on the wing for these 2 mesh cases are given in Figure C.2 for a flow condition of M= 0.95 and AOA = 5°.

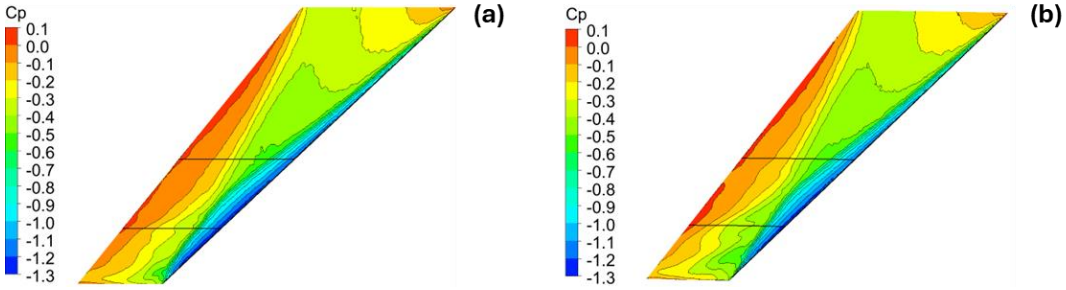

Figure C.2. Cp distribution on the wing for current mesh (a) and finer mesh (b) for a flow condition of M= 0.95 and AOA = 5°

In addition, the chordwise Cp distributions at 0.8 m and 0.55 m span locations are compared in Figure C.3 for different mesh sizes.

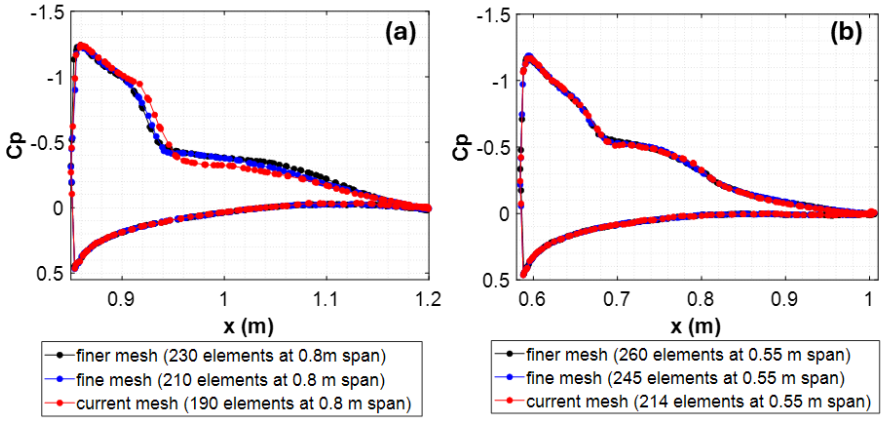

Figure C.3. Chordwise Cp distribution at 0.8 m (a) and 0.55m span locations (b) on the wing for different mesh sizes (M= 0.95 and AOA = 5°)

In Figure C.3(b), the results of the current mesh are indicated with red markers, while the results from the finer mesh are represented with black markers. Additionally, an intermediate mesh size has been included for comparison and is depicted using dark blue markers.

The variation of Mach number is also given in Figure C.4 for the 2 mesh cases shown in Figure C.1.

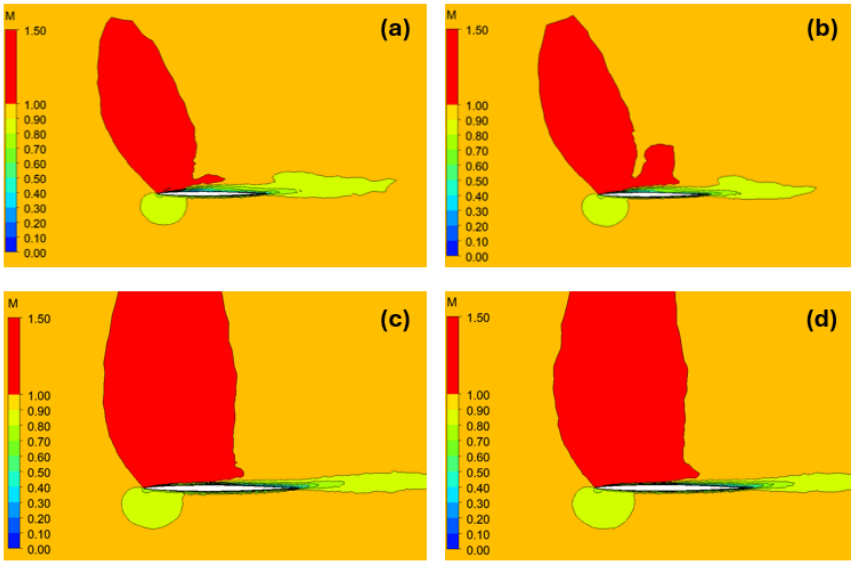

Figure C.4. Variation of Mach number at 0.8 m span location of the wing for the current mesh (a) and finer mesh (b), variation of Mach number at 0.55 m span location of the wing for the current mesh (c) and finer mesh (d).

The results presented in Figure C.2, Figure C.3 and Figure C.4 indicate that the current mesh yields outcomes that differ slightly from those obtained using finer mesh, especially at locations close to the wing tip. This suggests that, for transonic flow cases, where highly nonlinear flow behavior is present, the mesh configuration must be designed accordingly to ensure greater accuracy. In this study, however, the snapshot matrix is built from data collected at individual nodes, necessitating a consistent number of nodes across varying flow conditions. Consequently, the same mesh is used for higher Mach numbers, as the observed differences remain within an acceptable range.

D. Flow Conditions where Shock Formation is Observed

Flow conditions with higher Mach numbers are added to the dataset presented in Figure 3.1, some of which results in a formation of shock waves on the wing. In Table D.1, the conditions where shock waves are observed are marked with a '+'.

Table D.1. Flow conditions where shock formation is observed

AOA \ M	0,96	0,95	0,94	0,93	0,92	0,91	0,9
5	+	+	+	+	-	-	-
4,5	+	+	+	+	-	-	-
4	+	+	+	+	-	-	-
3,5	+	+	+	-	-	-	-
3	+	+	+	-	-	-	-
2,5	+	+	-	-	-	-	-
2	+	+	-	-	-	-	-
1,5	+	-	-	-	-	-	-
1	+	-	-	-	-	-	-

Figure D.1 shows the flow condition at Mach number = 0.85 and AOA = 5° where no shock is observed, serving as a reference for comparison.

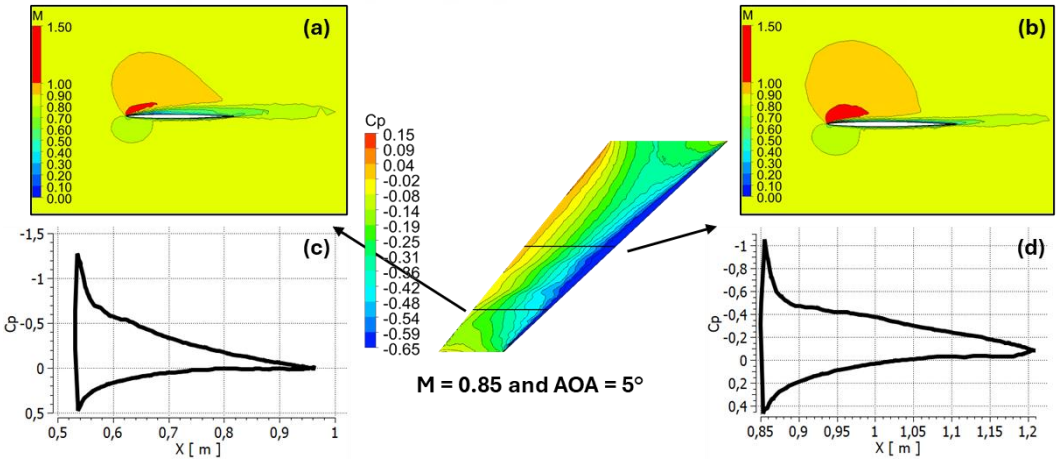

Figure D.1. Variation of Mach number at 0.8 m (a) and 0.5 m (b); chordwise Cp distribution at 0.8 m (c) and 0.5 m (d) span locations for M=0.85 and AOA= 5° flow condition

As seen in Figure D.1, there is no sharp drop in Mach number or discontinuity in the Cp distributions, in contrast to the flow condition of M=0.95 and AOA=5° illustrated in Figure 3.24 and Figure 3.25.

Additionally, a sample flow condition at M=0.93 and AOA=4.5°, where a shock is observed, is also presented in Figure D.2. The chordwise section taken at a spanwise location of 0.45 m span (where shock formation is more pronounced) illustrates how the Mach number varies along the chord. Furthermore, the corresponding Cp distribution at the same location highlights the discontinuity, indicating the presence of shock.

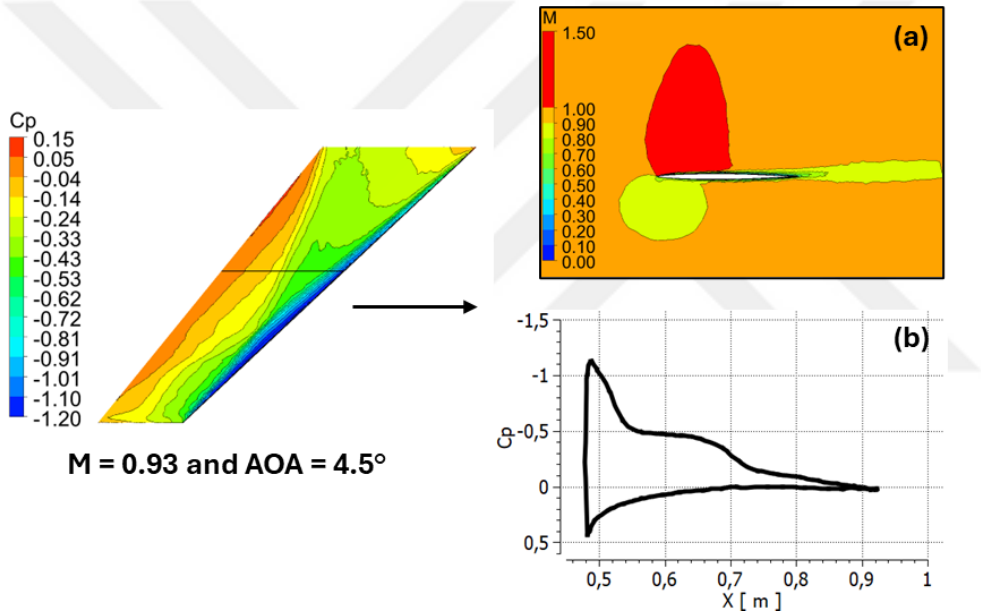

Figure D.2. Variation of Mach number at 0.5 span location (a), chordwise Cp distribution at 0.5 span location (b) for M=0.95 and AOA= 2° flow condition

The flow conditions marked with a '+' in Table D.1 exhibit similar behavior consistent with shock formation, although the shock strength varies, some being relatively weak, while others are more pronounced.

E. Accumulated Energy and NRMSE Distribution of the Reconstructed Cp for Each Data Pair with Different Data Sizes

Figure E.1 presents the accumulated energy and the NRMSE distribution across 90 parameter points for the Cp values of the rigid wing using 17 POD modes and Figure E.2 presents the corresponding results for the aeroelastic wing using 10 POD modes.

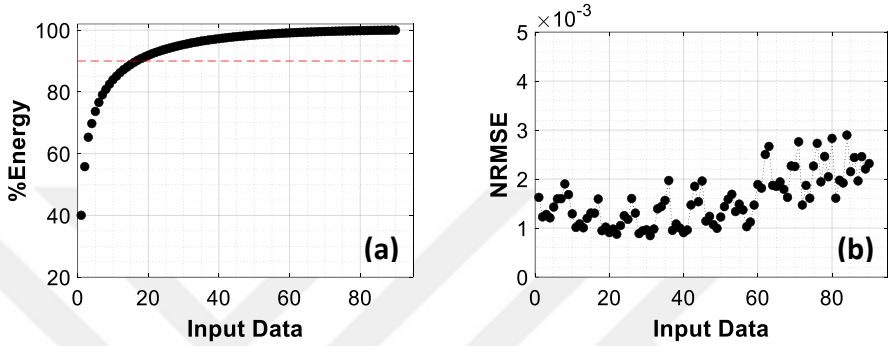

Figure E.1. Accumulated energy for the Cp of the rigid wing (a) and NRMSE distribution for the reconstructed Cp of the rigid wing for each 90 data pairs (b)

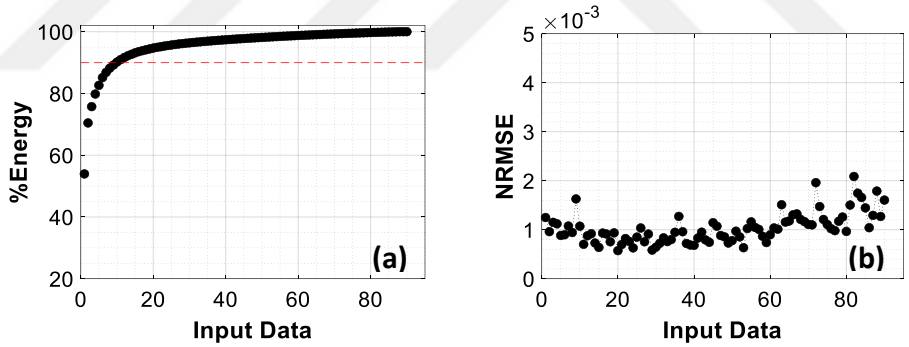

Figure E.2. Accumulated energy for the Cp of the aeroelastic wing (a) and NRMSE distribution for the reconstructed Cp of the aeroelastic wing for each 90 data pairs (b)

Figure E.3 presents the accumulated energy and the NRMSE distribution across 126 parameter points for the Cp values of the rigid wing, obtained using 24 POD modes.

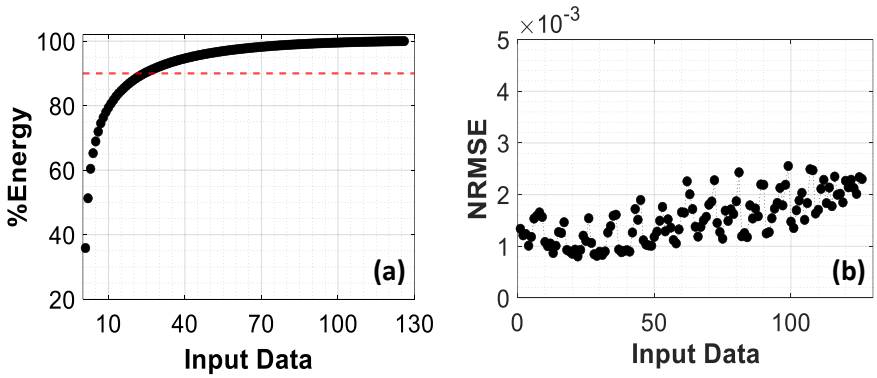

Figure E.3 Accumulated energy for the Cp of the rigid wing (a) and NRMSE distribution for the reconstructed Cp of the rigid wing for each 126 data pairs (b)

F. NRMSE Distribution of the Surrogate Model using Cubic Spline Interpolation Method

A simple regression method of cubic spline interpolation is also employed to construct a surrogate model using the dataset given in Figure 3.1, by implementing it on the snapshot matrix of the rigid wing's Cp results. In cubic spline interpolation, a cubic polynomial is used to interpolate data between adjacent grid points in each respective dimension. This method has been widely used in various studies, often yielding highly accurate results, as mentioned in Chapter 1. The NRMSE results for the Cp distributions of the intermediate parameters are given in Figure F.1.

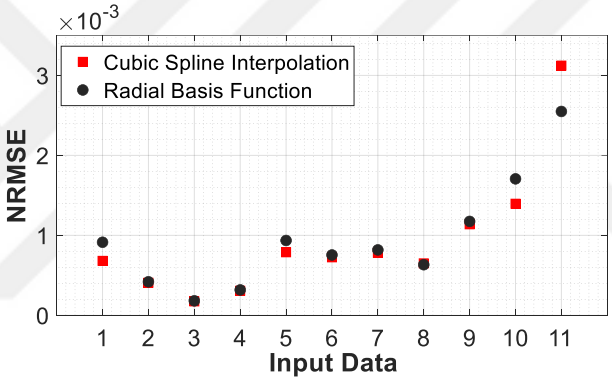

Figure F.1. NRMSE distribution of Cp results of rigid wing using cubic spline interpolation and RBF methods

It is seen in Figure F.1 that cubic spline interpolation provides more accurate results for most points compared to the RBF approach discussed in this study. However, for the last intermediate point, corresponding to the highest AOA and M pair, the RBF method stands out with the highest accuracy difference. Nonetheless, it can be inferred that for cases exhibiting limited nonlinearity, such as the data range presented in Figure 3.1, a simpler regression model could also yield satisfactory accuracy.

G. Prediction Performance of the RBF and Linear Interpolation Methods for the Reduced Parameter Sizes Obtained from LHS

Instead of using uniform sampling, data points can be selected within the interval using LHS method. The reduced samples, using LHS method, along with the prediction points are illustrated in Figure 4.13. For such cases involving scattered data in two dimensions, Matlab's 'scatteredInterpolant' function can be used for interpolation. The method works by dividing the data domain into a set of non-overlapping triangles formed by the available data points. For each prediction point that lies within one of these triangles, the interpolated value is calculated as a linear combination of the values at the triangle's vertices. For the aeroelastic wing configuration, the results obtained using RBF and linear interpolation methods are presented in Figure G.4. for 30, 15 and 7 LHS samples.

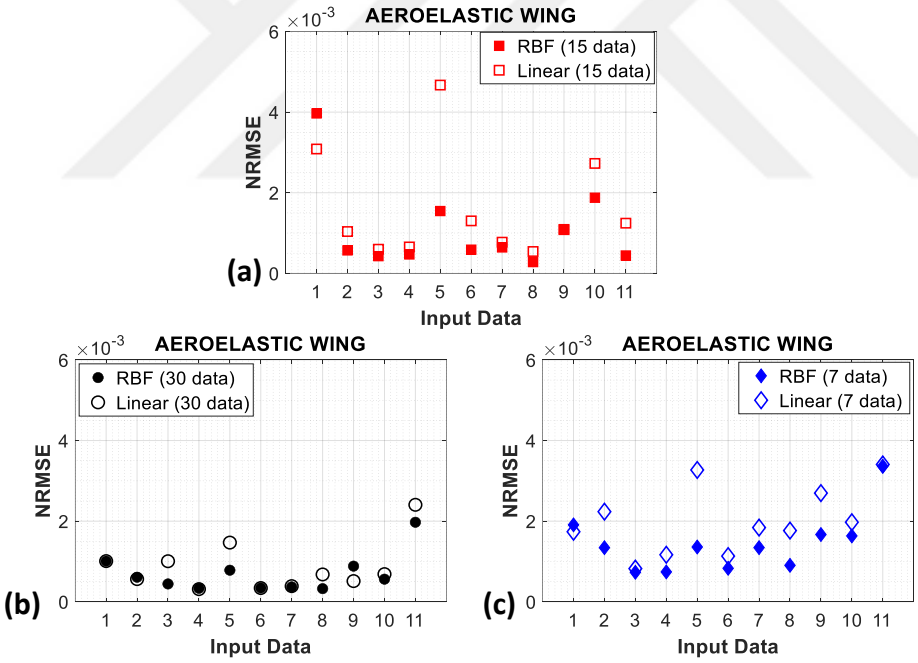

Figure G.4. NRMSE distribution of aeroelastic Cp results obtained by using the RBF and linear interpolations for 15 (a), 30 (b) and 7 (c) LHS data

Except for one prediction point in all LHS cases, RBF interpolation consistently yields more accurate results. This is particularly evident at the 5th prediction point,

where the difference between the two methods is significant, especially in the case with 15 samples. This discrepancy arises because when a prediction point lies outside the set of triangles defined by the data, its value is estimated based on the values and local gradients at the nearest boundary of the data domain. While this allows the method to return a value even outside the data region, the accuracy of such extrapolated results may be lower and less reliable compared to those obtained within the interior of the data domain. Similarly, the results obtained using RBF and linear interpolations for the rigid wing configuration are presented in Figure G.5 for 30, 15 and 7 LHS samples.

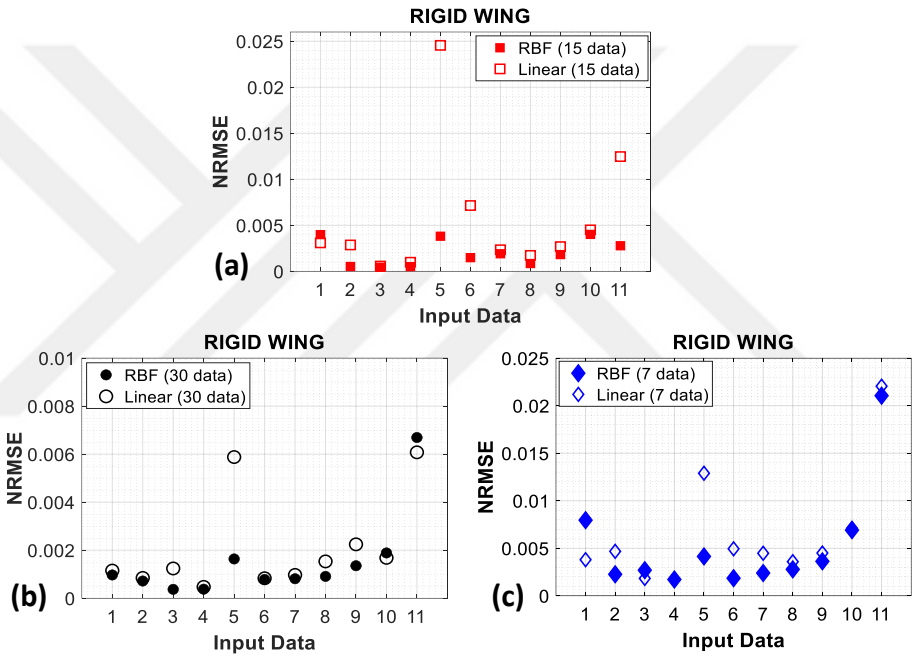

Figure G.5. NRMSE distribution of rigid Cp results obtained by using the RBF and linear interpolations for 15 (a), 30 (b) and 7 (c) LHS data

For the rigid wing configuration, the overall accuracy is lower than that of the aeroelastic wing, particularly in the case with 7 LHS samples. In the 15- and 30-sample cases, as with the aeroelastic wing, the difference between the interpolation results at the 5th prediction point remains significant. Moreover, in the 15-sample case, the discrepancies become even more pronounced at specific points, such as points 5, 6, and 11, compared to the aeroelastic configuration. Therefore, RBF interpolation may be preferred in these instances due to its higher accuracy.

H. NRMSE Distribution of ANN Models with Different Number of Layers and Neurons

As explained in Chapter 5, in Matlab's artificial neural networks tool, dataset is divided into training, validation and test subsets. By default, 70% of the data is allocated for training, while 15% each is designated for validation and testing. The validation set is used during training to evaluate the model's performance, helping to assess how well it generalizes to new, unseen data and preventing overfitting to the training set. On the other hand, the test set is reserved for evaluating the final model's performance and is not used during the training or validation phases. For this study, the ANN models are constructed through several trials while maintaining these default percentages. However, to avoid reducing the dataset that is already comparatively small, the test set is excluded in this part. The intermediate data points given in Figure 4.1, other than the dataset, are used for the test purpose. In addition, the percentage of validation points is reduced to 5%, similarly, to preserve the total number of the training data as high as possible and increase accuracy.

In this case of higher number of training points, different configurations of neurons and layers are tested to determine whether the accuracy of the Cp results for the rigid wing configuration discussed in Section 5.2.1 can be improved. The NRMSE distribution for the predicted Cp results of the 11 intermediate points (which also serve as test points) is given in Figure H.1, showing the case with 1 layer and varying numbers of neurons.

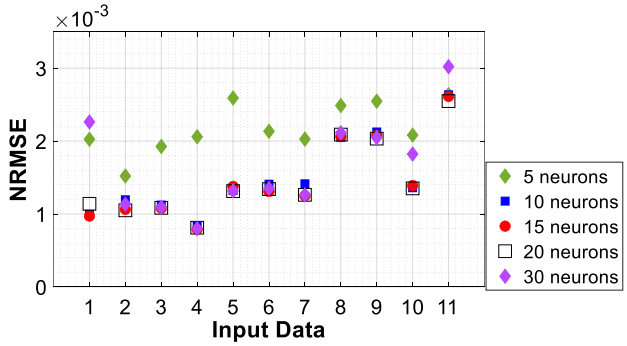

Figure H.1. NRMSE distribution of Cp results of the rigid wing with different number of neurons

In this case, it is observed that the most accurate results for most points are obtained with 1 layer with 15 neurons. The output vs target plots for training and validation points for this ANN configuration are given in Figure H.2.

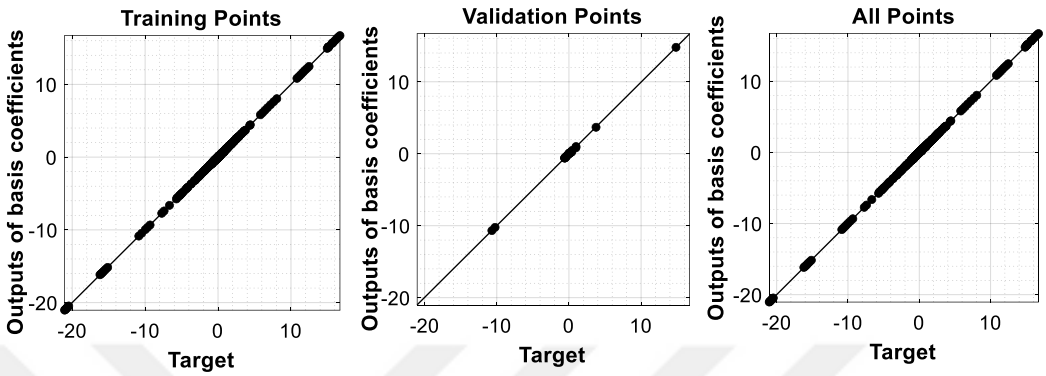

Figure H.2. Output vs target plots of basis coefficients for the ANN with 15 neurons

Similarly, the NRMSE distribution for the predicted Cp results of the intermediate points with different number of layers and neurons is given in Figure G.3.

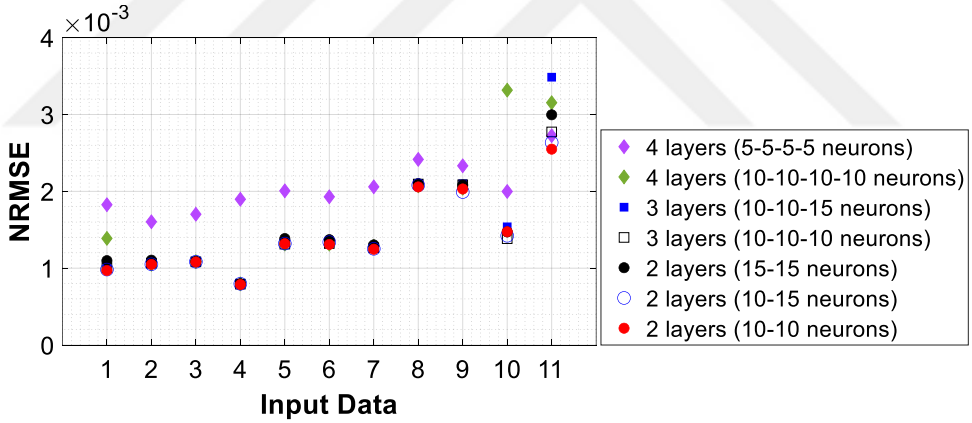

Figure H.3. NRMSE distribution of Cp results of the rigid wing with different number of layers and neurons

It is seen in Figure H.3 that the most accurate results for most points are obtained with 2 layers, each containing 10 neurons. The output vs target plots for training and validation points for this ANN configuration are given in Figure H.4.

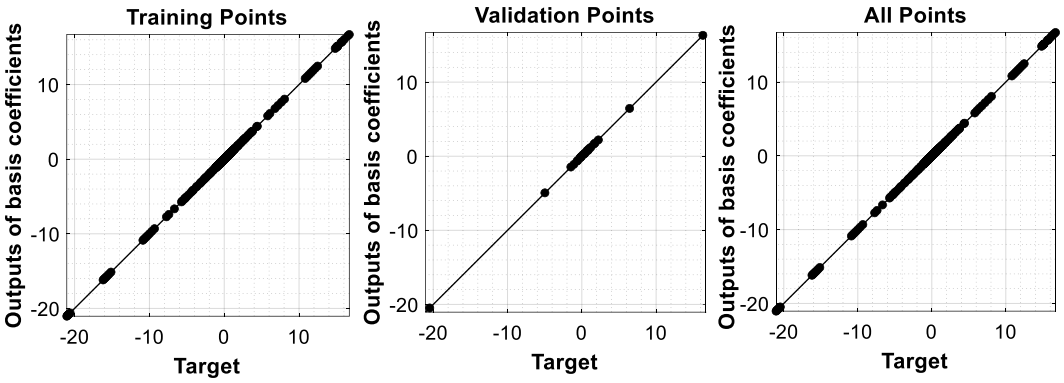

Figure H.4. Output vs target plots of basis coefficients for the ANN with 2 layers with 10 neurons each

Both configurations with 1 layer with 15 neurons as well as 2 layers, each containing 10 neurons, give the most accurate results being close to each other. In Figure H.5, the NRMSE results are compared with each other as well as the results given in Chapter 5.

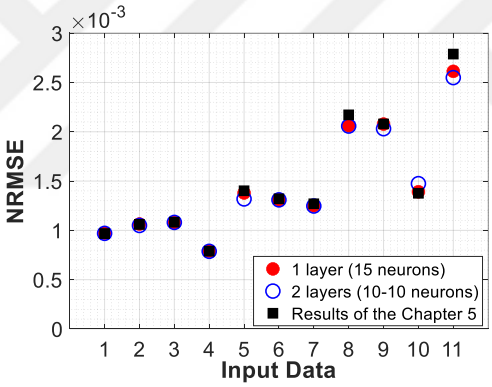

Figure H.5. NRMSE distribution of Cp results of rigid wing with different ANN configurations

It is seen that although the results are close to each other for most of the flow conditions, there is a noticeable difference between the results from Chapter 5 and the current results for the last prediction point, which has the highest M and AOA pair. In the current case, the ANN configuration with 2 layers, each containing 10 neurons, provides the most accurate results. On the other hand, in Chapter 5, the most accurate results were obtained using a single-layer ANN containing 15 neurons and adopting the Matlab's default dataset partitioning scheme, which allocates 70% of the data for training, while 15% each for validation and testing.

I. ANN Configurations with Different Number of Layers and Neurons

The following plots illustrate the output versus target comparisons for the most accurate ANN configurations used to predict Cp results. Figure I.1 shows the results for the ANN configuration with 2 hidden layers containing 10 and 20 neurons, respectively, developed for the Cp prediction of the rigid wing using the POD-based ROM with 90 data samples. Figure I.2 presents the results for the ANN with 2 layers of 15 and 20 neurons constructed for the Cp prediction of the aeroelastic wing using the corresponding POD-based ROM with 90 data samples. Finally, Figure I.3 displays the results for the ANN with 3 layers consisting of 10, 15 and 25 neurons developed for the rigid wing case using the POD-based ROM with 126 data samples.

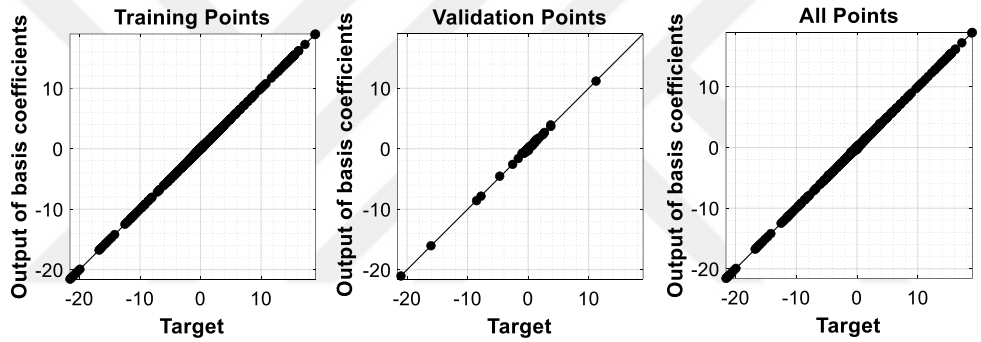

Figure I.1. Output vs target plot for ANN containing 2 layers with 10 and 20 neurons constructed for the Cp results of the rigid wing (90 data case)

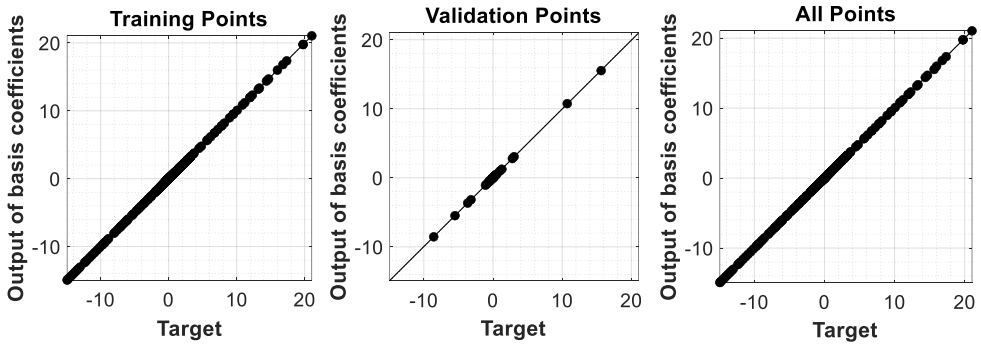

Figure I.2. Output vs target plot for ANN with 2 layers and 15 and 20 neurons constructed for the Cp results of the aeroelastic wing (90 data case)

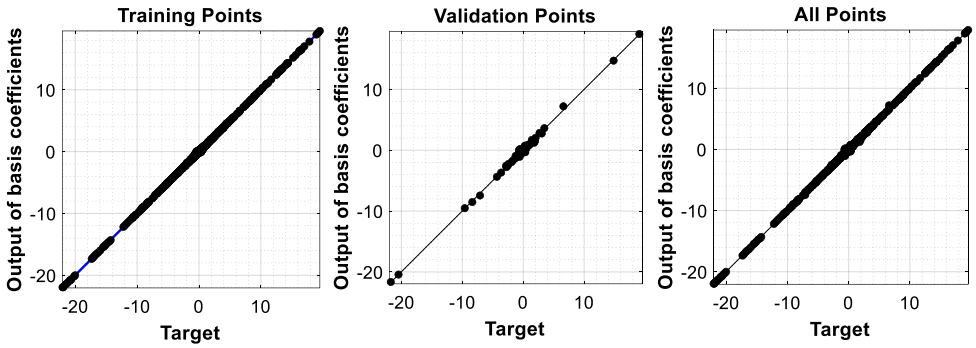

Figure I.3. Output vs. target plots of basis coefficients for the ANN with 3 layers and 10,15 and 25 neurons (126 data case)

The plots demonstrate a great match between the predicted and actual values for both the training and validation datasets, indicating the effectiveness of the respective ANN configurations. The NRMSE distributions for various other ANN configurations are presented in the following plots at various prediction points. These ANN configurations represent the most accurate models obtained across numerous trial runs. Figure I.4 displays the results for different ANN configurations, featuring different number of layers and neurons, used to predict the Cp values of the rigid wing, based on the POD-based ROM with 90 data samples. Figure I.5 shows the corresponding results for the aeroelastic wing case, also using a POD-based ROM and 90 data samples. Finally, Figure I.6 presents the results for different ANN configurations developed for the Cp prediction of a rigid wing, utilizing a POD-based ROM with 126 data samples.

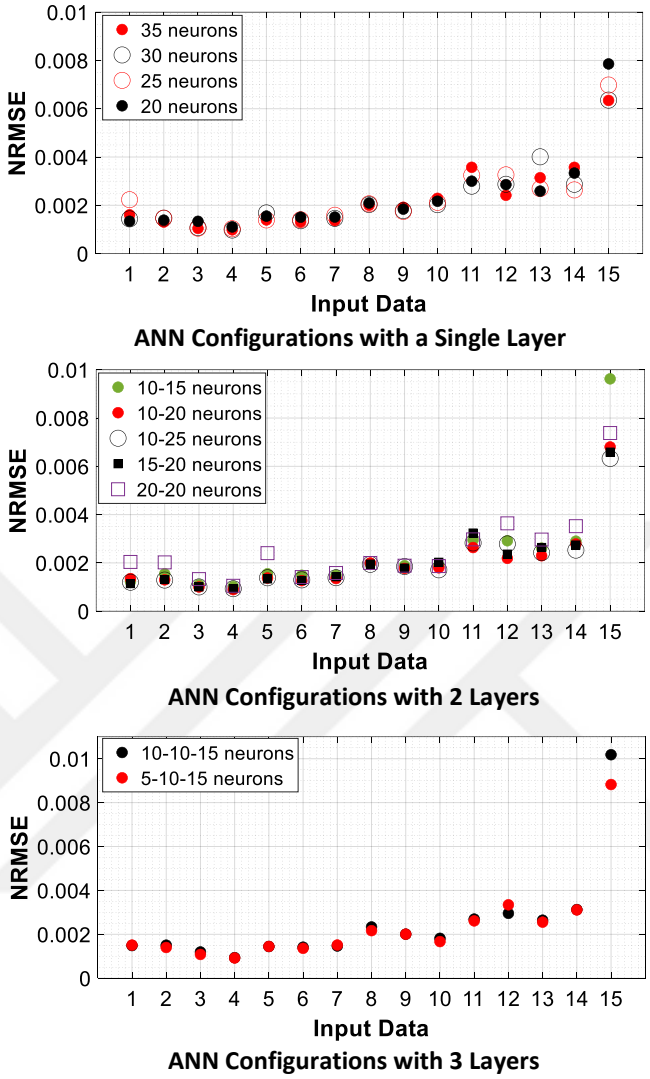

Figure I.4. NRMSE distribution for rigid Cp prediction with different ANN configurations constructed for the Cp results of the rigid wing (90 data case)

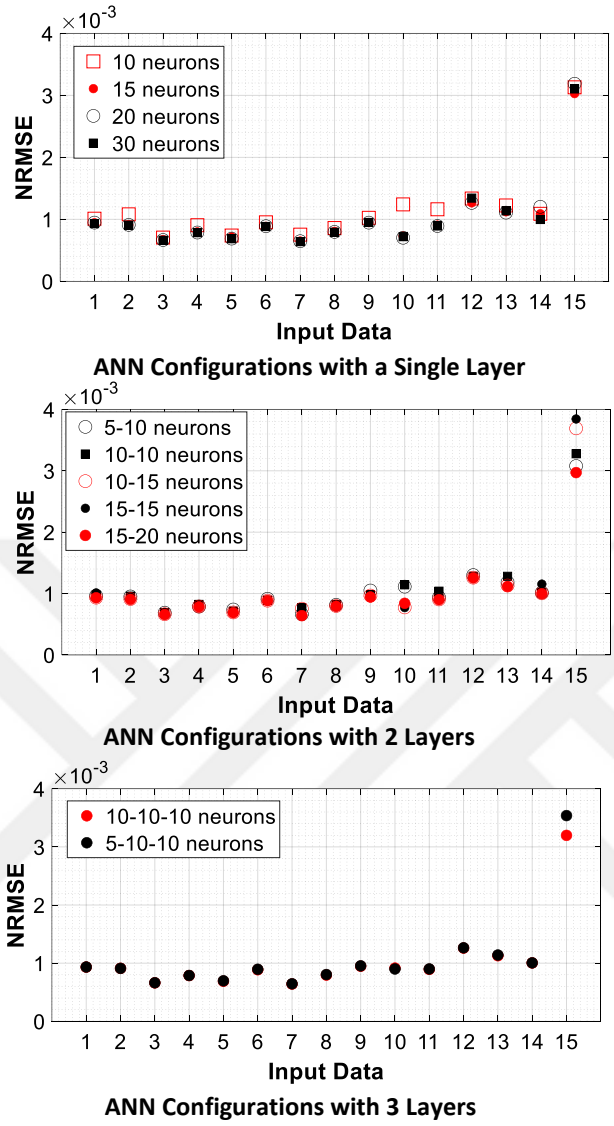

Figure I.5. NRMSE distribution for aeroelastic Cp prediction with different ANN configurations constructed for the Cp results of the aeroelastic wing (90 data case)

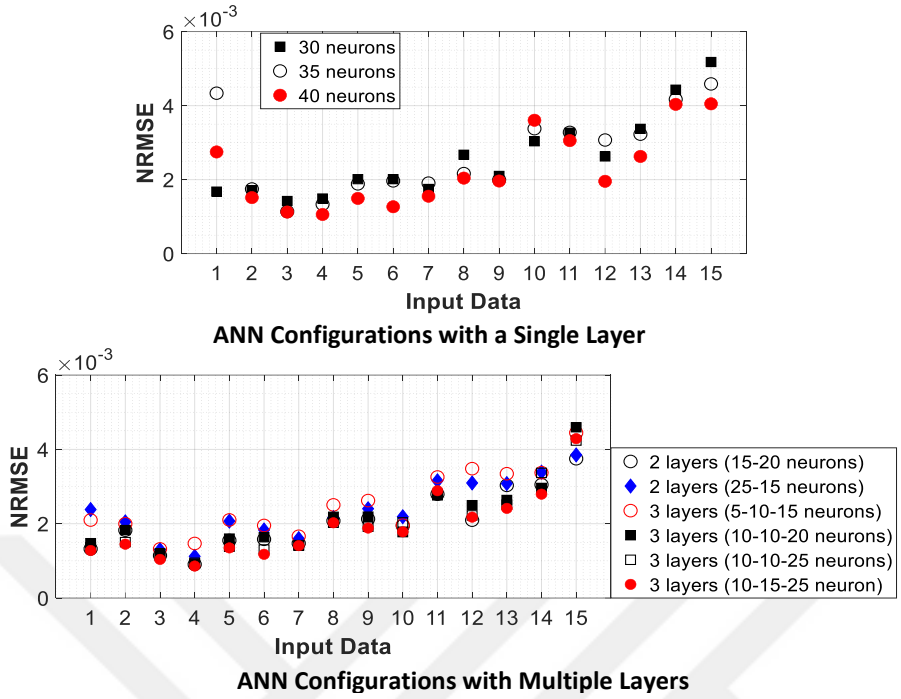

Figure I.6. NRMSE distribution for aeroelastic Cp prediction with different ANN configurations constructed for the Cp results of the rigid wing (126 data case)

J. Prediction Performance of POD based ROMs and Bilinear Interpolation for Different Data Sizes

The NRMSE results for the POD-based ROM predictions are compared with those obtained from bilinear interpolation results for the last parameter pair in each dataset in Figure J.1.

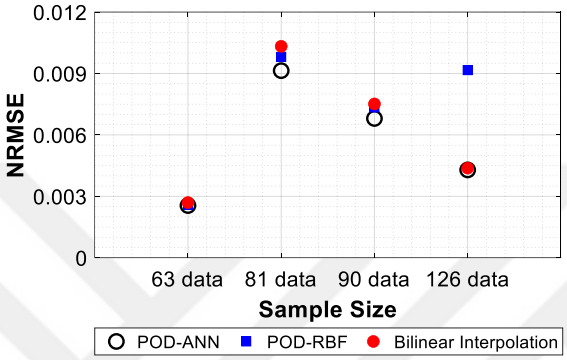

Figure J.1. NRMSE distribution of the predicted Cp results of rigid wing using different data samples and different methods

For all cases investigated, the POD-ANN method consistently yields the highest prediction accuracy. With the exception of the 126-sample dataset, bilinear interpolation produces the least accurate results. However, the differences among the methods are relatively small. Therefore, in scenarios where data reduction or real-time computational efficiency is not a critical concern, a basic method of bilinear interpolation can provide reasonably satisfactory results. This suggests that for certain applications, the simplicity and ease of implementation of bilinear interpolation may justify its use.

K. Prediction of the Results for Data Points Outside the Snapshot Matrix of 63 Parameter Pairs

In addition to the intermediate parameter pairs, the prediction capability of the POD based ROMs is also evaluated for parameter pairs outside the snapshot matrix of 63 parameter pairs given in Figure 3.1. For this reason, the following flow conditions are randomly chosen: M = 0.92 & AOA = 2.2°, M = 0.87 & AOA = 3.6°, M = 0.4 & AOA = 4.6°, and M = 0.5 & AOA = 5.6°. These conditions are marked with red markers and numbered accordingly in Figure K.1.

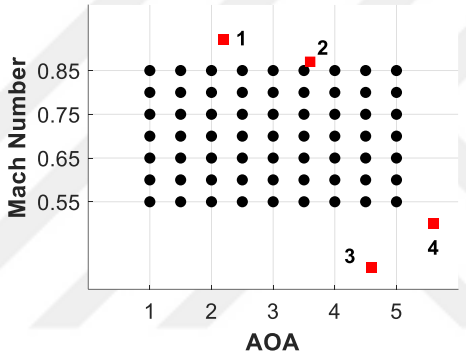

Figure K.1. Dataset with prediction points outside the domain

The corresponding NRMSE distribution of the Cp results for each prediction point is given in Figure K.2.

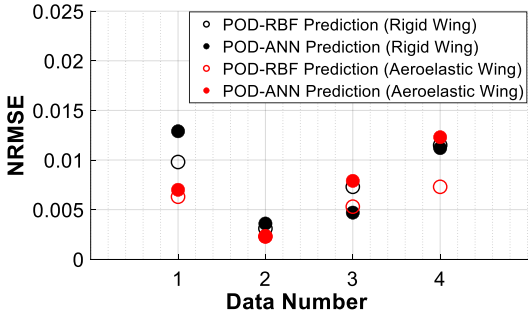

Figure K.2. NRMSE distribution of predicted Cp results of rigid and aeroelastic wings

The predicted results for the outlier points are also compared with those of the intermediate points (depicted in Figure 5.34) labelled as points 12, 13, 14 and 15, respectively in Figure K.3.

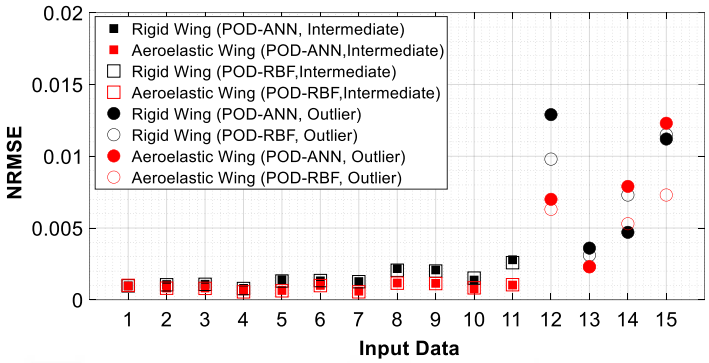

Figure K.3. NRMSE distribution of predicted Cp results of intermediate and outlier points for rigid and aeroelastic wings

It is seen that, with the exception of the second case (13th in Figure K.3), the accuracy of the results is much lower than the predicted Cp values for the intermediate points in the dataset. This is expected, as the flow characteristics tend to change remarkably as we get further away from the known data points. Therefore, the second case, being closer to the data points, shows the highest accuracy. Additionally, it is observed that the accuracy of the POD-RBF predictions is higher than that of the POD-ANN predictions across nearly all flow conditions. Figure K.4 shows the sectional Cp distributions for four prediction points using POD-RBF, highlighting noticeable mismatches with high-fidelity results (except for the second case) indicating the method's unreliability outside the defined range.

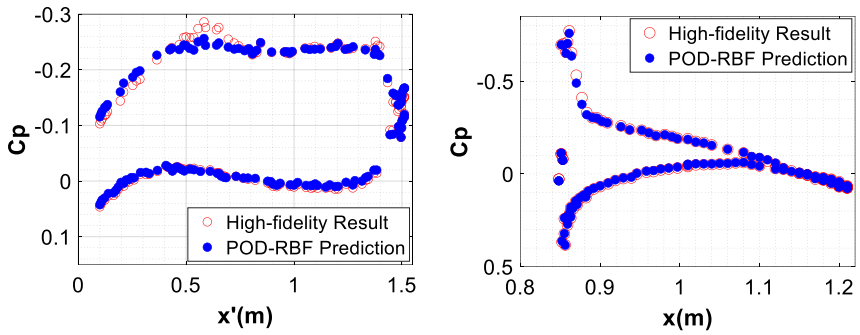

Spanwise and chordwise Cp distribution of the rigid wing for M=0.92 & AOA=2.2°

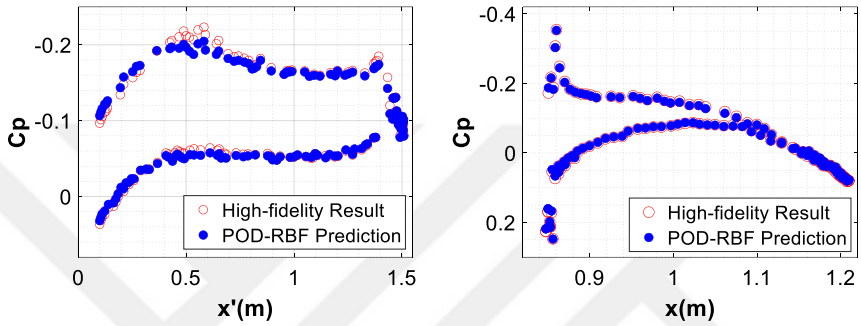

Spanwise and chordwise Cp distribution of the aeroelastic wing for M=0.92 & AOA=2.2°

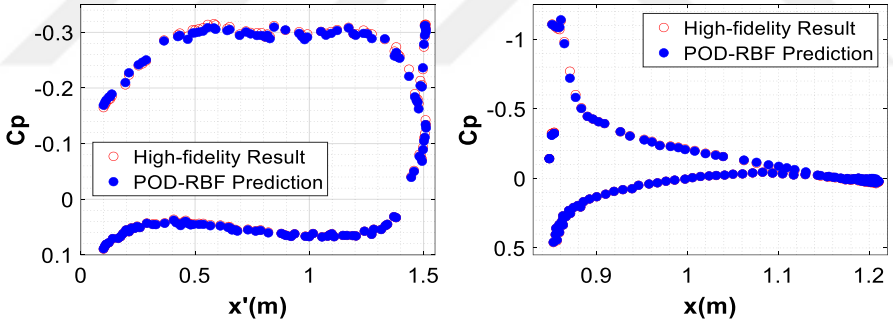

Spanwise and chordwise Cp distribution of the rigid wing for M=0.87 & AOA=3.6°

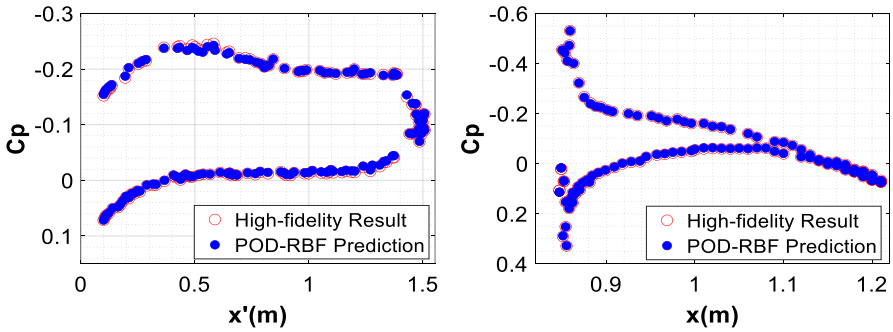

Spanwise and chordwise Cp distribution of the aeroelastic wing for M=0.87 & AOA=3.6°

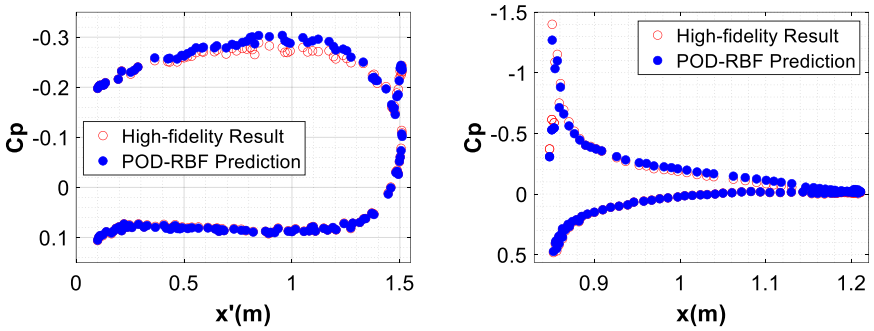

Spanwise and chordwise Cp distribution of the rigid wing for M=0.4 & AOA= 4.6°

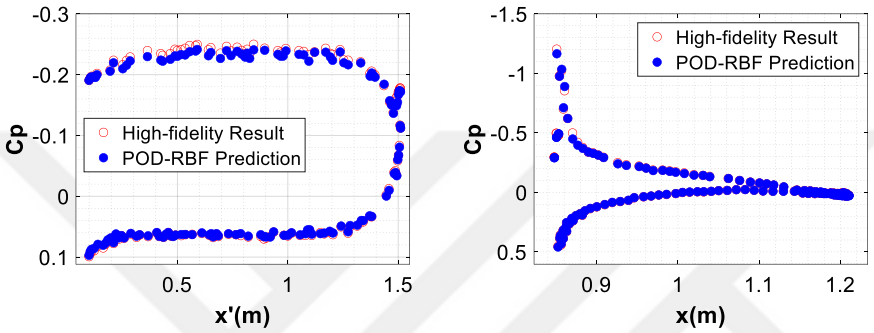

Spanwise and chordwise Cp distribution of the aeroelastic wing for M=0.4 & AOA= 4.6°

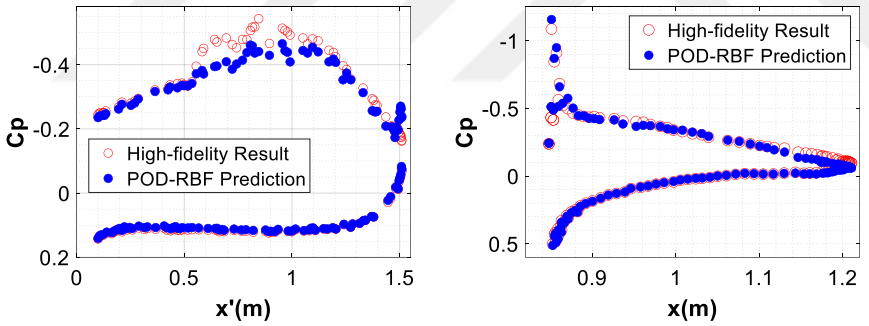

Spanwise and chordwise Cp distribution of the rigid wing for M=0.5 & AOA=5.6°

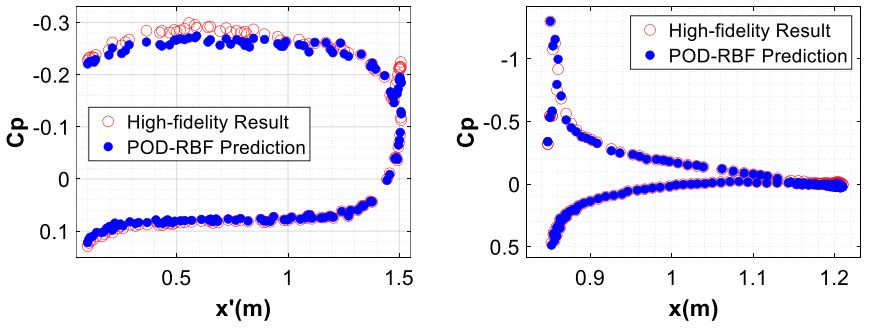

Spanwise and chordwise Cp distribution of the aeroelastic wing for M=0.5 & AOA=5.6°

Figure K.4. Predicted sectional Cp results obtained by using the POD-RBF method

CURRICULUM VITAE

Surname, Name: Yılmaz (Özkaya), Zarif Özge

EDUCATION

Degree	Institution	Year of Graduation
MS	METU Aerospace Engineering	2017
BS (ranked 1st in the department)	METU Aerospace Engineering	2014
High School	Gazi Anatolian High School, Ankara	2009

WORK EXPERIENCE

Enrollment	Place	Year
Lead Engineer	Roketsan	2021-Present
Senior Engineer	Roketsan	2019-2021
Engineer	Roketsan	2014-2019
Candidate Engineer	Roketsan	2013-2014
Intern Eng. Student	TAI	2012-2013

FOREIGN LANGUAGES

English

PUBLICATIONS

1. Özkaya Yılmaz, Ö., Kayran, A., "A Comparative Study on the Efficiencies of Aerodynamic Reduced Order Models of Rigid and Aeroelastic Sweptback Wings", Aerospace 2024, 11(8), 616; https://doi.org/10.3390/aerospace11080616, (2024).

CONFERENCE PAPERS

1. Yılmaz, Ö., Kayran, A, "Performance Comparison of RBF and ANN Based Surrogate Models for the Static Aeroelastic Behavior of a Wing", AIAA Aviation and ASCEND, 2024, Las Vegas, Nevada, USA; https://doi.org/10.2514/6.2024-4232, (2024).

2. Yılmaz, Ö., Kayran, A, "Application of Artificial Neural Network based Surrogate Models for Parameterized Flow to a Sweptback Wing: An Outlook for Wind Turbine Blades" AIAA Scitech, 2025, Orlando, Florida, USA, (2025).

3. Özkaya, Ö., Kayran, A., "Nonlinear Static Aeroelastic Behavior of Composite Missile Fin with Interlaminar and Intralaminar Damage", 10.2514/6.2018-1449, AIAA Science and Technology Forum and Exposition, AIAA SciTech 2018, Kissimmee, Florida, USA, (2018).

4. Özkaya, Ö., Kayran, A., "Nonlinear Static Aeroelastic Behavior of Composite Missile Fin with Interlaminar Damage", AIAC-2017-051, 9th Ankara International Aerospace Conference-AIAC, METU, Ankara, Turkey, (2017).